

AD-A266 368

RADIX SYSTEMS

TR-93-081

TR-93-081

2

ANALYSIS OF CHAOTIC WAVEFORMS FOR
APPLICATION TO ACTIVE SONAR SYSTEMS

FINAL REPORT

Nanda K. Alapati

Richard H. Kirklin

Paul C. Etter

DTIC
ELECTE
JUN 29 1993
S A D

Radix Systems, Inc.
201 Perry Parkway
Gaithersburg, MD 20877

June 1993

This document has been approved
for public release and sale; its
distribution is unlimited.

Sponsored by:

Advanced Research Projects Agency
Maritime Systems Technology Office
ARPA Order No. 7911
Contract MDA-972-91-C-0059

"The views and conclusions contained in this document are those of the authors and should not be interpreted as representing the official policies, either expressed or implied, of the Advanced Research Projects Agency or any other part of the U.S. Government."

93-14861



93 6 00 001

REPORT DOCUMENTATION PAGE

Form Approved
GMB No. 0704-0188

Public reporting burden for this collection of information is estimated to average 1 hour per response, including the time for reviewing instructions, searching existing data sources, gathering and maintaining the data needed, and completing and reviewing the collection of information. Send comments regarding this burden estimate or any other aspect of this collection of information, including suggestions for reducing the burden, to Washington Headquarters Service, Directorate for Information Operations and Reports, 1215 Jefferson Davis Highway, Suite 1204, Arlington, VA 22202-4302, and to the Office of Management and Budget, Paperwork Reduction Project (0704-0188), Washington, DC 20503.

1. AGENCY USE ONLY (Leave blank)		2. REPORT DATE June 1993	3. REPORT TYPE AND DATES COVERED Contractor Report (Final)	
4. TITLE AND SUBTITLE Analysis of Chaotic Waveforms for Application to Active Sonar Systems			5. FUNDING NUMBERS C: MDA-972-92-C-0059 ARPA Order No. 7911	
6. AUTHOR(S) Nanda K. Alapati; Richard H. Kirklin; Paul C. Etter				
7. PERFORMING ORGANIZATION NAME(S) AND ADDRESS(ES) Radix Systems, Inc. 201 Perry Parkway Gaithersburg, MD 20877			8. PERFORMING ORGANIZATION REPORT NUMBER TR-93-081	
9. SPONSORING/MONITORING AGENCY NAME(S) AND ADDRESS(ES) Advanced Research Projects Agency Maritime Systems Technology Office			10. SPONSORING/MONITORING AGENCY REPORT NUMBER	
11. SUPPLEMENTARY NOTES Nanda K. Alapati: (301)926-3200 Dr. William Carey				
12a. DISTRIBUTION/AVAILABILITY STATEMENT National Technical Information Service 5285 Port Royal Road Springfield, VA 22161			12b. DISTRIBUTION CODE	
13. ABSTRACT (Maximum 200 words) This report evaluates the feasibility of using a new class of chaotic waveforms in low-frequency active acoustic scenarios. These waveforms are generated by nonlinear processes and therefore have characteristics that differ from their linear counterparts. There are two principal findings of this evaluation. First, as broadband signals, chaotic waveforms have desirable characteristics such as range resolution, range-rate resolution (Doppler), and reverberation discrimination against moving targets. Second, unlike pseudo-random noise, chaotic waveforms are amenable to noise reduction techniques that enhance the Signal-to-Noise Ratio (SNR) because they are of low dimensionality. Additionally, because chaotic signals are difficult to recognize, they decrease the potential for recognition by opposition forces. Using a selection of qualitative and quantitative metrics, the Lorenz waveform is identified as suitable for use in active surveillance scenarios. Further, it is demonstrated that, given present acoustic projector technology constraints, waveform generation can be accomplished using straightforward band-shifting techniques.				
14. SUBJECT TERMS Chaos Nonlinear processes Signal processing			15. NUMBER OF PAGES 116	
			16. PRICE CODE	
17. SECURITY CLASSIFICATION OF REPORT Unclassified	18. SECURITY CLASSIFICATION OF THIS PAGE Unclassified	19. SECURITY CLASSIFICATION OF ABSTRACT Unclassified	20. LIMITATION OF ABSTRACT Unlimited	

TR-93-081

**ANALYSIS OF CHAOTIC WAVEFORMS FOR
APPLICATION TO ACTIVE SONAR SYSTEMS****FINAL REPORT**

Nanda K. Alapati

Richard H. Kirklin

Paul C. Etter

Radix Systems, Inc.
201 Perry Parkway
Gaithersburg, MD 20877

June 1993

Sponsored by:

Advanced Research Projects Agency
Maritime Systems Technology Office
ARPA Order No. 7911
Contract MDA-972-91-C-0059

"The views and conclusions contained in this document are those of the authors and should not be interpreted as representing the official policies, either expressed or implied, of the Advanced Research Projects Agency or any other part of the U.S. Government."

Accession For	
NTIS - CRA&I	<input checked="" type="checkbox"/>
DTIC - TAB	<input type="checkbox"/>
Unannounced	<input type="checkbox"/>
Justification	
By	
Distribution/	
Availability Codes	
Dist	Avail and/or Special
A-1	

DTIC QUALITY INSPECTED 2

ABSTRACT

This report evaluates the feasibility of using a new class of chaotic waveforms in low-frequency active acoustic scenarios. These waveforms are generated by nonlinear processes and therefore have characteristics that differ from their linear counterparts. There are two principal findings of this evaluation. First, as broadband signals, chaotic waveforms have desirable characteristics such as range resolution, range-rate resolution (Doppler), and reverberation discrimination against moving targets. Second, unlike pseudo-random noise, chaotic waveforms are amenable to noise reduction techniques that enhance the Signal-to-Noise Ratio (SNR) because they are of low dimensionality. Additionally, because chaotic signals are difficult to recognize, they decrease the potential for recognition by opposition forces.

Using a selection of qualitative and quantitative metrics, the Lorenz waveform is identified as suitable for use in active surveillance scenarios. Further, it is demonstrated that, given present acoustic projector technology constraints, waveform generation can be accomplished using straightforward band-shifting techniques.

TABLE OF CONTENTS

ABSTRACT	ii
LIST OF FIGURES	v
LIST OF TABLES	x
ACKNOWLEDGMENTS	xi
1. INTRODUCTION	1
2. CHAOTIC WAVEFORMS, PROPERTIES and METRICS	3
2.1 Chaotic Waveforms	3
2.2 Properties of Chaotic Waveforms	3
2.3 Conventional Metric	9
2.4 Qualitative Chaotic Metrics	9
2.4.1 Phase Plots	9
2.4.2 Close Return Map	10
2.4.3 Other Qualitative Metrics	10
2.5 Quantitative Techniques	11
2.5.1 Correlation Dimension	11
2.5.2 Local Intrinsic Dimension	12
2.5.3 Other Quantitative Metrics	13
3. SOURCES AND EFFECTS OF SIGNAL DISTORTION	14
3.1 Sources of Signal Distortion	14
3.1.1 Propagation through Ocean Channel	14
3.1.1.1 Characteristics of Ocean Channel	15
3.1.1.2 Ocean Impulse Response	15
3.1.2 Doppler	17
3.1.3 Noise Contamination	19
3.2 Effects of Signal Distortion	19
3.2.1 Replica Correlation	20
3.2.1.1 Noise Contamination	20
3.2.1.2 Propagation and Doppler	20
3.2.2 Qualitative Assessments	28
3.2.2.1 Phase Plots	28
3.2.2.2 Close Return Map	30
3.2.3 Quantitative Assessments	33
3.2.3.1 Correlation Dimension	33
3.2.3.2 Local Intrinsic Dimension	39

TABLE OF CONTENTS (continued)

4.	NOISE REDUCTION	41
5.	CONCLUSIONS	46
	REFERENCES	47
	APPENDIX A NONLINEAR EQUATIONS	A-1
	A.1 Quasiperiodically forced van der Pol equation:	A-1
	A.2 Rössler equation:	A-1
	A.3 Nonlinear stochastic equation:	A-2
	A.4 Fokker Equation	A-2
	APPENDIX B PROPAGATION CHANNEL	B-1
	APPENDIX C REPLICA CORRELATIONS WITH NOISY SIGNALS	C-1
	APPENDIX D REPLICA CORRELATIONS WITH DOPPLER-SHIFTED ECHOES	D-1
	APPENDIX E PHASE PLOTS OF DISTORTED SIGNALS	E-1
	APPENDIX F STEREOSCOPIC PROJECTIONS	F-1
	APPENDIX G CORRELATION DIMENSION	G-1

LIST OF FIGURES

- Figure 2.1-1. Lorenz Waveform: (a) equation; (b) time series; (c) phase plot; and (d) power spectrum.
- Figure 2.1-2. Duffing Waveform: (a) equation; (b) time series; (c) phase plot; and (d) power spectrum.
- Figure 2.1-3. Henon Waveform: (a) equation; (b) time series; (c) phase plot; and (d) power spectrum.
- Figure 2.1-4. Iterative Waveform: (a) equation; (b) time series; (c) phase plot; and (d) power spectrum.
- Figure 2.1-5. Ambiguity Functions for Chaotic Waveforms: (a) Lorenz; (b) Duffing; (c) Henon; and (d) Iterative.
- Figure 3.1-1. Sound Speed Profiles Used in Generating Ocean Impulse Responses: (a) Profile 1; and (b) Profile 2.
- Figure 3.1-2. Case 1 Ocean Impulse Responses for (a) Outgoing Channel and (b) Incoming Channel; and Frequency Responses for (c) Outgoing Channel and (d) Incoming Channel.
- Figure 3.2-1. Replica Correlations for Noise-Contaminated Lorenz Echoes for Selected SNR Values: (a) 20 dB; (b) 10 dB; (c) 0 dB; and (d) -10 dB.
- Figure 3.2-2. Replica Correlations for Noise-Contaminated Lorenz Echoes for Selected SNR Values: (a) -15 dB; (b) -20 dB; (c) -25 dB; and (d) -30 dB.
- Figure 3.2-3. Replica Correlations for Doppler-Shifted Lorenz Echoes in Case 1 with an Actual Doppler of 20 Knots and Assumed Dopplers of: (a) 19.5 Knots; (b) 20 Knots; (c) 20.2 Knots; and (d) 20.4 Knots.
- Figure 3.2-4. Replica Correlations Illustrating the Effect of Doppler: (a) No Doppler Shift to Either Replica or Echo; (b) 20 Knot Doppler Shift of Both Replica and Echo.
- Figure 3.2-5. Replica Correlations for Doppler-Shifted Lorenz Echoes with an Actual Doppler of 20 Knots and Assumed Dopplers of : (a) 15 Knots; (b) 20 Knots; (c) 22 Knots; and (d) 24 Knots. Transmitted Signal is Bandshifted 50 Hz, and There is no Transmission Distortion.

- Figure 3.2-6. Replica Correlation with 'De-Dopplerized' and Demodulated Lorenz Echo.
- Figure 3.2-7. Phase Plot of the Lorenz Waveform: (a) original; (b) modulated, then demodulated; (c) at target; (d) of echo; (e) Doppler-shifted; (f) modulated then Doppler-shifted; (g) at target, Doppler-shifted; (h) Doppler-shifted echo.
- Figure 3.2-8. Close Return Maps of Lorenz Waveform with Various Levels of Added Noise, and Gaussian Noise Alone.
- Figure 3.2-9. Close Return Maps of Distorted Lorenz Waveform.
- Figure 3.2-10. Close Return Maps of Distorted Duffing Waveform.
- Figure 3.2-11. Close Return Maps of Distorted Henon Waveform.
- Figure 4-1. Noise Reduction Time Series: (a) Time Series of Lorenz Waveform; (b) Gaussian Noise; (c) Signal Plus Noise; and (d) Noise-Reduced Signal.
- Figure 4-2. Noise Reduction Power Spectra: (a) Power Spectrum of Lorenz Waveform; (b) Gaussian Noise; (c) Signal Plus Noise; and (d) Noise-Reduced Signal.
- Figure 4-3. Close Return Maps of the Lorenz Waveform: (a) SNR Infinite; (b) in Gaussian Noise at 0 dB SNR; (c) After Noise Reduction.
- Figure B-1. Ocean Impulse and Frequency Responses for Outgoing and Incoming Channels for Case 1.
- Figure B-2. Ocean Impulse and Frequency Responses for Outgoing and Incoming Channels for Case 2.
- Figure B-3. Ocean Impulse and Frequency Responses for Outgoing and Incoming Channels for Case 3.
- Figure B-4. Ocean Impulse and Frequency Responses for Outgoing and Incoming Channels for Case 4.
- Figure B-5. Ocean Impulse and Frequency Responses for Outgoing and Incoming Channels for Case 5.
- Figure B-6. Ocean Impulse and Frequency Responses for Outgoing and Incoming Channels for Case 6.

- Figure C-1. Replica Correlations for Noise-Contaminated Lorenz Echoes for Selected SNR Values: (a) 20 dB; (b) 10 dB; (c) 0 dB; and (d) -10 dB.
- Figure C-2. Replica Correlations for Noise-Contaminated Lorenz Echoes for Selected SNR Values: (a) -15 dB; (b) -20 dB; (c) -25 dB; and (d) -30 dB..
- Figure C-3. Replica Correlations for Noise-Contaminated Duffing Echoes for Selected SNR Values: (a) 20 dB; (b) 10 dB; (c) 0 dB; and (d) -10 dB.
- Figure C-4. Replica Correlations for Noise-Contaminated Duffing Echoes for Selected SNR Values: (a) -15 dB; (b) -20 dB; (c) -25 dB; and (d) -30 dB.
- Figure C-5. Replica Correlations for Noise-Contaminated Henon Echoes for Selected SNR Values: (a) 20 dB; (b) 10 dB; (c) 0 dB; and (d) -10 dB.
- Figure C-6. Replica Correlations for Noise-Contaminated Henon Echoes for Selected SNR Values: (a) -15 dB; (b) -20 dB; (c) -25 dB; and (d) -30 dB.
- Figure C-7. Replica Correlations for Noise-Contaminated Iterative Echoes for Selected SNR Values: (a) 20 dB; (b) 10 dB; (c) 0 dB; and (d) -10 dB.
- Figure C-8. Replica Correlations for Noise-Contaminated Iterative Echoes for Selected SNR Values: (a) -15 dB; (b) -20 dB; (c) -25 dB; and (d) -30 dB.
- Figure D-1. Replica Correlations for Doppler-Shifted Lorenz Echoes in Case 1 with an Actual Doppler of 20 Knots and Assumed Dopplers of: (a) 19.5 Knots; (b) 20 Knots; (c) 20.2 Knots; and (d) 20.4 Knots.
- Figure D-2. Replica Correlations for Doppler-Shifted Lorenz Echoes in Case 2 with an Actual Doppler of 20 Knots and Assumed Dopplers of: (a) 19.5 Knots; (b) 20 Knots; (c) 20.2 Knots; and (d) 20.4 Knots.
- Figure D-3. Replica Correlations for Doppler-Shifted Lorenz Echoes in Case 3 with an Actual Doppler of 20 Knots and Assumed Dopplers of: (a) 19.5 Knots; (b) 20 Knots; (c) 20.2 Knots; and (d) 20.4 Knots.
- Figure D-4. Replica Correlations for Doppler-Shifted Lorenz Echoes in Case 4 with an Actual Doppler of 20 Knots and Assumed Dopplers of: (a) 19.5 Knots; (b) 20 Knots; (c) 20.2 Knots; and (d) 20.4 Knots.
- Figure D-5. Replica Correlations for Doppler-Shifted Lorenz Echoes in Case 5 with an Actual Doppler of 20 Knots and Assumed Dopplers of: (a) 19.5 Knots; (b) 20 Knots; (c) 20.2 Knots; and (d) 20.4 Knots.

- Figure D-6. Replica Correlations for Doppler-Shifted Lorenz Echoes in Case 6 with an Actual Doppler of 20 Knots and Assumed Dopplers of: (a) 19.5 Knots; (b) 20 Knots; (c) 20.2 Knots; and (d) 20.4 Knots.
- Figure E-1. Phase Plot of the Lorenz Waveform: (a) original; (b) modulated, then demodulated; (c) at target; (d) of echo; (e) Doppler-shifted; (f) modulated then Doppler-shifted; (g) at target, Doppler-shifted; (h) Doppler-shifted echo.
- Figure E-2. Phase Plot of the Duffing Waveform: (a) original; (b) modulated, then demodulated; (c) at target; (d) of echo; (e) Doppler-shifted; (f) modulated then Doppler-shifted; (g) at target, Doppler-shifted; (h) Doppler-shifted echo.
- Figure E-3. Phase Plot of the Henon Waveform: (a) original; (b) modulated, then demodulated; (c) at target; (d) of echo; (e) Doppler-shifted; (f) modulated then Doppler-shifted; (g) at target, Doppler-shifted; (h) Doppler-shifted echo.
- Figure E-4. Phase Plot of the Iterative Waveform: (a) original; (b) modulated, then demodulated; (c) at target; (d) of echo; (e) Doppler-shifted; (f) modulated then Doppler-shifted; (g) at target, Doppler-shifted; (h) Doppler-shifted echo.
- Figure F-1. Stereoscopic Pairs of the Lorenz (a,b) and Duffing (c,d) Waveform Phase Plots Embedded in Three Dimensions.
- Figure F-2. Stereoscopic Pairs of the Henon (a,b) and Iterative (c,d) Waveform Phase Plots Embedded in Three Dimensions.
- Figure G-1. Correlation Dimension Extraction Curve for Sine Wave Embedded in 5 Dimensions.
- Figure G-2. Correlation Dimension Extraction Curve for Chirp Embedded in 5 Dimensions.
- Figure G-3. Correlation Dimension Extraction Curve for Gaussian Noise Embedded in 5 Dimensions.
- Figure G-4. Correlation Dimension Extraction Curve for Gaussian Noise Embedded in 7 Dimensions.

- Figure G-5. Correlation Dimension Extraction Curve for Gaussian Noise Embedded in 10 Dimensions.
- Figure G-6. Correlation Dimension Extraction Curve for Lorenz Waveform Embedded in 4 Dimensions.
- Figure G-7. Correlation Dimension Extraction Curve for Lorenz Waveform Propagated Through Case 1 Ocean with 20 Knots Doppler, Embedded in 5 Dimensions.
- Figure G-8. Correlation Dimension Extraction Curve for Lorenz Waveform Propagated Through Case 1 Ocean with 20 Knots Doppler, Embedded in 10 Dimensions.
- Figure G-9. Correlation Dimension Extraction Curve for Lorenz Waveform with 20 Knots Doppler, Embedded in 10 Dimensions.
- Figure G-10. Correlation Dimension Extraction Curve for Duffing Waveform Embedded in 4 Dimensions.
- Figure G-11. Correlation Dimension Extraction Curve for Duffing Waveform Embedded in 10 Dimensions.
- Figure G-12. Correlation Dimension Extraction Curve for Duffing Waveform Propagated Through Case 1 Ocean with 20 Knots Doppler, Embedded in 5 Dimensions.
- Figure G-13. Correlation Dimension Extraction Curve for Duffing Waveform Propagated Through Case 1 Ocean with 20 Knots Doppler, Embedded in 10 Dimensions.
- Figure G-14. Correlation Dimension Extraction Curve for Duffing Waveform with 20 Knots Doppler, Embedded in 10 Dimensions.
- Figure G-15. Correlation Dimension Extraction Curve for Henon Waveform Embedded in 5 Dimensions.
- Figure G-16. Correlation Dimension Extraction Curve for Henon Waveform Propagated Through Case 1 Ocean with 20 Knots Doppler, Embedded in 5 Dimensions.

- Figure G-17. Correlation Dimension Extraction Curve for Henon Waveform Propagated Through Case 1 Ocean with 20 Knots Doppler, Embedded in 7 Dimensions.
- Figure G-18. Correlation Dimension Extraction Curve for Henon Waveform Propagated Through Case 1 Ocean with 20 Knots Doppler, Embedded in 10 Dimensions.
- Figure G-19. Correlation Dimension Extraction Curve for Henon Waveform with 20 Knots Doppler, Embedded in 10 Dimensions.
- Figure G-20. Correlation Dimension Extraction Curve for Iterative Waveform Embedded in 5 Dimensions.
- Figure G-21. Correlation Dimension Extraction Curve for Iterative Waveform Propagated Through Case 1 Ocean with 20 Knots Doppler, Embedded in 5 Dimensions.
- Figure G-22. Correlation Dimension Extraction Curve for Iterative Waveform Propagated Through Case 1 Ocean with 20 Knots Doppler, Embedded in 10 Dimensions.
- Figure G-23. Correlation Dimension Extraction Curve for Iterative Waveform with 20 Knots Doppler, Embedded in 10 Dimensions.

LIST OF TABLES

- Table 3.1-1. Summary of Test Cases.
- Table 3.2-1. Correlation Dimension
- Table 3.2-2. Local Intrinsic Dimension (LID)

ACKNOWLEDGMENTS

It is a pleasure to acknowledge the professional direction provided by Dr. William Carey and Capt. Ed Mihalak of the Defense Advanced Research Projects Agency (DARPA).

Dr. Duncan Sheldon, Harvey Hamel and Bill Corneau of the Naval Undersea Warfare Center, New London Detachment, kindly provided the ocean frequency response information used in this report.

1. INTRODUCTION

Requirements for advanced acoustic sensors will be driven largely by the proliferation of weapons systems to those third-world countries having maritime interests. Particularly important will be the need to monitor the conventional submarine activities of such countries. When operating on battery power, these submarines are extremely difficult to detect and classify, especially in noisy coastal regions where the sea floor is often littered with debris and the water column is densely populated by biologics.

The utility of traditional passive acoustic sensors has been diminished since such sensors have relied upon the noise radiated by the submarine's own propulsion system, or other mechanical sources mostly of a transient nature. Active sonars, by nature, are susceptible to counterdetection and thus neutralization by countermeasures. This situation has necessitated the exploration of alternative technologies and tactics that afford greater detection potential and reduced vulnerability to countermeasures in near-land warfare.

One viable concept is that of low-frequency, bistatic systems that use a powerful, but remote, acoustic projector to ensonify a large volume of ocean. Target echoes are then detected by separate, passive acoustic receivers. This type of bistatic surveillance system has its own set of troublesome problems. Principal among these are the unwanted reverberant returns from bathymetric features, masking of target echoes by the source pulse, poor understanding of the bistatic scattering properties of the sea surface and sea floor, difficulties in target localization, multipath resolution, and noise field estimation.

The purpose of this study is to evaluate the feasibility of using a new class of chaotic waveforms in low-frequency active acoustic scenarios in realistic ocean environments. These waveforms are generated by nonlinear processes and therefore have characteristics in common with broadband signals: range resolution, range-rate resolution (Doppler), and reverberation discrimination against moving targets.

This report is organized into five sections. After the introduction in Section 1, chaotic waveforms, properties and metrics are discussed in Section 2. Section 3 examines the effects of signal distortion on the integrity of chaotic waveforms, and noise reduction techniques are discussed in Section 4. Section 5 presents the conclusions of the study.

2. CHAOTIC WAVEFORMS, PROPERTIES and METRICS

2.1 Chaotic Waveforms

Four basic chaotic waveforms have been selected for detailed examination: Lorenz, Duffing, Henon and Iterative. For each of these waveforms, the following information is presented: equation; time series; phase plot; and power spectrum (Figures 2.1-1 through 2.1-4). The phase plot is a qualitative metric for viewing chaotic behavior in signals; this metric will be described in more detail in Section 2.4.1. In addition, the ambiguity function is presented for all four waveforms (Figure 2.1-5). The ambiguity function describes the total ambiguity in resolving targets in range (time delay) and velocity (Doppler frequency). Other nonlinear waveforms that were investigated, but not discussed in the body of this report, are contained in Appendix A.

2.2 Properties of Chaotic Waveforms

Chaos is the appearance of apparently random motion in both forced and unforced deterministic dynamical systems. A chaotic system appears to exhibit irregular, unpredictable behavior. While both noise and chaotic signals are characterized by a broadband power spectrum, chaotic signals can be distinguished from noise on the basis of dimensionality. Specifically, noise has a high dimensionality while chaotic signals have a low, and often non-integer (or fractal), dimension. Both qualitative and quantitative techniques are available for the determination of the dimensionality of nonlinear waveforms. In addition, the conventional replica correlation technique can be used to detect nonlinear waveforms.

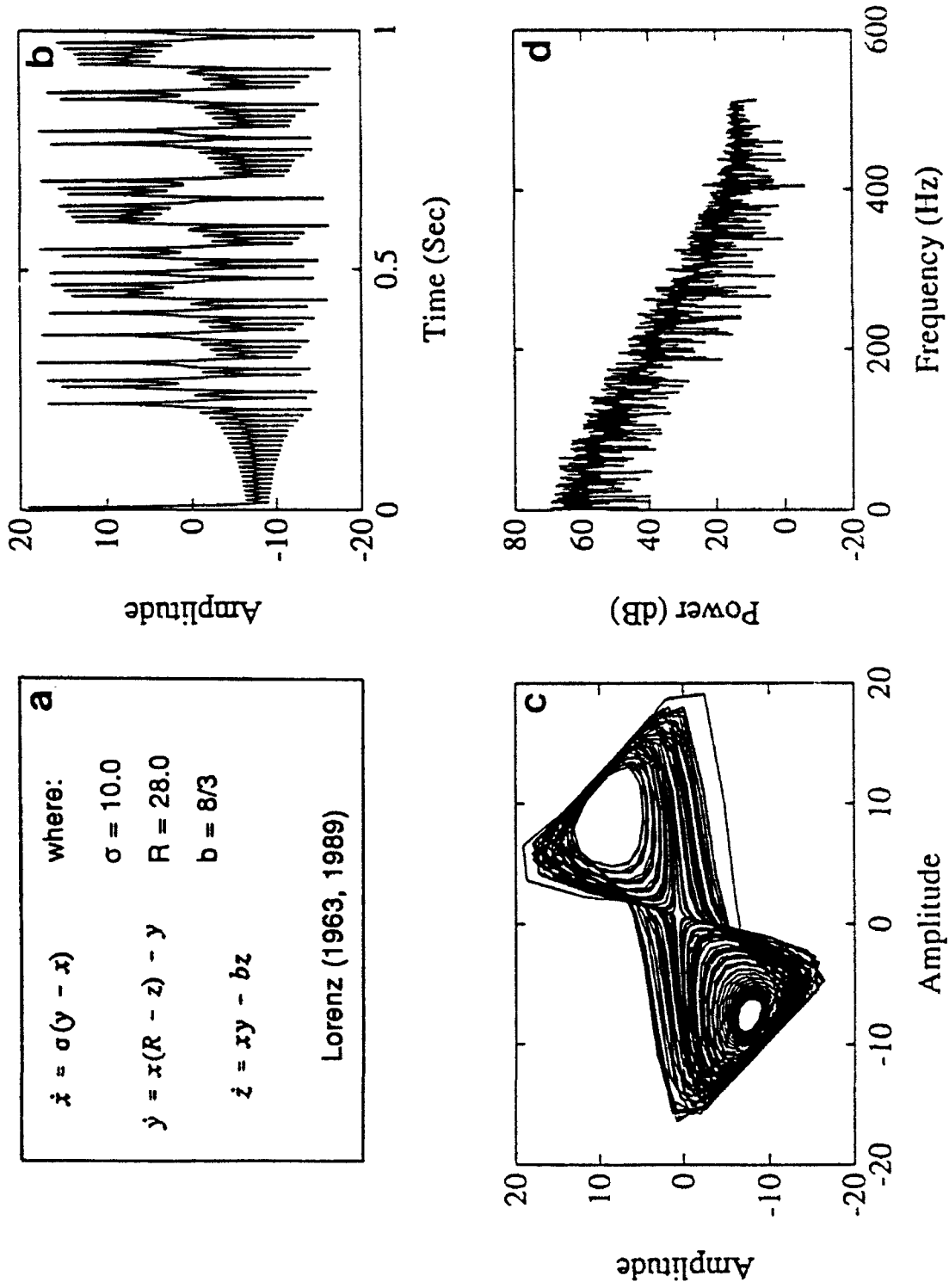


Figure 2.1-1. Lorenz Waveform: (a) equation; (b) time series; (c) phase plot; and (d) power spectrum.

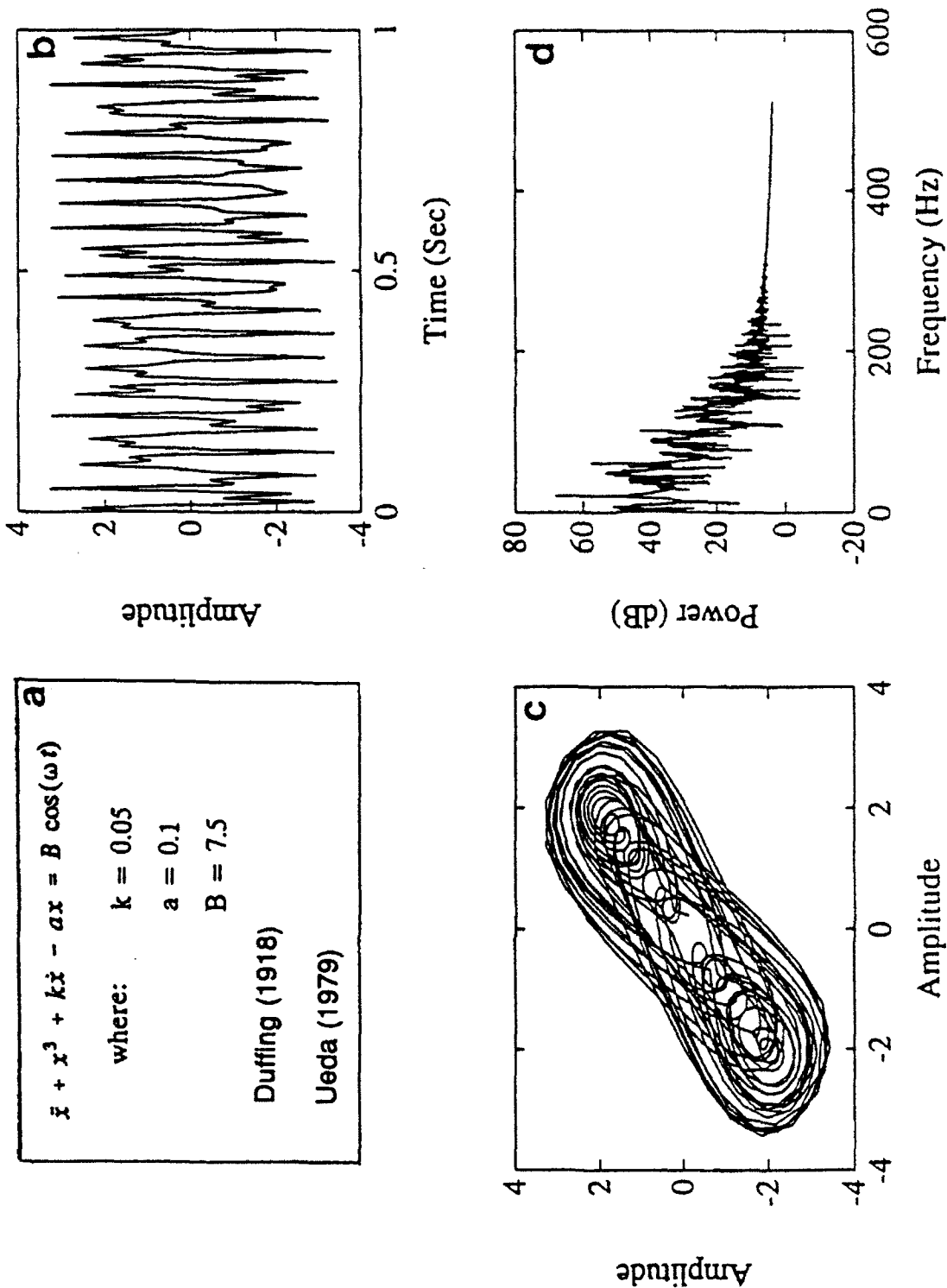


Figure 2.1-2. Duffing Waveform: (a) equation; (b) time series; (c) phase plot; and (d) power spectrum.

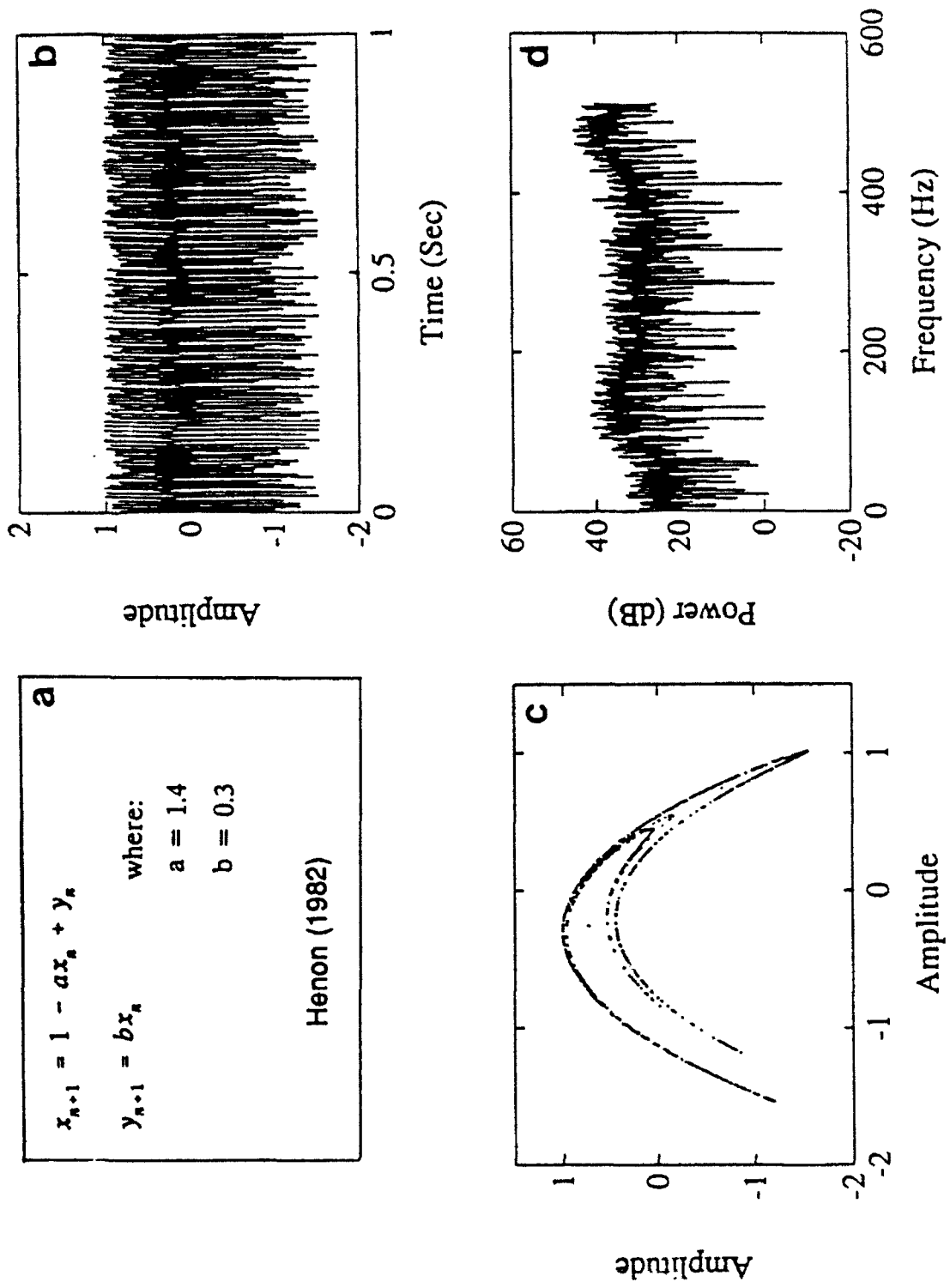


Figure 2.1-3. Henon Waveform: (a) equation; (b) time series; (c) phase plot; and (d) power spectrum.

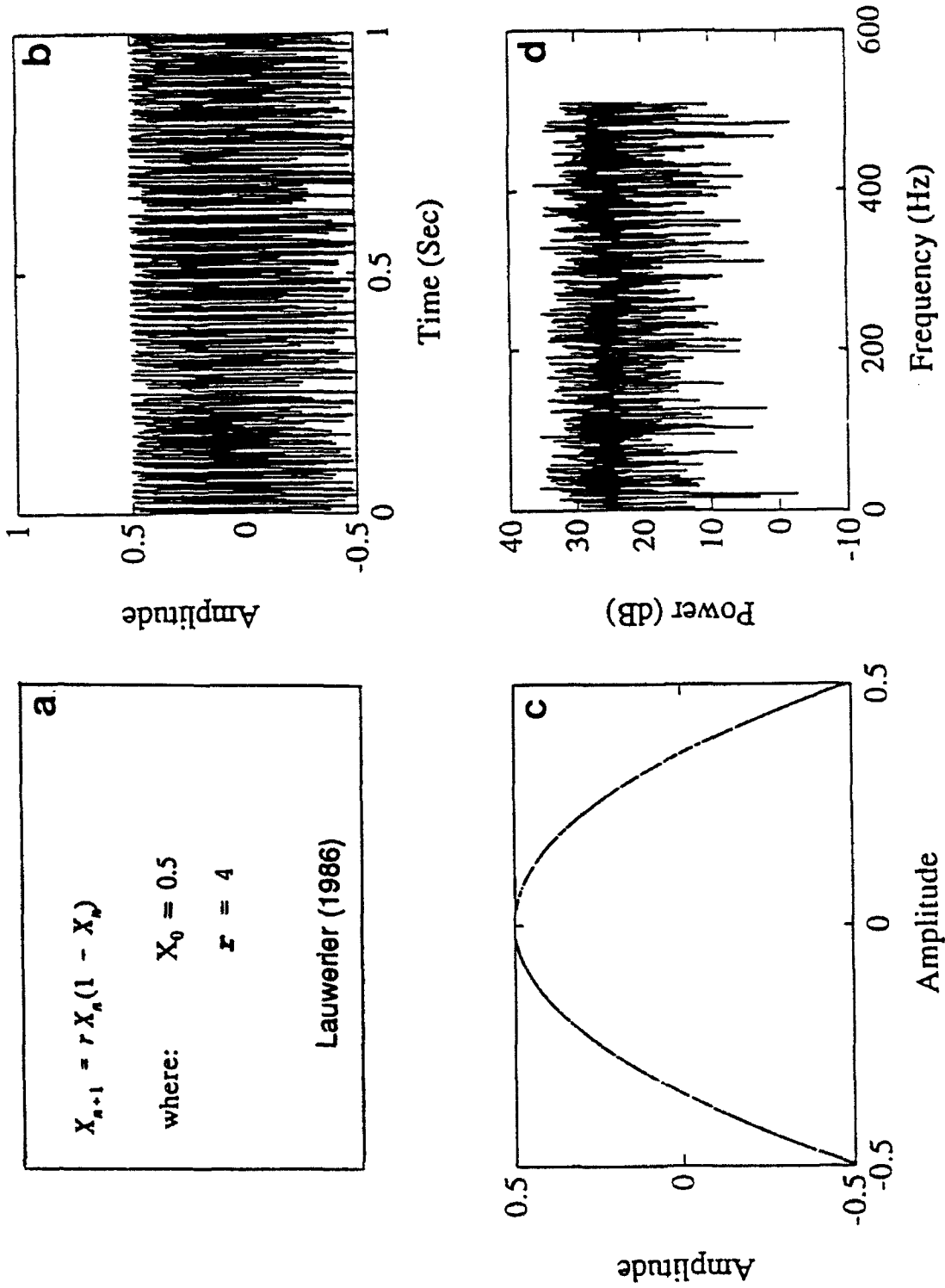


Figure 2.1-4. Iterative Waveform: (a) equation; (b) time series; (c) phase plot; and (d) power spectrum.

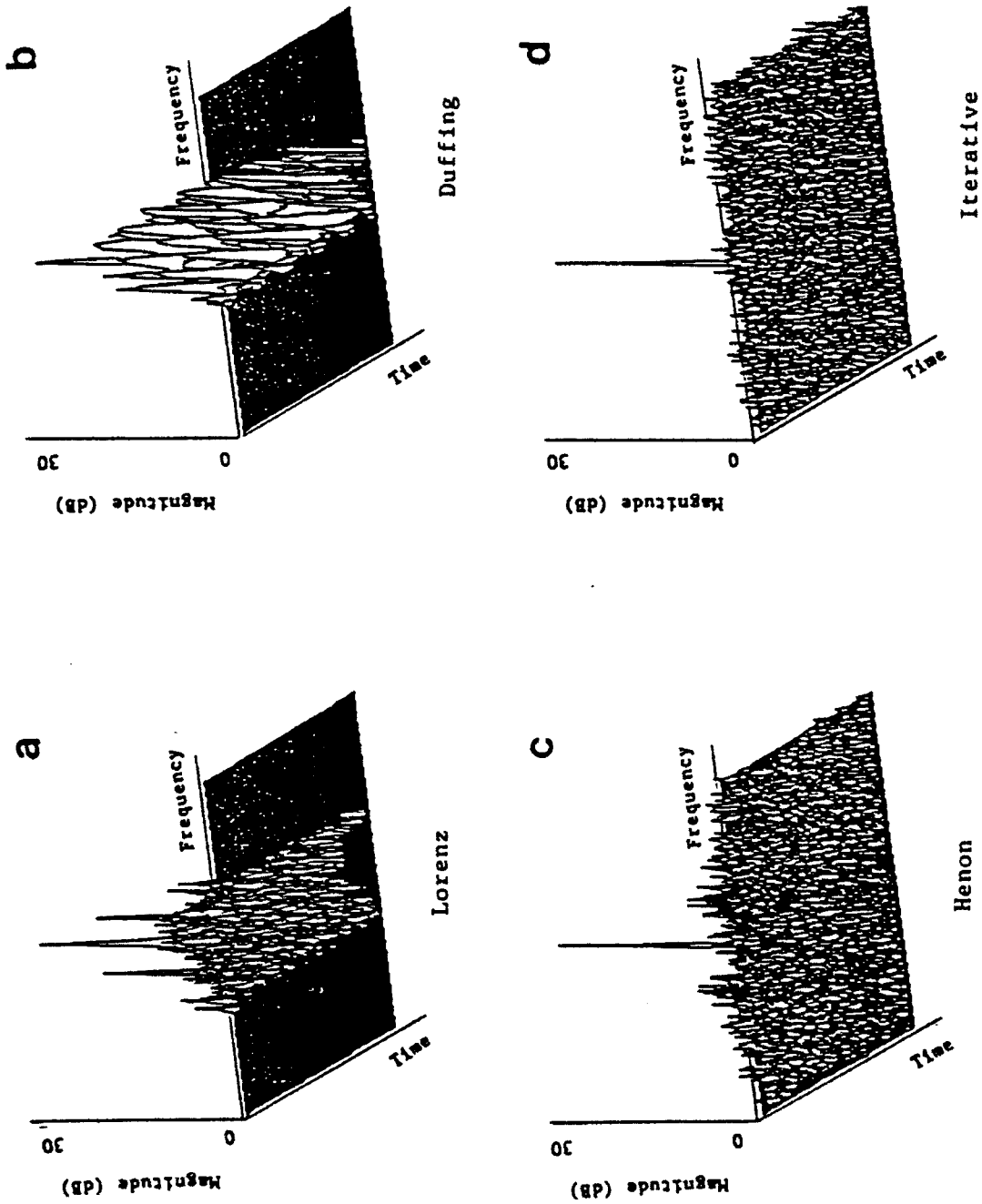


Figure 2.1-5. Ambiguity Functions for Chaotic Waveforms: (a) Lorenz; (b) Duffing; (c) Henon; and (d) Iterative.

2.3 Conventional Metric

The replica correlation technique is applied to each of the four chaotic waveforms in order to provide a familiar frame of reference. This technique is based on a conventional cross correlation of the return signal with a replica of the transmitted signal.

2.4 Qualitative Chaotic Metrics

Qualitative techniques used in this report to describe chaotic behavior include phase plots and close return maps. Other metrics, including the return map and Poincarè sections, are also described for completeness even though they are not used in this study.

2.4.1 Phase Plots

Nonlinear systems that can be modeled by a set of differential equations are amenable to an analysis in phase space. A single point in phase space characterizes the state of the entire system at an instant in time. A sequence of such points (referred to as a *trajectory*) in m-dimensional phase space can be used to characterize the dynamical evolution of that system. The shape that the trajectory assumes is called an *attractor*. The trajectories of a dynamical system can be categorized according to four classes of attractors:

- (1) point attractors
- (2) limit cycles
- (3) quasi-periodic attractors
- (4) strange attractors

Strange attractors are characteristic of chaotic behavior.

The first step in any analysis of suspected chaotic behavior is to reconstruct the phase portrait in order to identify the type of attractor. The reconstruction of phase trajectories from measured data is limited in two respects. First, the true dimension of the system may not be known *a priori*. Second, it is unlikely that all dynamic variables can be observed in the data even if the dimensionality is known. Reconstructed phase plots for the Lorenz, Duffing, Henon and Iterative waveforms were presented previously in Figures 2.1-1 through 2.1-4.

2.4.2 Close Return Map

An approach to the detection of chaotic waveforms referred to as a Close Return Map (CRM) has been shown to be an effective representation for the Lorenz waveform. The CRM is a plot of the time differences, for each of k consecutive reference points of a time series, between the time series origin and occasions when the level of the discretized time series returns to a value within some small window about the reference point. Both the ordinate and abscissa are in units of time.

2.4.3 Other Qualitative Metrics

Poincaré Section. A Poincaré section is the intersection of the m -dimensional phase trajectory in the embedding space with a surface of $m-1$ or fewer dimensions. A useful tool in the visualization of a chaotic system is the intersection of the three-dimensional (3D) trajectories with a two-dimensional (2D) plane. The result is a 2D projection of the strange attractor.

Return Map. A return map is derived from the Poincaré section. If the Poincaré map is one-dimensional (1D), then the n th orbit of the trajectory with the intersecting plane can be described by a single parameter, $x[n]$. The corresponding return map is then simply a plot

of $x[n]$ versus $x[n+1]$ for all n . The shape of the return map provides a qualitative description of the chaotic process itself.

2.5 Quantitative Techniques

Quantitative techniques (or dimensional metrics) used in this report to describe chaotic behavior include correlation dimension and local intrinsic dimension. Other metrics, including information dimension, theoretic entropy and Lyapunov exponent, are also described for completeness even though they are not used in this study.

2.5.1 Correlation Dimension

This method was developed by Grassberger & Procaccia (1983). First, the measured time series t_k , $k = 1, \dots, N$, is embedded in m -dimensional phase space: $X_i = (t_i, t_{i+1}, t_{i+2}, \dots, t_{i+(m-1)})$. Then, a distance metric, d_{ij} , is selected which provides a measure of the separation between points X_i and X_j in phase space. The correlation function is defined as

$$C^m(r) = \frac{2}{N(N-1)} \{ \text{No. of ordered pairs } X_i X_j \text{ such that } d_{ij} \leq r \}, i < j$$

where: m = embedding dimension
 N = number of measured vectors X_i
 r = distance parameter

$C^m(r)$ behaves approximately as r^d , where d is the dimension that is being estimated. In practice, the dimension d can be found by plotting $\log [C(r)]$ versus $\log (r)$ and then graphically determining the slope. For small r , poor statistics result in deviations from a uniform slope; for large r , deviations may be caused by nonlinear effects in the calculations. Consequently, the choice of a meaningful range of r values is critical to this procedure, and recourse is often made to visual inspections of graphical outputs. Once the range of r is selected, the slope can be calculated using a least-squares method.

Several related factors affect the accuracy of the estimation of the correlation dimension including the embedding dimension (m), the delay time (l) used in reconstructing the attractor, the length of the data set (N), the sampling interval used in forming the time series, and the signal-to-noise ratio (SNR) of the signal. For example, a slope value close to that of the embedding dimension may indicate that the embedding dimension selected is too low for that particular attractor. A log-log plot without a region of uniform slope may indicate that the time delay was inappropriate or that an insufficient amount of data was used. Noise tends to increase the dimensionality calculated using this method.

It should also be noted that the correlation dimension is most effective for attractors with dimension less than 4.

2.5.2 Local Intrinsic Dimension

The Local Intrinsic Dimension (LID) is another procedure for classifying a chaotic time series. Computation of the LID requires selection of an embedding dimension, formation of vectors, and selection of local centers on the attractor. For each local center, a data covariance matrix is formed using the nearest neighbors. Singular value decomposition (SVD) is then applied to the matrix and the eigenvalues, calculated from the singular values, are ranked from highest to lowest. All eigenvalues greater than some specified fraction of the highest eigenvalue are considered to be *significant*, and the number of such significant eigenvalues is taken to be the LID for that neighborhood. This process is repeated at each of the local centers, and the average across all of these is called the LID of the attractor. In effect, this procedure yields an estimate of the topological dimension of the data (i.e., the number of orthogonal vectors required to describe the data vectors when averaged over a number of regions in the phase space).

2.5.3 Other Quantitative Metrics

Information Dimension. The information dimension is similar in concept to the correlation dimension, but differs in that it uses only nearest neighbors and is more applicable for chaotic processes of dimension greater than 3. For experimental data, nearest neighbors must be selected which are far enough apart such that the power law represents scaling of the attractor rather than the noise. Issues of concern for this approach are: embedding dimension, length of the data set, processing (or filtering), SNR, and noise reduction.

Theoretic Entropy. In addition to the various dimensions, chaotic attractors can also be characterized by entropies. Such measures have been adapted from ergodic theory and applied to physical measurements.

Lyapunov Exponent. Lyapunov exponents represent the average exponential rates of divergence or convergence of nearby orbits in the phase space. Nearby points in the phase space represent nearly identical states. A time evolution of two trajectories, each beginning with one of the two initially nearby points will show whether the system is creating or losing information. If the trajectories diverge, the system is said to be chaotic. Any system containing at least one positive Lyapunov exponent is labelled chaotic, with the magnitude of the positive exponent reflecting how rapidly the dynamical system becomes chaotic. In the case of a deterministic-chaotic system whose dynamical equations are known, the Lyapunov exponents can readily be calculated from the system Jacobian. For cases involving time-series data, the method attributed to Wolf (1986) can be used. This method tracks the trajectories of two orbits starting on neighboring points in the phase space and then calculates the average rate of their exponential divergence as the trajectories evolve.

3. SOURCES AND EFFECTS OF SIGNAL DISTORTION

3.1 Sources of Signal Distortion

The chaotic metrics described in Section 2 are formulated on the assumption of an undistorted noise-free signal. In the event of distortions caused by transmission through the ocean and/or Doppler shifts, as well as noise contamination, these metrics might not be expected to perform as well as under ideal situations. The purpose of this section is to investigate the effects of the transmission channel, Doppler shifts, and varying signal-to-noise ratio (SNR) values on the viability of these metrics and upon replica correlation.

3.1.1 Propagation through Ocean Channel

A demanding test of the robustness of chaotic waveforms is passage through a realistic ocean waveguide. Rather than generate original ocean impulse response functions, recourse was made to work already accomplished at the Naval Undersea Warfare Center (NUWC) in New London, CT. (This decision was based on guidance received from the project office.) The NUWC data consisted of the frequency response of the ocean based on execution of the Generic Sonar Model (GSM). Two ocean environments were considered covering the frequency band 900-1500 Hz.

A consequence of the decision to use the NUWC data was to band-limit the chaotic waveforms, which are necessarily broadband in nature. Two options were considered: bandpass filtering the broadband chaotic signals; and frequency-compressing then modulating the compressed signals so as to fall within the 900-1500 Hz bandpass. The second option is reversible; that is, the original chaotic waveform can be recovered. The first option, however, destroys part of the signal and therefore, is not reversible. Consequently, in all the analyses that follow, the second option was applied.

It should be noted that frequency compression was achieved by simply assigning a temporal sampling rate to the chaotic waveform samples (4096 points) so that the signal spectra fell in the band 0 - 512 Hz. As shown in Section 2.1, all the chaotic waveforms were generated as solutions to differential or difference equations with no implicit temporal relation, except for Duffing which can be arbitrary. Consequently, the assignment of a temporal sampling rate can be considered an interpretive convenience.

3.1.1.1 Characteristics of Ocean Channel

The two ocean environments considered were both deep-water regions exhibiting a sonic layer, a deep sound channel, and sufficient depth excess to support convergence-zone (CZ) propagation. The corresponding sound speed profiles are presented in Figure 3.1-1.

3.1.1.2 Ocean Impulse Response

In order to utilize the NUWC data, the chaotic waveforms first had to be modulated to be consistent with the 600 Hz bandwidth.

A total of six cases were obtained from NUWC: three cases each for two different environments. All cases involved bistatic geometries with a hull-mounted transmit array (at 18 ft), a submerged target (at 600 ft), and a passive towed array (at 322 ft). The horizontal separation between the submerged target and the two arrays varied from 67 kyds to 71 kyds, and the two arrays were deployed from the same surface ship (i.e., they were separated by a relatively short baseline). The combinations of sound speed profiles and ranges used in these six cases are summarized in Table 3.1-1.

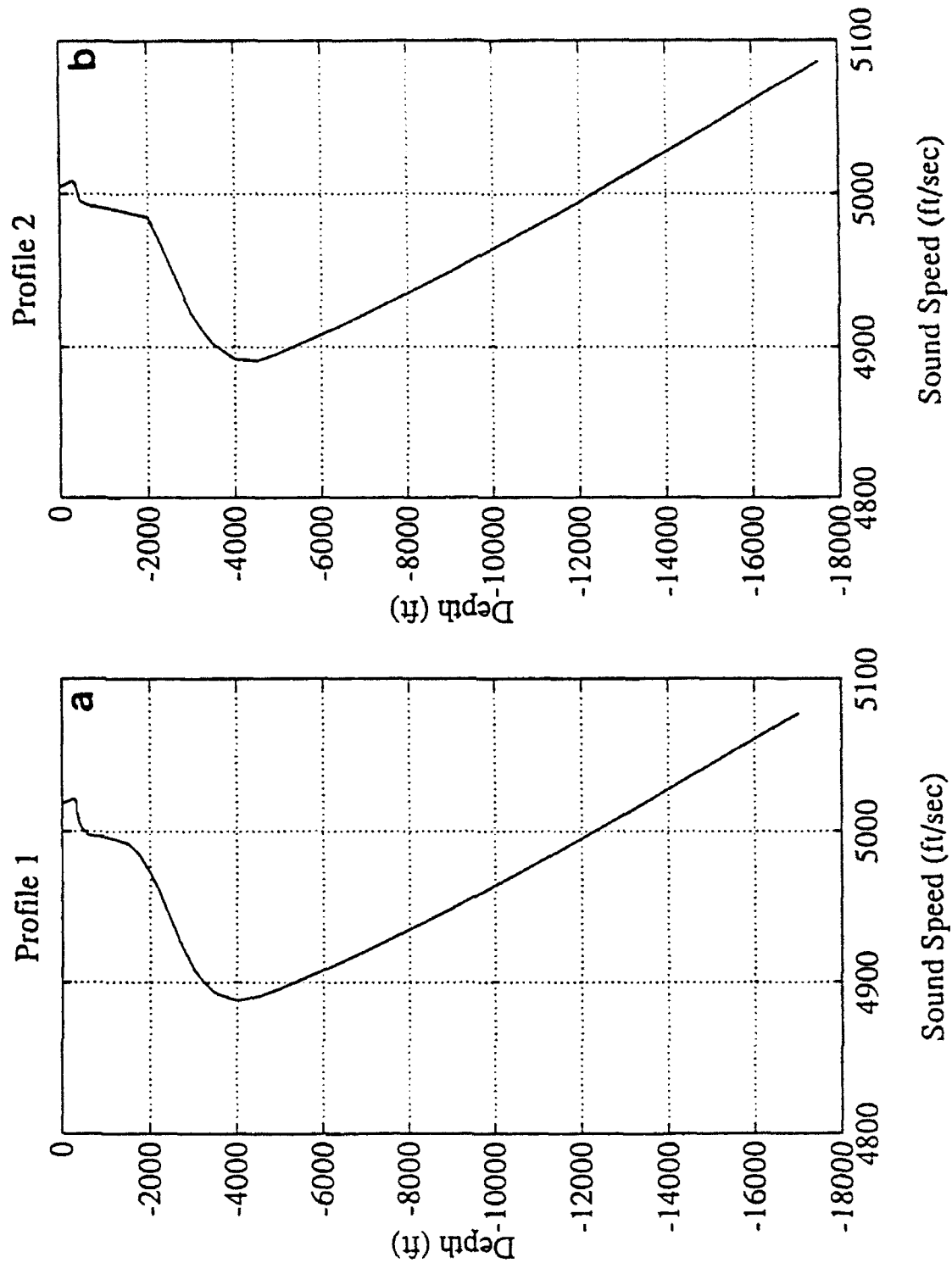


Figure 3.1-1. Sound Speed Profiles Used in Generating Ocean Impulse Responses: (a) Profile 1; and (b) Profile 2.

Table 3.1-1.
Summary of Test Cases

Profile Number	Range		
	67 kyds	69 kyds	71 kyds
Profile 1	Case 1	Case 2	Case 3
Profile 2	Case 4	Case 5	Case 6

For each case, both outbound and inbound ocean frequency responses were provided. The frequency responses were reported in $\frac{1}{4}$ -Hertz intervals over the interval 900.00 Hz to 1499.75 Hz. To the nearest power of 2, this implies a sampling rate of 4096 samples per second in the time domain and a time length of 4 seconds, or a total of 16384 samples. Both the impulse and frequency responses of the outbound and inbound channels of Case 1 are plotted in Figure 3.1-2. A complete set of impulse and frequency responses for all six cases are presented in Appendix B.

3.1.2 Doppler

Motion of both the transmitter-receiver platform and the target will distort the received signal. The signal impinging upon the target will be Doppler-shifted due to the motion of the transmitter and of the target. The resulting echo will then be Doppler-shifted due to the motion of the target and of the receiver. In the analyses that follow, the simplifying assumption was made that the transmitter-receiver is stationary. Justification for this assumption is based on the premise that one can pre- and post-correct own ship's Doppler in the directions of the transmit and receive beams, respectively. Consequently, only the target was assumed to be in motion. The transmitted waveform, therefore, was convolved with the outbound channel, then Doppler-shifted, and then convolved with the inbound channel. Detection was performed by crosscorrelating Doppler-shifted replicas of the transmitted waveform with the signals passed through the ocean channels.

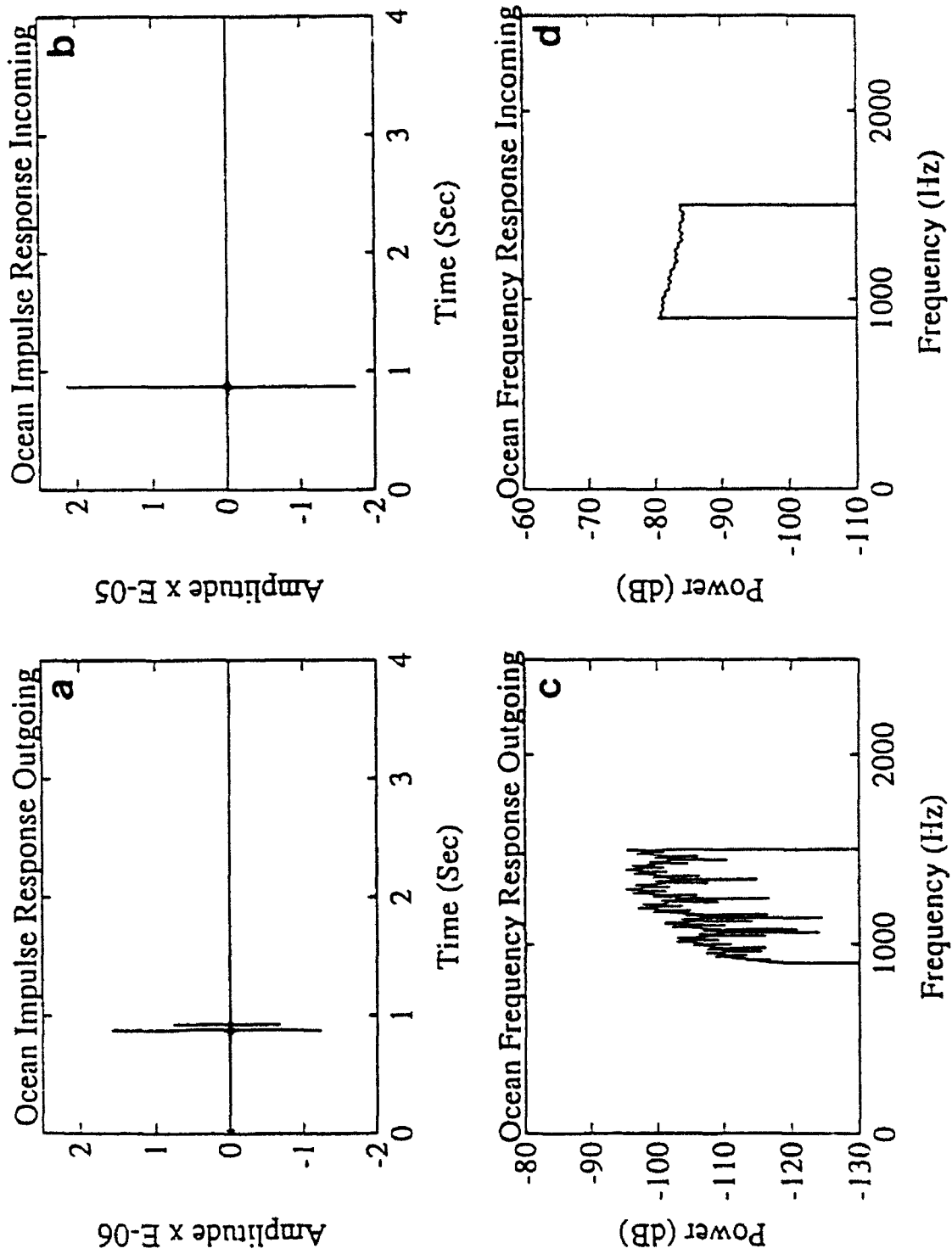


Figure 3.1-2. Case 1 Ocean Impulse Responses for (a) Outgoing Channel and (b) Incoming Channel; and Frequency Responses for (c) Outgoing Channel and (d) Incoming Channel.

Two cases were considered:

- (1) correlate demodulated echo with a modulated-Doppler-shifted replica that has then been demodulated; and
- (2) correlate de-dopplerized, demodulated echo with the replica.

3.1.3 Noise Contamination

Noise contamination of chaotic signals was simulated by adding randomly generated, Gaussian noise to each waveform. The noise was added at levels equivalent to SNRs ranging from -30 dB to +20 dB.

3.2 Effects of Signal Distortion

The effects of distortion upon chaotic waveform echoes are examined. With one exception, it will be shown that, when modulated, the waveform sensitivities to Doppler make them amenable to precise Doppler determination and, hence, target tracking.

Three forms of distortion are examined in the following: that caused by additive noise; by transmission through the ocean; and by Doppler. In Sections 3.2.1 through 3.2.3, the 'Case 1 Ocean' is used. The Case 1 Ocean sound speed profile was presented previously in Figure 3.1-1 and applies to a transmitter/receiver-to-target range of 67 kyds. In all that follows, the target is assumed to be a perfect reflector, introducing no distortion or attenuation to the signal.

The signal recognition and analysis metrics examined in this section include: replica correlation, phase plots, close return map, correlation dimension and local intrinsic dimension.

3.2.1 Replica Correlation

Replica correlation is simply the correlation of the received echo with a replica of the transmitted signal. The effects upon replica correlation of additive noise and the two ocean environmental scenarios at the three ranges provided by NUWC are examined for Doppler shifts caused by 19.5 knots to 20.5 knots target motion. Only the target is assumed to be in motion, because it is possible to compensate for transmitter-receiver motion.

3.2.1.1 *Noise Contamination*

Noise contamination of chaotic signals was simulated by adding randomly generated Gaussian noise to each waveform. The noise was added at levels equivalent to SNR's ranging from +20 dB to -30 dB. The noisy signals were then cross-correlated with the pure signal to determine the SNR at which the correlations are visually undetectable. This procedure provides an indication of the robustness of the various chaotic waveforms to noise contamination. The results for the Lorenz waveform are presented in Figures 3.2-1 and 3.2-2. Complete results for the Lorenz, Duffing, Henon, and Iterative waveforms are presented in Appendix C. Note the scale change between Figure 3.2-1 (correlation magnitude 0-1) versus Figure 3.2-2 (correlation magnitude 0-0.2). In Appendix C it can be seen that the correlations with the Duffing waveform appear similar to what one would expect for a sine-wave-like signal. This follows from the fact that the Duffing is driven by a cosine.

3.2.1.2 *Propagation and Doppler*

Figure 3.2-3 illustrates correlation of the Lorenz echo, passed through the Case 1 ocean environment (using Profile 1, as illustrated previously in Figure 3.1-1) at a range of 67 kyds, with a replica of the transmitted signal. The correlations shown in Figure 3.2-3 were calculated by cross-correlating the received echo with Doppler-shifted replicas. The

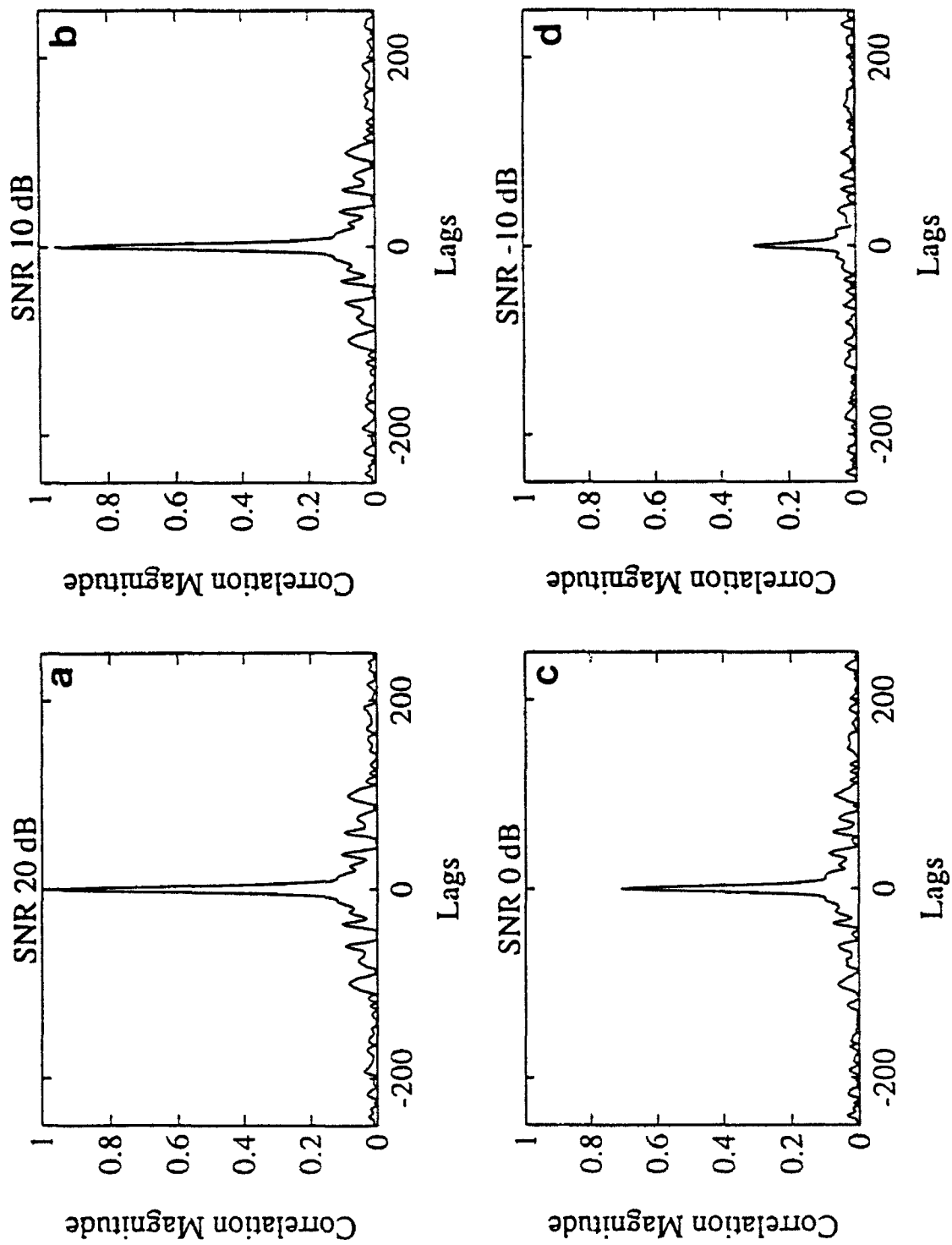


Figure 3.2-1. Replica Correlations for Noise-Contaminated Lorenz Echoes for Selected SNR Values: (a) 20 dB; (b) 10 dB; (c) 0 dB; and (d) -10 dB.

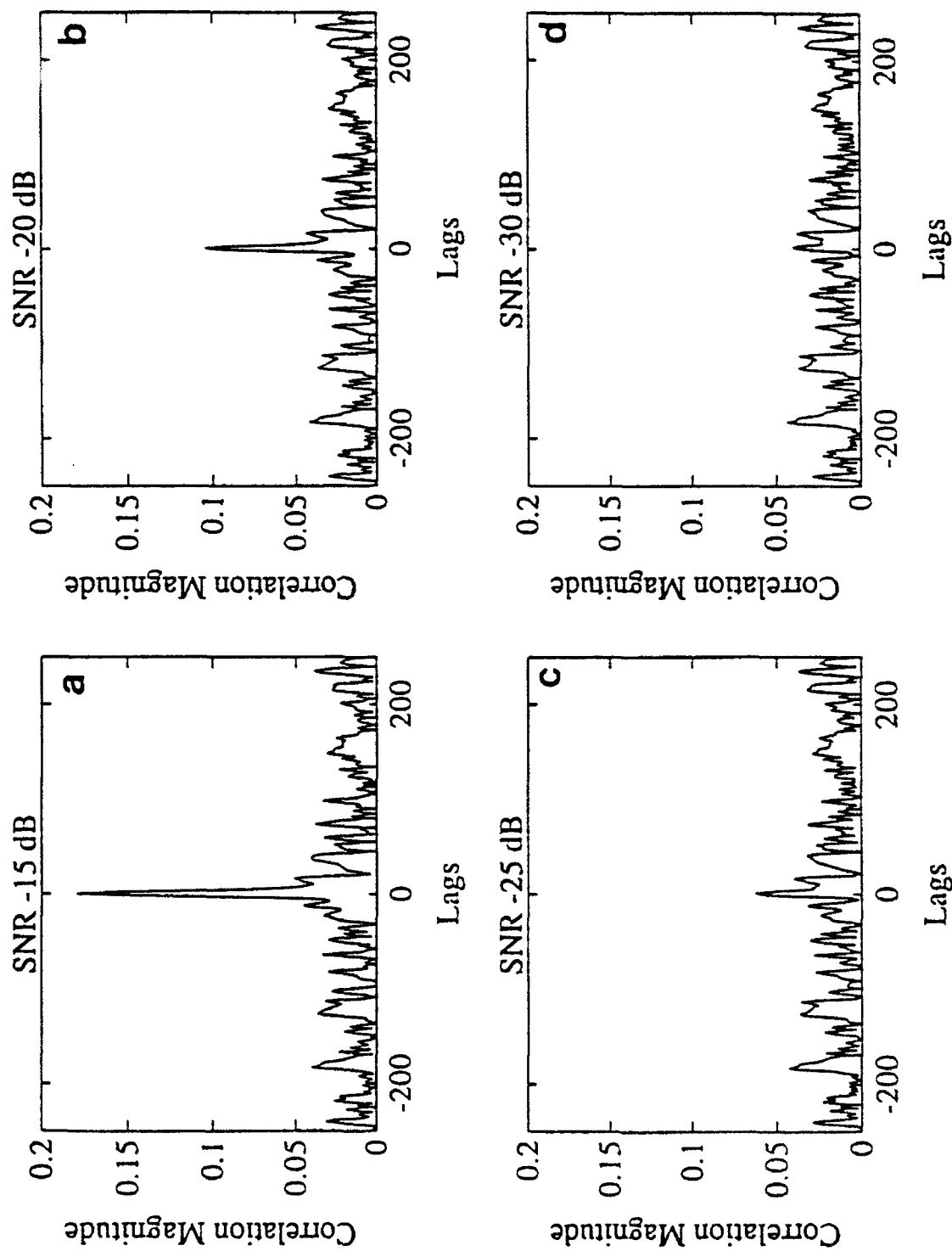


Figure 3.2-2. Replica Correlations for Noise-Contaminated Lorenz Echoes for Selected SNR Values: (a) -15 dB; (b) -20 dB; (c) -25 dB; and (d) -30 dB.

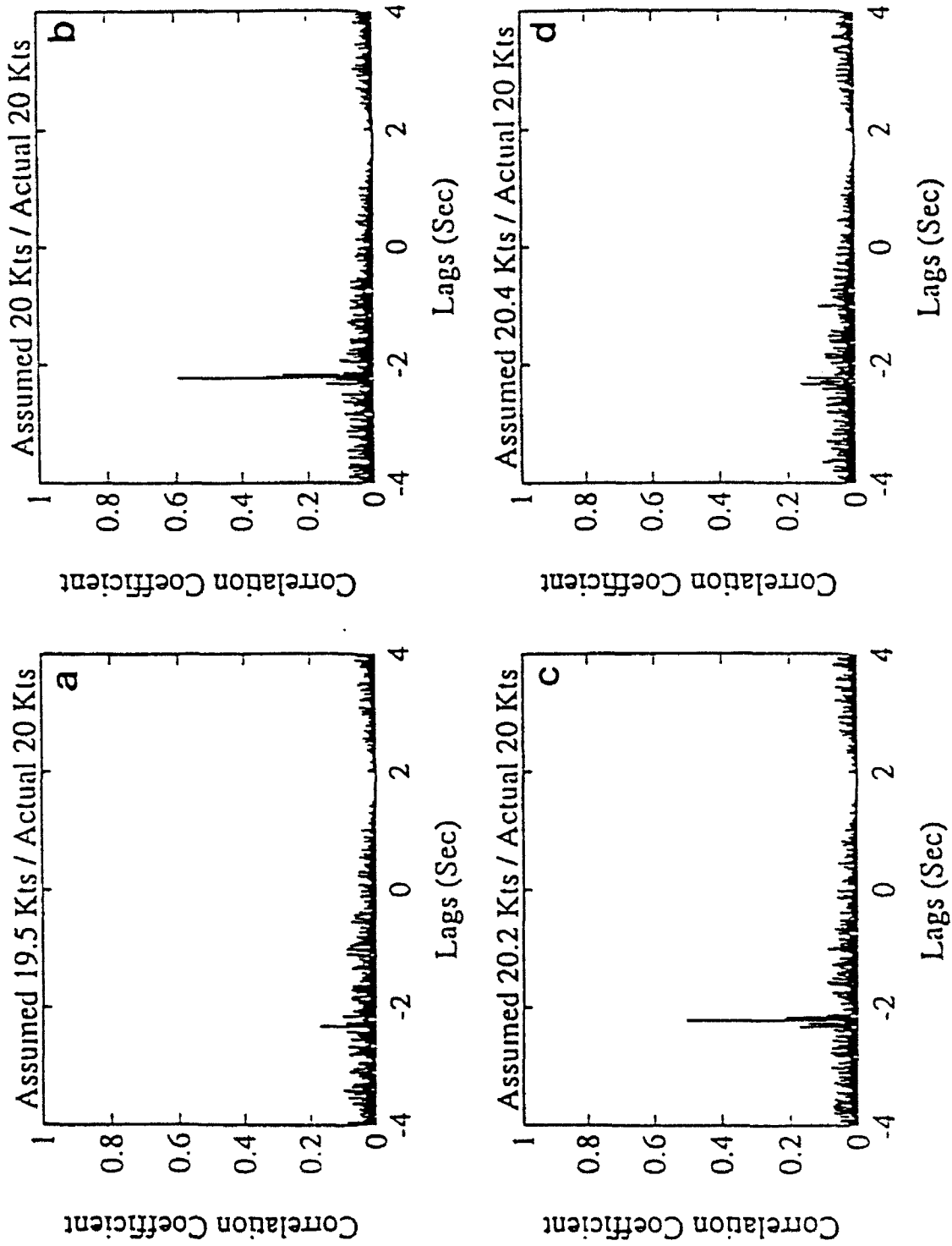


Figure 3.2-3. Replica Correlations for Doppler-Shifted Lorenz Echoes in Case 1 with an Actual Doppler of 20 Knots and Assumed Dopplers of: (a) 19.5 Knots; (b) 20 Knots; (c) 20.2 Knots; and (d) 20.4 Knots.

absolute values of the correlations are shown in the figures. It is clear that the modulated signal is very sensitive to Doppler shifts. Additional figures, contained in Appendix D, show that this observation applies to all the environment-range combinations provided by NUWC (recall Table 3.1-1).

Another observation that can be made from Figure 3.2-3 and those in Appendix D is that, even when the replica is shifted by the correct Doppler, the peak correlation is well below 1. The reasons for this are that the ocean channel distorts the signal, but perhaps more importantly, the Doppler-shifted echo is convolved with a slightly different band of the ocean channel frequency response than would be a non-Doppler-shifted signal. This is illustrated in Figure 3.2-4 where both the echo and replicas in the top of the figure have no Doppler shift, while in the bottom of the figure they both have Doppler shifts caused by 20 knots of relative target motion. The correlation of the no-Doppler case is seen to be higher than for the Doppler-shifted case.

Much of the sensitivity to Doppler is caused by the fact that the signal has been modulated by a 944 Hz carrier frequency. Figure 3.2-5 illustrates replica correlations when the modulating carrier frequency is only 50 Hz. The sensitivity is reduced by a factor of almost ten; however, it should be noted that the signal was not propagated through the ocean. This follows from the fact that the signal occupies the band 50 Hz to 562 Hz, which is outside the 900 Hz to 1600 Hz band of the ocean models.

An additional replica correlation approach was examined in which the echo was 'de-Dopplerized', demodulated, then correlated with a replica of the transmitted signal. The results of this approach are illustrated in Figure 3.2-6. Upon comparing Figures 3.2-6 with 3.2-3, it is seen that there is no advantage to this approach; operationally it would be much more computationally intensive.

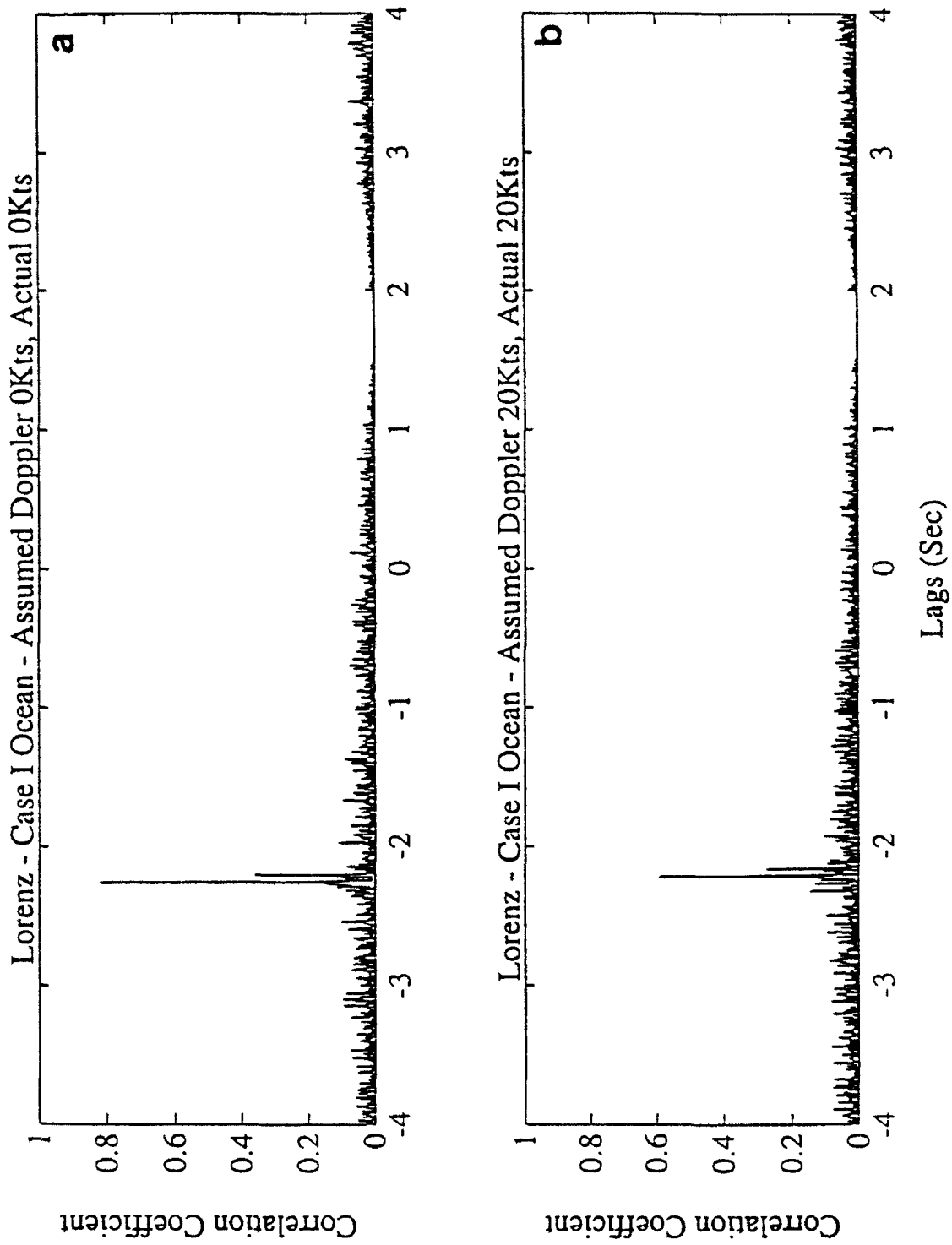


Figure 3.2-4. Replica Correlations Illustrating the Effect of Doppler: (a) No Doppler Shift to Either Replica or Echo; (b) 20 Knot Doppler Shift of Both Replica and Echo.

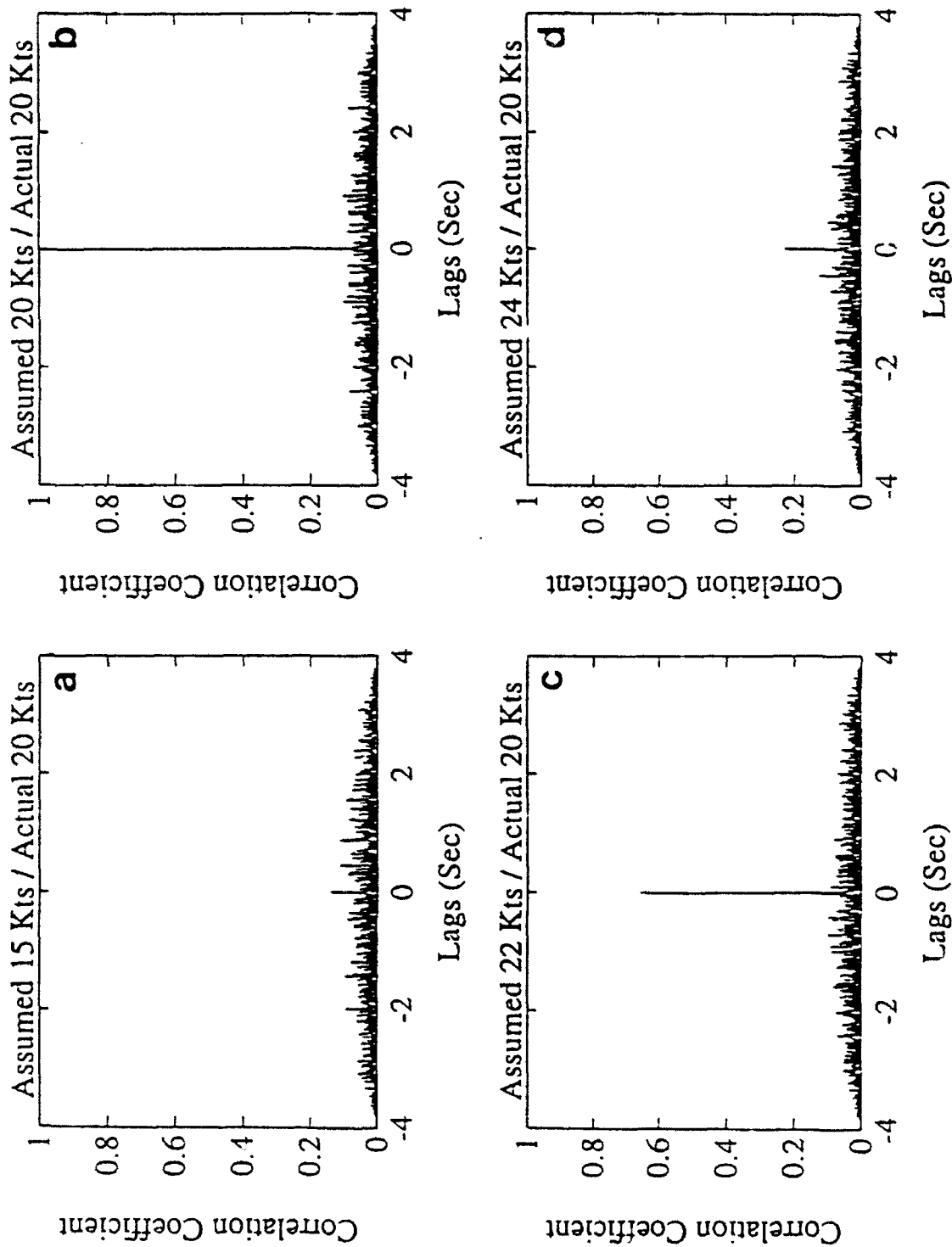


Figure 3.2-5. Replica Correlations for Doppler-Shifted Lorenz Echoes with an Actual Doppler of 20 Knots and Assumed Dopplers of : (a) 15 Knots; (b) 20 Knots; (c) 22 Knots; and (d) 24 Knots. Transmitted Signal is Bandshifted 50 Hz, and There is no Transmission Distortion.

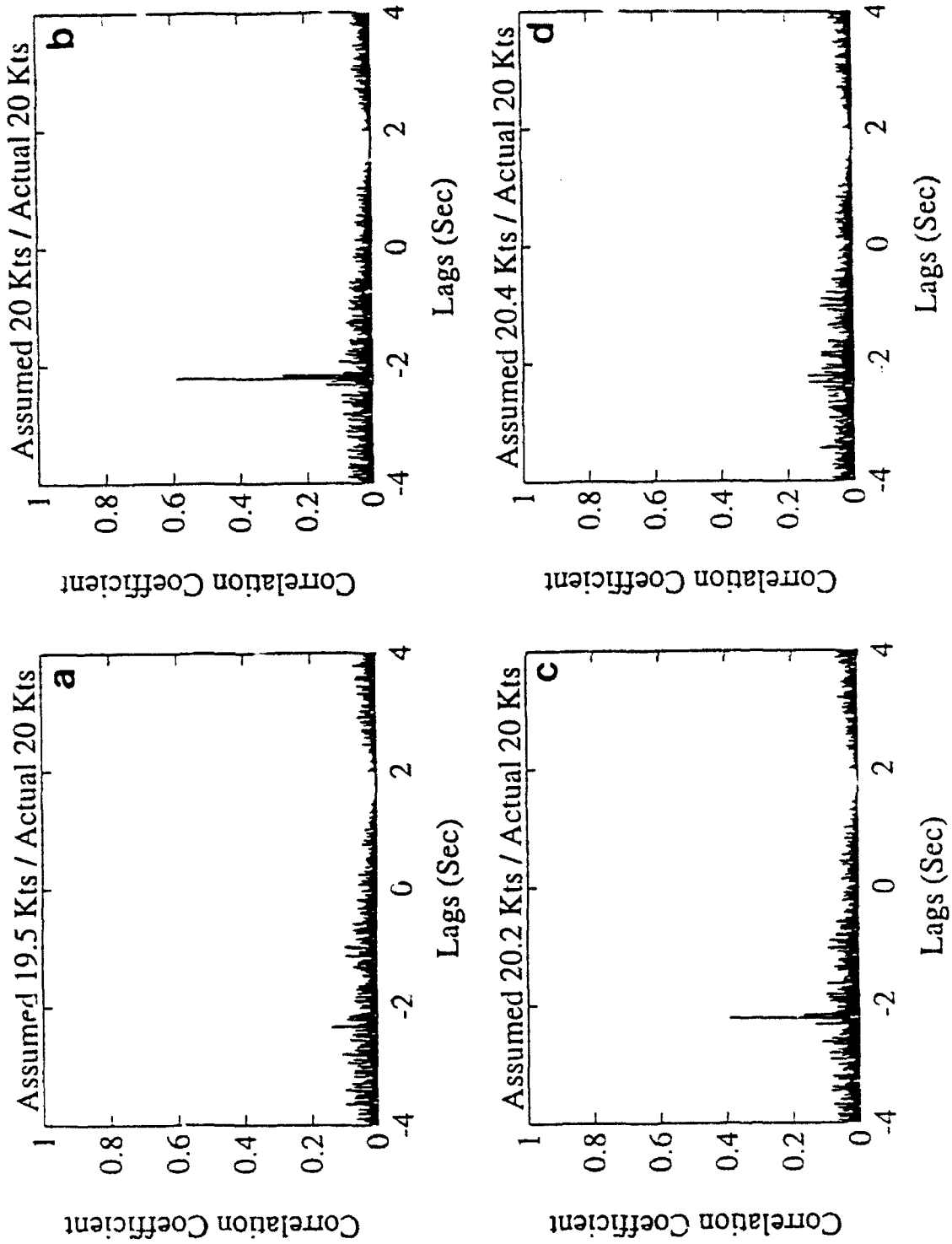


Figure 3.2-6. Replica Correlation with, 'De-Dopplerized' and Demodulated Lorenz Echo.

3.2.2 Qualitative Assessments

3.2.2.1 *Phase Plots*

Phase trajectories characterize the dynamical evolution of a chaotic system. It would be hoped, therefore, that the echoes of chaotic waveforms would preserve some degree of the dynamics and hence, that the original waveform would be recognizable from the phase plot of the echo. It will be seen that our signal distortions of a modulated signal are generally too great to preserve the phase plots, using an embedding dimension of two. Illustrated in Figure 3.2-7 is a series of phase plots of the Lorenz waveform. The figure consists of two columns of four panels. The first column examines the distortion of phase plots due to the transmission channel alone, with no Doppler. The first panel (a) of the left column is a phase plot of the original waveform. The second panel (b) of the left column shows the phase plot after modulating then demodulating the signal. Any difference between the first and second panels is due to computer truncation error. The third panel (c) of the left column is the phase plot of signal at the target after demodulation. This signal has been transmitted one way through the ocean then demodulated. The fourth panel (d) on the left is a phase plot of the demodulated echo. This signal has been transmitted and echoed back to the receiver then demodulated. The second column of panels examines the effects of Doppler. The first panel (e) in this column is the phase plot of the baseband Doppler-shifted signal. The second panel (f) is a phase plot when the signal has been modulated (944 Hz) then Doppler-shifted. In the third panel (g) the signal has been modulated, transmitted, Doppler-shifted, then demodulated at the target. The fourth panel (h) in the second column is the demodulated, Doppler-shifted echo at the source-receiver. Figure 3.2-7 shows that the Lorenz phase plot is intolerant of distortion, either by ocean propagation or by Doppler shift. This intolerance is also exhibited by the Duffing, Henon and Iterative waveforms as can be seen in Appendix E. The figures of Appendix E present the same information described above, but for all four waveforms. Extreme intolerance to Doppler shift is seen of the Henon and Iterative waveforms, even when the shift occurs over

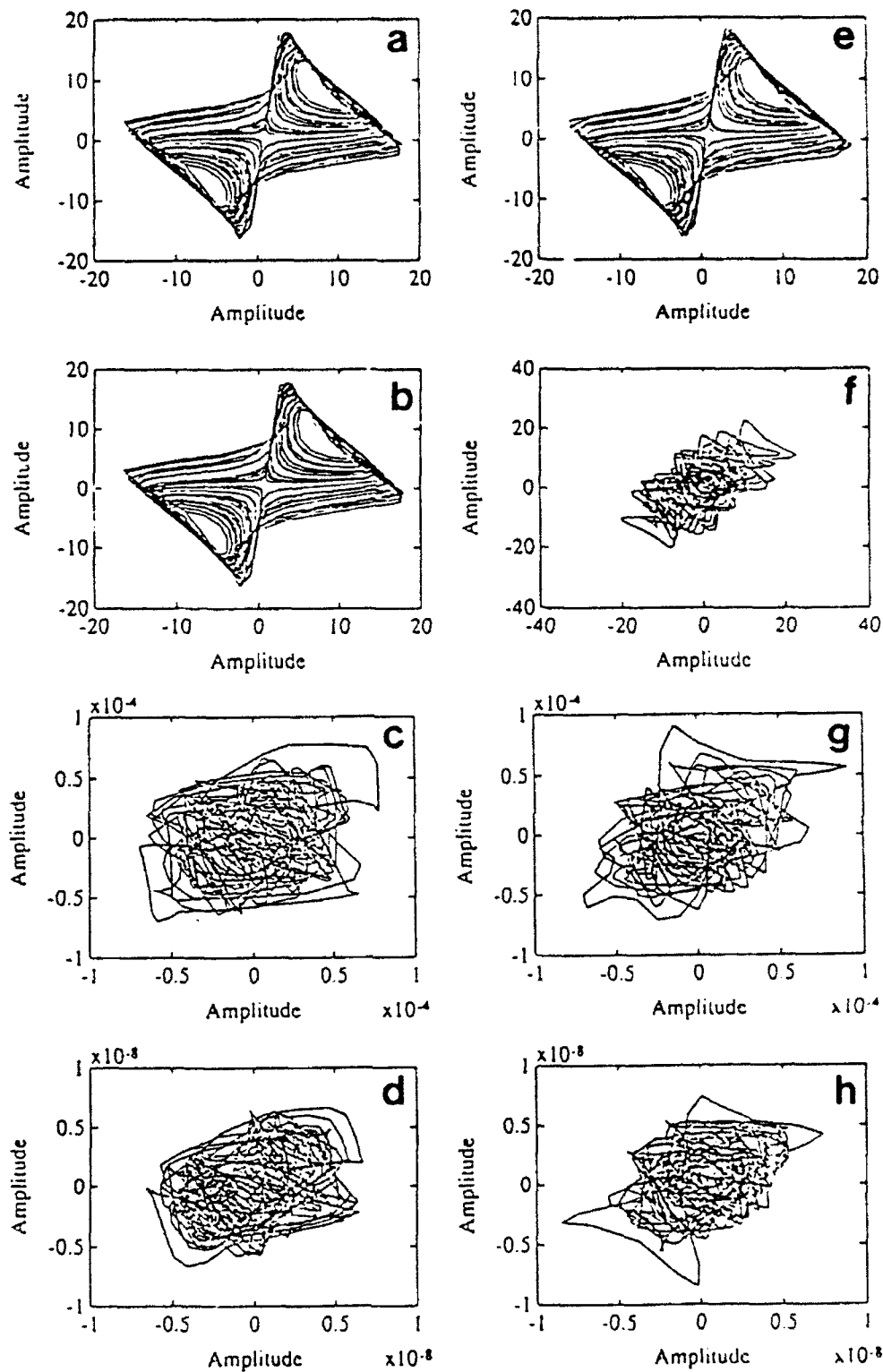


Figure 3.2-7. Phase Plot of the Lorenz Waveform: (a) original; (b) modulated, then demodulated; (c) at target; (d) of echo; (e) Doppler-shifted; (f) modulated then Doppler-shifted; (g) at target, Doppler-shifted; (h) Doppler-shifted echo.

the baseband (0 - 512 Hz). The Duffing waveform phase plot is the most resistant to the distortions.

Presented in Appendix F are selected stereoscopic projections. These plots are presented for those individuals who are adept at visualizing three dimensions from the stereo pairs (e.g., Broomhead & King, 1986).

3.2.2.2 *Close Return Map*

The Close Return Map (CRM) is an approach to the detection of chaotic waveforms, previously discussed in Section 2.4.2, that is a particularly effective metric for the Duffing and Lorenz waveforms. Briefly, the CRM is a plot of the time difference between a time series origin, for K consecutive reference points of the time series, and occasions when the level of the discretized time series returns to a value within some small window about the reference point. Both the ordinate and abscissa are in units of time. Distinctive patterns are observed from such figures, for example, those illustrated in Figure 3.2-8. Figure 3.2-8 illustrates the effects of random Gaussian noise on the CRM of the Lorenz waveform as the SNR decreases; Figure 3.2-8(d) is the CRM of Gaussian noise alone. Noise can be seen to introduce a random scatter to the CRM data points.

Figure 3.2-9 (a) illustrates the effect of Doppler on the CRM. Doppler was introduced in the manner described previously in Section 3.1.2, corresponding to a target moving at a relative speed of 20 knots. The Doppler shift is seen to distort the pattern relative to that shown previously in Figure 3.2-8. However, a clear pattern related to the original can be seen in Figure 3.2-9(a). Figure 3.2-9(b) illustrates the distortion caused by propagation through the ocean channel in the band 900 - 1500 Hz. While the distortion differs from that caused by Doppler, an obvious pattern nonetheless remains. The Case 1 ocean channel described in Section 3.1.1 was used as the propagation channel. Figure

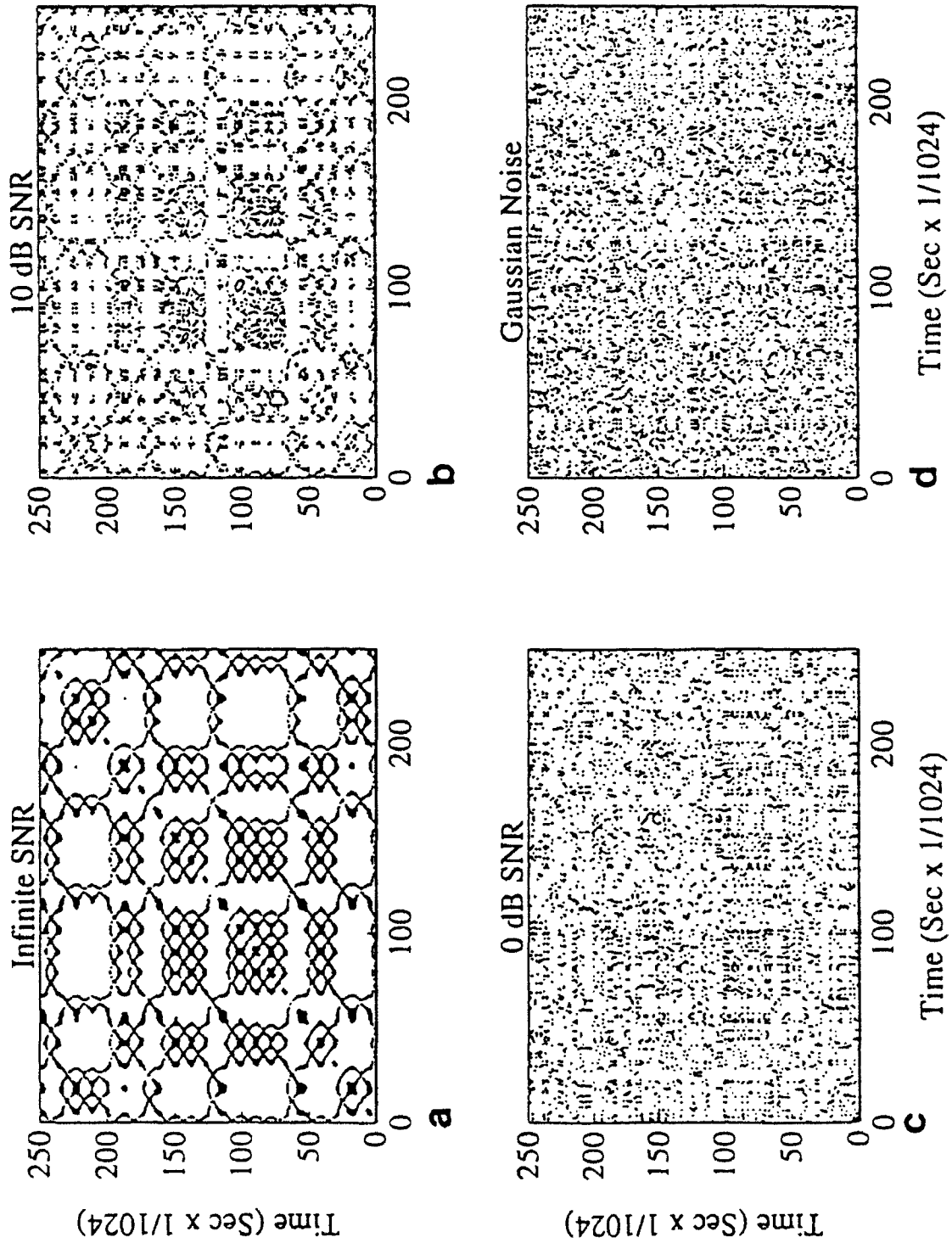


Figure 3.2-8. Close Return Maps of Lorenz Waveform with Various Levels of Added Noise, and Gaussian Noise Alone.

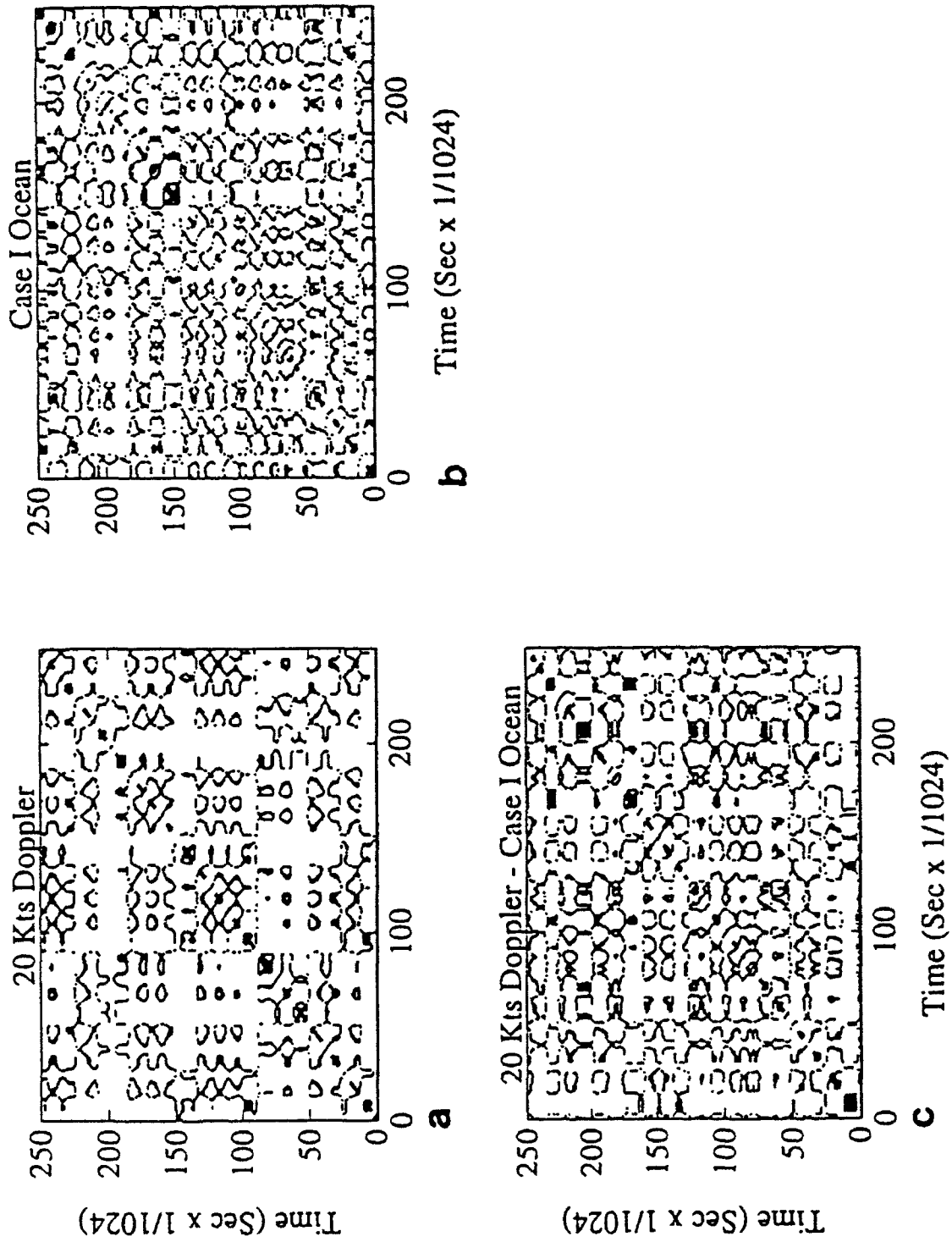


Figure 3.2-9. Close Return Maps of Distorted Lorenz Waveform.

3.2-9(c) illustrates the combined distortion resulting from both propagation through the ocean and a Doppler shift. Again, a distorted but clearly apparent pattern is observed.

Figure 3.2-10 is the CRM of the Duffing waveform. Again a distinctive pattern is observed which differs from that of the Lorenz waveform. Figure 3.2-10(b) is the same as Figure 3.2-10(a) except that noise has now been added at a SNR of 10 dB. Figure 3.2-10(c) illustrates the effects of propagation (Case 1 ocean) and Doppler (20 knots relative motion) on the Duffing CRM. Noise added at a SNR of 10 dB starts to obscure the patterns, as can be seen in Figure 3.2-10(d).

The utility of the CRM is diminished for the Henon (and Iterative) waveform because of the *tightness* of the patterns, as can be seen in Figure 3.2-11(a). If the window width used to define close returns is reduced so as to produce a plot less dense in dots, the patterns are lost. Figure 3.2-11(b) is the CRM of the Henon waveform propagated through the Case 1 ocean, Doppler-shifted at relative motion of 20 knots, with noise added at a SNR of 10 dB. In order to see a pattern, the close return window width had to be broadened, resulting in a dense plot as seen in the figure. The problem is that, if the window width is too broad (i.e., dots are dense enough to see a pattern in the distorted Henon waveform), noise alone will also exhibit a pattern as shown in Figure 3.2-11(c). Only at the density of dots used for the Duffing and Lorenz waveforms does noise become a random distribution of dots. In other words, the close return window width must be small enough to preclude adjacent points in a discretized time series.

3.2.3 Quantitative Assessments

3.2.3.1 *Correlation Dimension*

The correlation dimension is one of the invariant metrics that provides a measure of the density of embedded points occupying a higher dimensional space. The invariance of

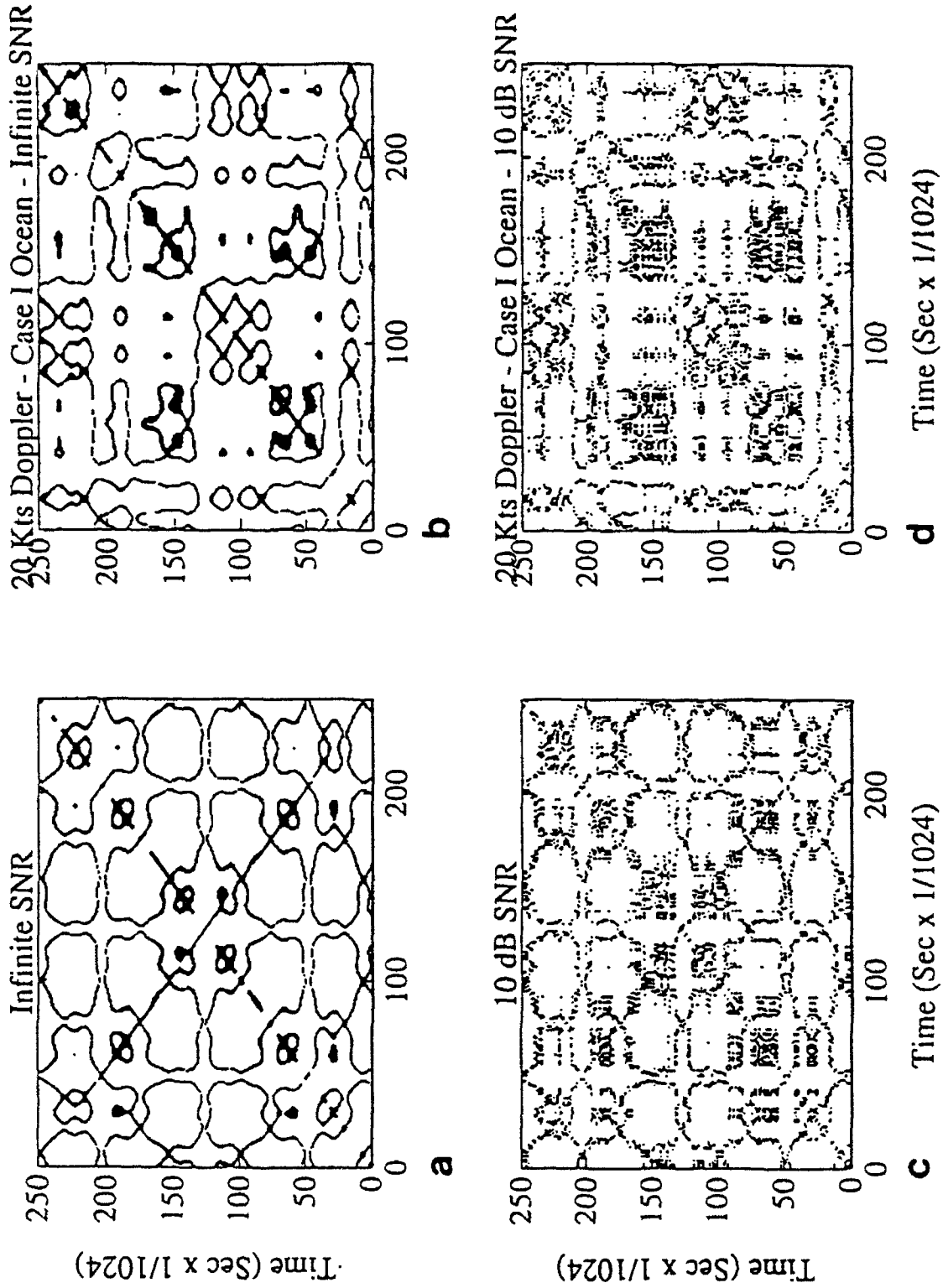


Figure 3.2-10. Close Return Maps of Distorted Duffing Waveform.

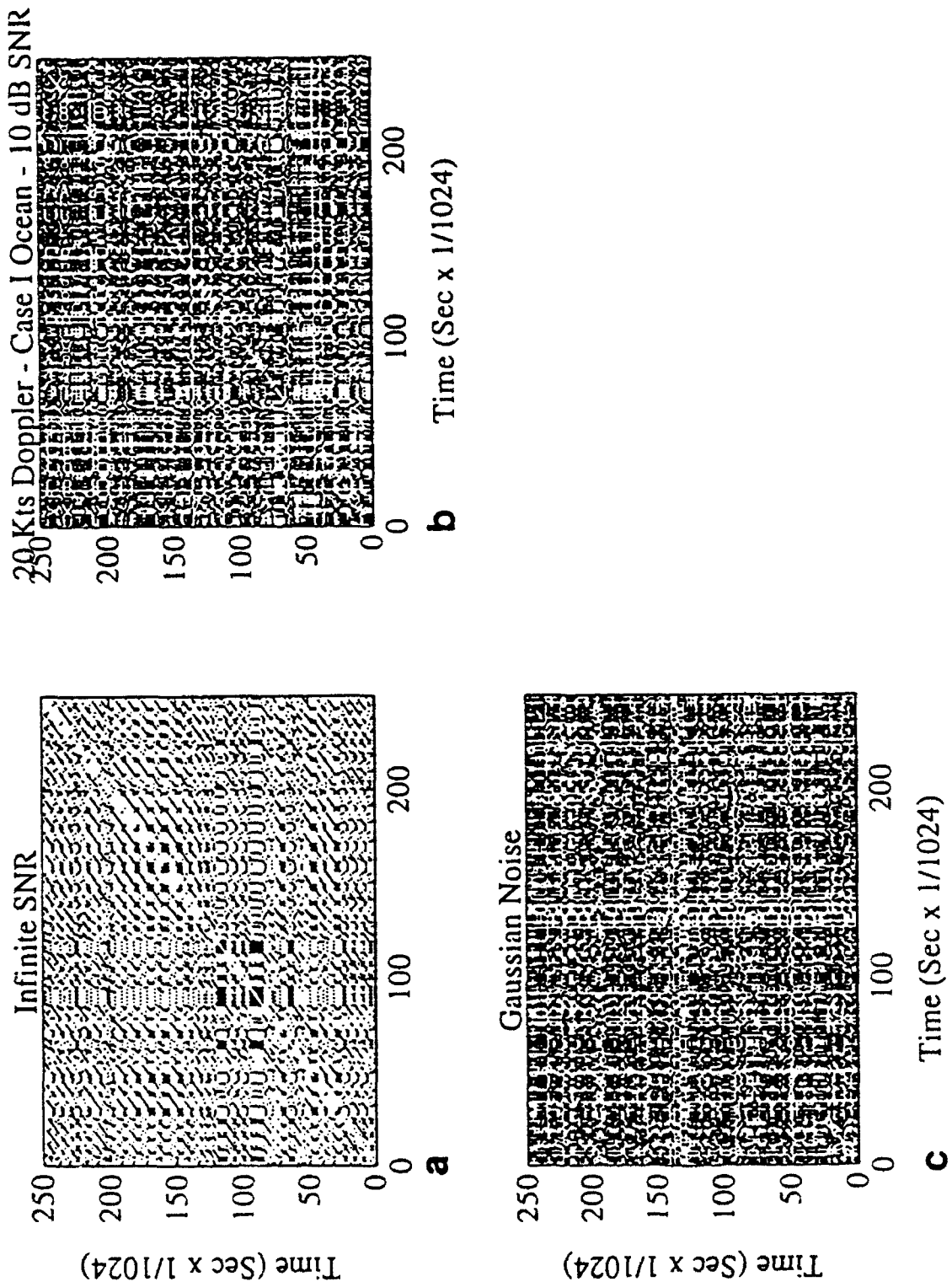


Figure 3.2-11. Close Return Maps of Distorted Henon Waveform.

this metric under ocean propagation and Doppler distortion is examined. It will be seen that these distortions increase the correlation dimension, but not at the rate that would be expected for Gaussian noise.

Table 3.2-1 summarizes the estimates of the correlation dimension of the four chaotic waveforms examined in this report. It will be recalled that the correlation dimension is the slope of the linear equation relating the logarithms of the range and domain of the correlation function defined in section 2.5.1. In practice estimates of these linear equations are not always linear, thereby requiring judgement as to the region of linearity. Because of this subjectivity, plots are provided in Appendix G of the curves used to estimate the correlation dimensions of Table 3.2-1.

The estimated correlations dimensions of a sine wave, FM slide (chirp), and Gaussian noise are also given in Table 3.2-1 to provide 'baselines.' Not all matrix cells are completed in Table 3.2-1 for two reasons. First, this procedure is very computationally intensive. Second, these results are only intended to indicate trends. For the sine wave the correlation dimension was found to be 1. A five-dimensional embedding was used as well as a time lag (τ) of one sample. The dimension of the FM slide was estimated to be 2. Both the sine and FM slide are non-chaotic waveforms with integral-valued dimensions. The estimated correlation dimension of Gaussian noise can be seen from the table to increase with increasing embedding dimension, approximately 4.71, 6.25, and 9, for embedding dimensions 5, 7, and 10 respectively. This is to be expected because the dimension of noise is infinite; hence, the estimate of the correlation dimension should be approximately equal to the embedding dimension used to make the estimate.

The estimated correlation dimension of the undistorted Lorenz waveform embedded in four dimensions is approximately 2.02. When the signal is propagated through the ocean and Doppler-shifted, the dimension is seen to increase to about 3.33 and 3.5 for embedding dimensions of 5 and 10, respectively. These increases are well below the embedding

dimensions. When distorted by Doppler alone, the dimension is about 3.9 (estimated from Figure G-9), suggesting that a larger sample size might be required in order to obtain a better estimate.

Table 3.2-1.
Correlation Dimension

Waveform	Embedding Dimension			
	4	5	7	10
Sine Wave		1.0		
FM Slide (Chirp)		2.0		
Gaussian Noise		4.71	6.25	9.0
Lorenz Undistorted	2.02			
Doppler-Shifted Lorenz Echo		3.33		3.5
Doppler-Shifted Lorenz				3.94
Duffing Undistorted	2.27			2.3
Doppler-Shifted Duffing Echo		2.6		3.5
Doppler-Shifted Duffing				2.5
Henon Undistorted		1.22		
Doppler-Shifted Henon Echo		3.75	4.35	5.0
Doppler-Shifted Henon				3.0
Iterative Undistorted		1.0		
Doppler-Shifted Iterative Echo			4.75	7.33
Doppler-Shifted Iterative				3.5

The correlation dimension of an undistorted Duffing waveform embedded in four dimensions is seen to have been estimated at about 2.27, implying a fractal dimension. When embedded in 10 dimensional space the estimated correlation dimension is about 2.3. These values demonstrate the invariance of the correlation dimension (i.e., the correlation dimension does not change with embedding dimension once a sufficiently high dimension is

used to embed the attractor). The estimated correlation dimension of a Doppler-shifted Duffing echo (Case 1 ocean) embedded in 5 and 10 dimensions were found to be 2.6 and 3.5, respectively. Finding a linear portion of the curves shown in Appendix G, Figures G-12 and G-13, from which the correlation dimensions can be estimated is difficult, reducing the confidence in the estimates. Nevertheless, the increase in correlation dimension with embedding dimension suggests that the distortions caused by modulating, ocean propagation, Doppler shifting, and demodulation introduce some 'noise.' However, the increase is far below the embedding dimension. The correlation dimension estimate of a Doppler-shifted signal without ocean propagation embedded in 10 dimensional space is only 2.5 compared with 2.3 for the undistorted waveform. This suggests, at least in the case of Duffing, that Doppler does not significantly affect the correlation dimension.

A correlation dimension of 1.22 was estimated for the undistorted Henon waveform using an embedding dimension of 5. The correlation dimension estimates increase to 3.75, 4.35, and 5 for the Doppler-shifted Henon echo when embedded in dimensions of 5, 7, and 10, respectively. Again, we see that the signal distortions have effectively added noise, worse than in the case of the Duffing waveform, but still well below the embedding dimension. The correlation dimension estimate of a Doppler-shifted signal without ocean propagation when embedded in 10 dimensional space is 3. Again, we see a significantly reduced correlation dimension relative to the propagated echo. However, the correlation dimension of this Doppler-shifted signal is well above the undistorted signal.

The estimated correlation dimension of the undistorted Iterative waveform is 1, which is surprisingly non-fractal. The dimensional estimates of the Doppler-shifted Iterative echo are about 4.75 and 7.33 when embedded in dimensions of 5 and 10, respectively. These estimates resemble noise much more than was observed with the Lorenz and Duffing waveforms. When the signal is distorted by Doppler alone, the correlation dimension drops significantly, to about 3.5.

3.2.3.2 Local Intrinsic Dimension

Computation of the Local Intrinsic Dimension (LID) requires selection of an embedding dimension, local vectors on the attractor, and the identification of the N nearest neighbors of each local center. For this report 25 local vectors were selected. The 29 nearest neighbors (vectors) to each local vector were identified then averaged with the local vector to find a local center. At each local center a matrix was formed of the difference between each vector in a local neighborhood and its center. The LID was then found by averaging the number of eigenvalues of each matrix within 10% of the value of the largest eigenvalue of that matrix. This procedure yields an estimate of the topological dimension of the data.

Table 3.2-2 gives the LIDs of the Lorenz, Duffing, Henon, and Iterative waveforms using embedding dimensions of 10, 15 and 20. LIDs of the undistorted and distorted waveforms are given. The distortions include propagation through the Case 1 ocean environment with and without a Doppler shift. The Doppler shift is equivalent to 20 knots target motion. Also included in the table is the LID of Gaussian noise. The LIDs of Gaussian noise are seen to equal the embedding dimension. The distorted Henon and Iterative waveforms give rise to noise like LIDs. The LIDs of the distorted Lorenz and Duffing waveforms, however, are well below the embedding dimension suggesting that the LID metric might be of value in identifying these two waveforms.

Table 3.2-2.
Local Intrinsic Dimension (LID)

Waveform	Embedding Dimension		
	10	15	20
Gaussian Noise	10	15	19.84
Lorenz	2.4	2.16	2.16
Propagated Lorenz	6.8	5.2	5.48
Propagated Doppler-Shifted Lorenz	7.04	5.88	6.56
Duffing	3.4	3.44	3.2
Propagated Duffing	4.52	4.8	5.2
Propagated Doppler-Shifted Duffing	4.72	5.4	5.92
Henon	3.24	5.88	9.8
Propagated Henon	10	14.76	17.92
Propagated Doppler-Shifted Henon	10	14.96	18.92
Iterative	4	11.8	18.36
Propagated Iterative	10	14.96	19.36
Propagated	10	15	19.56

Notes: (1) 30 vectors in each local neighborhood, eigenvalues below 10% of the highest rejected; (2) 25 local neighborhoods used in LID average; (3) propagation is through Case 1 ocean, Doppler shift at 20 knots target motion.

4. NOISE REDUCTION

A potentially valuable outgrowth of chaotic and non-linear signal processing research has been the development of techniques to reduce noise from noisy signals (Cawley & Hsu, 1992; R. Hughes, private communication). A particularly simple, but effective, technique has been developed under this contract. The common thread in all the techniques is to extract a signal's attractor, embedded in N-dimensional space, from the noisy attractor. The signal must be structured, i.e. of low dimensionality, but not necessarily chaotic.

The technique developed under this contract is to simply average M nearest neighbors of every point on the noisy signal's N-dimensional attractor. The resulting 'average attractor' is then 'disembedded' by averaging the appropriate components of the vectors that constitute the average attractor. The parameters that must be specified are the embedding delay, the embedding dimension, and the number of nearest neighbors. The efficacy of this simple technique is illustrated in Figures 4-1 and 4-2. Time series of the Lorenz waveform (a), Gaussian noise (b), the sum of the Lorenz waveform and Gaussian noise (c), and of the noise reduced estimate of the waveform (d) are illustrated in Figure 4-1. The SNR of the signal plus noise is 0 dB. The results shown in Figure 4-1d are from three iterations of the noise reduction technique starting with the time series shown in Figure 4-1c, using an embedding delay of 1 data sample, embedding dimension of 15, and 15 nearest neighbors in the averages. Figure 4-2 presents the power spectra corresponding to the time series shown in Figure 4-1. Note that the spectrum of the noise reduced signal resembles that of the signal, as contrasted to what one would expect from a low pass filter. Had the signal been low pass filtered the spectrum would rapidly decrease beyond the cutoff frequency.

A final example of the utility of the noise reduction algorithm is the enhancement of the close return map illustrated in Figure 4-3. Panel (a) shows the close return map of the undistorted Lorenz waveform. In panel (b) the waveform has been contaminated with

Gaussian noise at 0 dB SNR. Panel (c) illustrates the close return map of the noise reduced signal. As before, an embedding dimension of 15 was used in the algorithm but, only 10 nearest neighbors. Three iterations of the algorithm were used to produce the results shown in panel (c).

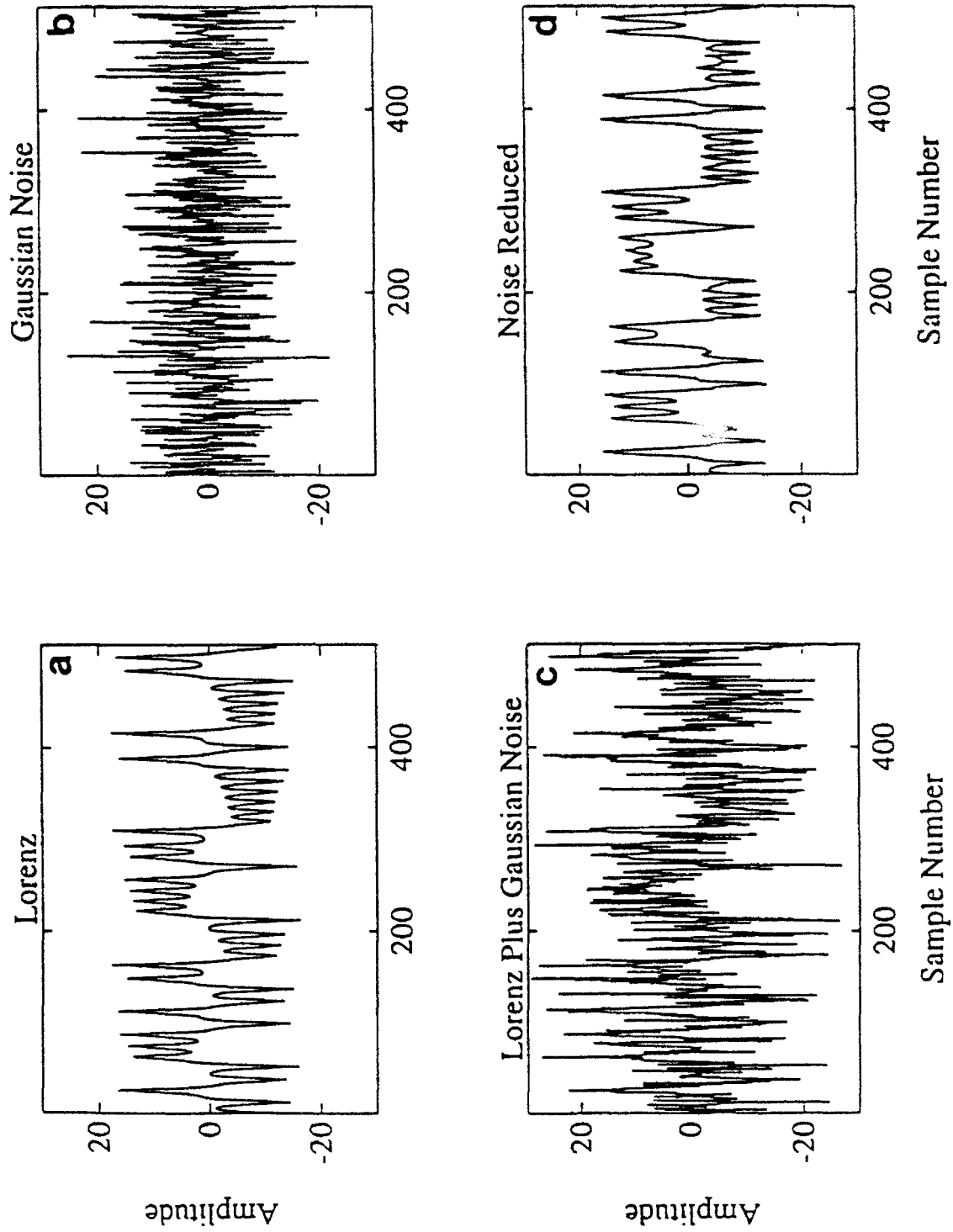


Figure 4-1. Noise Reduction Time Series: (a) Time Series of Lorenz Waveform; (b) Gaussian Noise; (c) Signal Plus Noise; and (d) Noise-Reduced Signal.

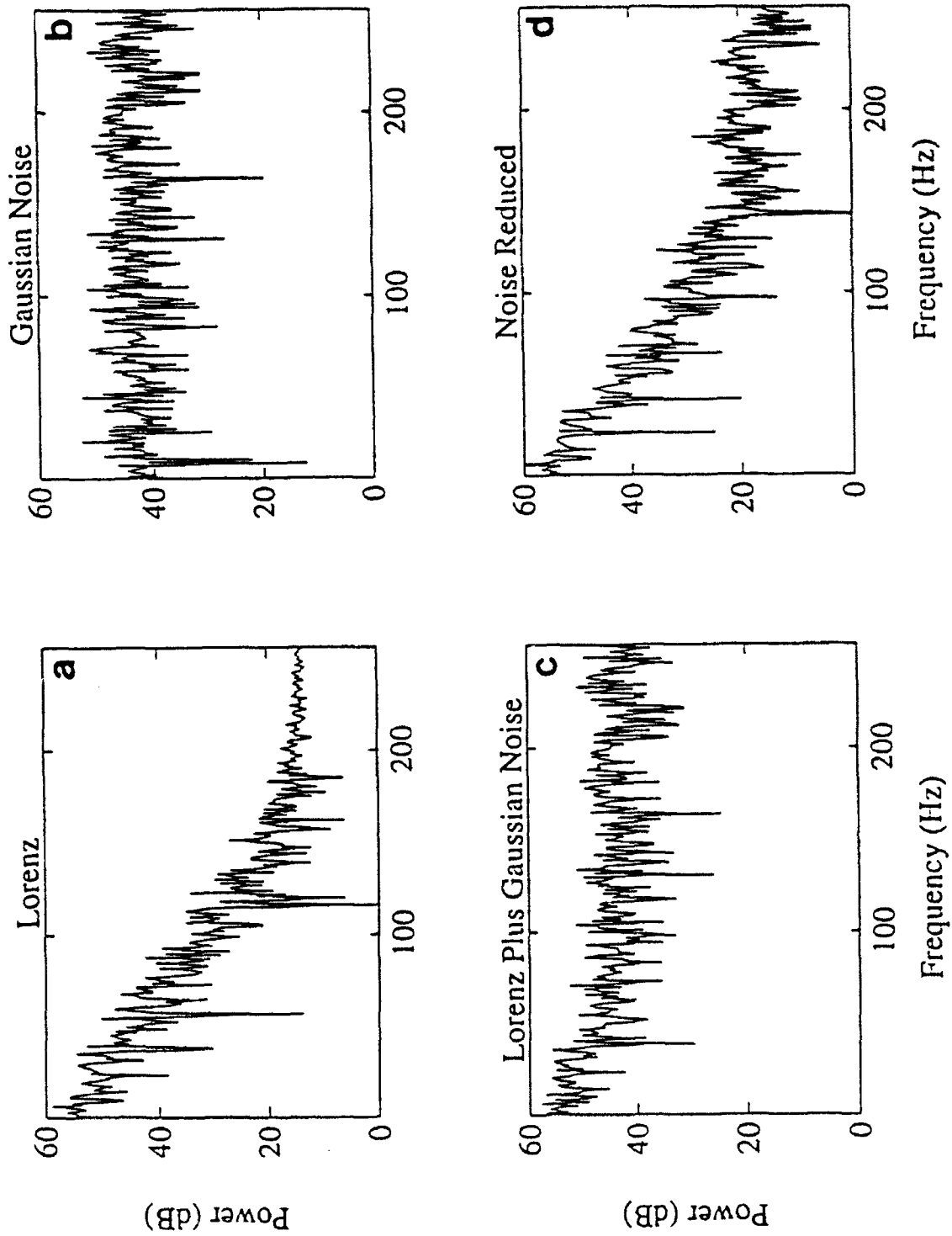


Figure 4-2. Noise Reduction Power Spectra: (a) Power Spectrum of Lorenz Waveform; (b) Gaussian Noise; (c) Signal Plus Noise; and (d) Noise-Reduced Signal.

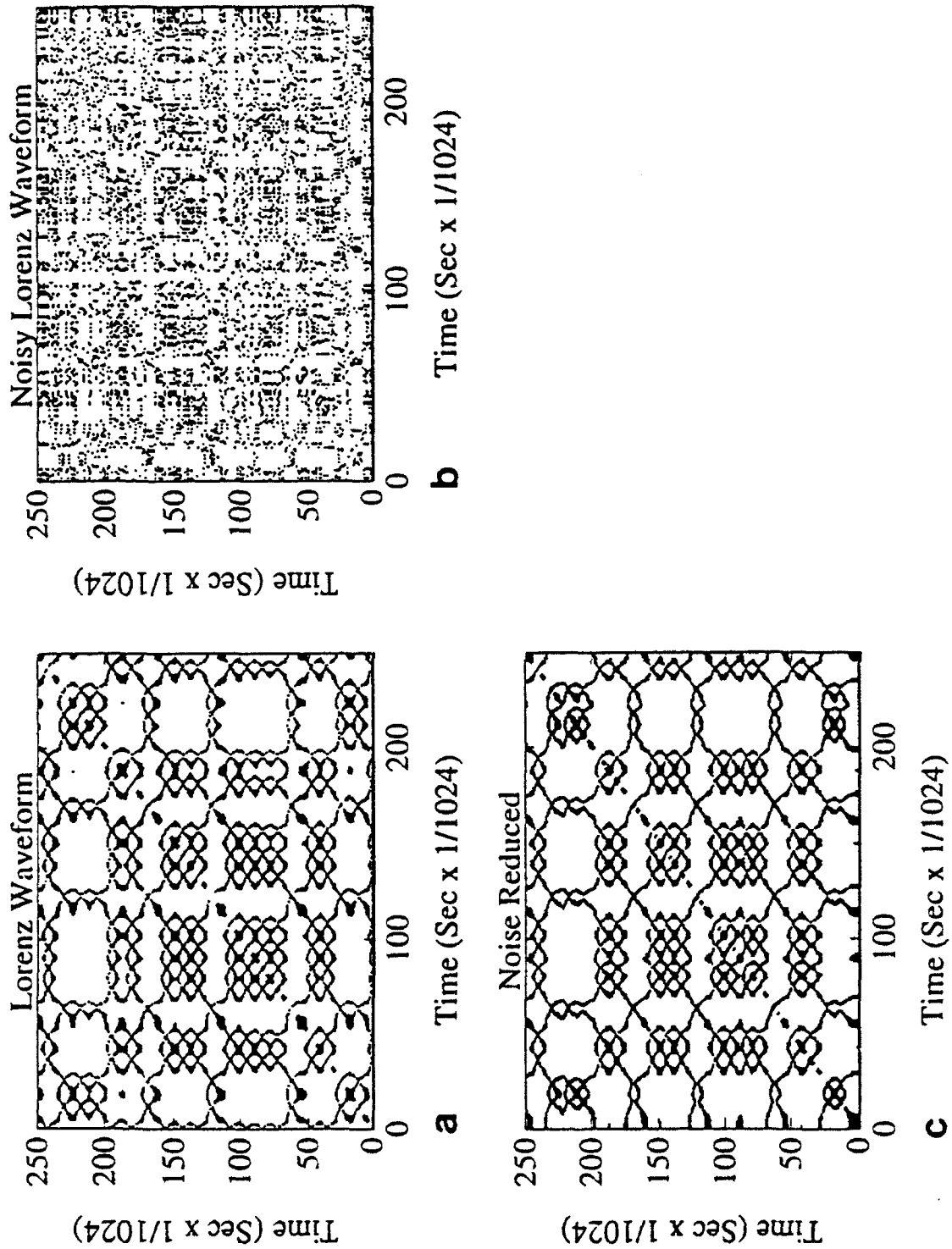


Figure 4-3. Close Return Maps of the Lorenz Waveform: (a) SNR Infinite; (b) in Gaussian Noise at 0 dB SNR; (c) After Noise Reduction.

5. CONCLUSIONS

As broadband signals, chaotic waveforms have desirable characteristics such as range resolution, range-rate resolution (Doppler), and reverberation discrimination against moving targets. Second, unlike pseudo-random noise, chaotic waveforms are amenable to noise reduction techniques that enhance the Signal-to-Noise Ratio (SNR) because they are of low dimensionality. Additionally, because chaotic signals are difficult to recognize, they decrease the potential for recognition by opposition forces.

Using a selection of qualitative and quantitative metrics, the Lorenz waveform is identified as suitable for use in active surveillance scenarios. Further, it is demonstrated that, given present projector technology constraints, waveform generation can be accomplished using straightforward band-shifting techniques.

REFERENCES

- Brindley, J., Kapitaniak, T. & El Naschie, M.S. (1991). Analytical conditions for strange chaotic and nonchaotic attractors of the quasiperiodically forced van der Pol equation. *Physica D*, 51, 28-38.
- Broomhead, D.S. & King, G.P. (1986). Extracting qualitative dynamics from experimental data. *Physica D*, 20, 217-36.
- Cawley, R. & Hsu, G.-H. (1992). SNR performance of a noise reduction algorithm applied to coarsely sampled chaotic data. *Phys. Lett. A*, 166, 188-96.
- Duffing, G. (1918). *Erzwungene Schwingungen bei Veränderlicher Eigenfrequenz*. Vieweg: Braunschweig.
- Gouesbet, G. & Maquet, J. (1992). Construction of phenomenological models from numerical scalar time series. *Physica D*, 58, 202-15.
- Grassberger, P. & Procaccia, I. (1983). Measuring the strangeness of strange attractors. *Physica D*, 9, 189-208.
- Henon, M. (1982). A two-dimensional map with a strange attractor. *Commun. Math. Phys.*, 50, 69-82.
- Lauwerier, H.A. (1986). One-dimensional iterative maps. In *Chaos*, A.V. Holden, ed., Princeton University Press.
- Lorenz, E.N. (1963). Deterministic non-periodic flow. *J. Atmos. Sci.*, 20, 130-41.

Lorenz, E.N. (1989). Computational Chaos - A prelude to computational instability *Physica D*, **35**, 299-317.

Millonas, M.M. & Reichl, L.E. (1992). Stochastic chaos in a class of Fokker-Planck equations. *Phys. Rev. Lett.*, **68**, 3125-8.

Provenzale, A., Smith, L.A., Vio, R. & Murante, G. (1992). Distinguishing between low-dimensional dynamics and randomness in measured time series. *Physica D*, **58**, 31-49.

Ueda, Y. (1979). Randomly transitional phenomena in the system governed by Duffing's equation. *J. Stat. Phys.*, **20**, 181-96.

Wolf, A. (1986). Quantifying chaos with Lyapunov exponents. In *Chaos*, A. V. Holden, ed., Princeton Univ. Press.

APPENDIX A NONLINEAR EQUATIONS

A.1 Quasiperiodically forced van der Pol equation:

$$\ddot{x} - 2\lambda(1 - \beta x^2)\dot{x} + \omega_0^2 x = F \cos(\Omega t)$$

where: $\lambda < 1$
 $\omega < \Omega$
 $\omega < 1$

Brindley et al. (1991)

A.2 Rössler equation:

$$\dot{x} = -y - z$$

$$\dot{y} = x + ay$$

$$\dot{z} = b + z(x - c)$$

where: $a = 0.146$
 $b = 0.2$
 $c = 10$

Gouesbet & Maquet (1992)

A.3 Nonlinear stochastic equation:

$$\dot{y} = (\alpha - 0.5) \beta - y + \sqrt{2 \beta y} w$$

where: w = standard Gaussian white noise process

$$\alpha = 1$$

$$\beta = 1$$

Provenzale et al. (1992)

A.4 Fokker Equation

$$\dot{\phi} = 2x^4 + 0.6y^4 + \epsilon xy(x - y)^2$$

where: $\epsilon = 0.004$

Millonas & Reichl (1992)

APPENDIX B

PROPAGATION CHANNEL

Figures B-1 through B-6 illustrate the impulse and frequency responses of the six ocean environments utilized in this work. The frequency responses were provided by NUWC in New London, Connecticut and are for the transmitter-target and target-receiver geometries given in Table 3.1-1 in the body of this report.

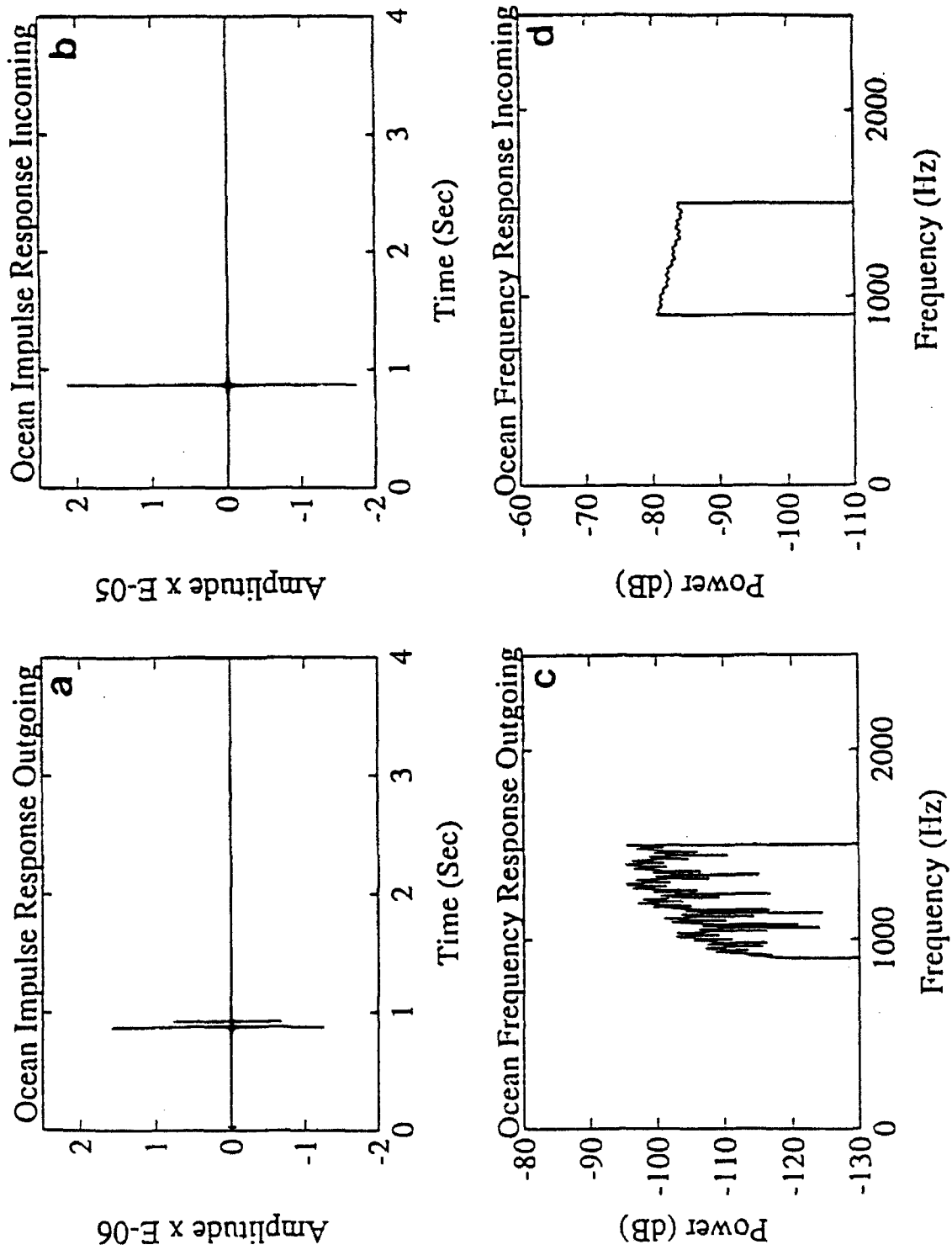


Figure B-1. Ocean Impulse and Frequency Responses for Outgoing and Incoming Channels for Case 1.

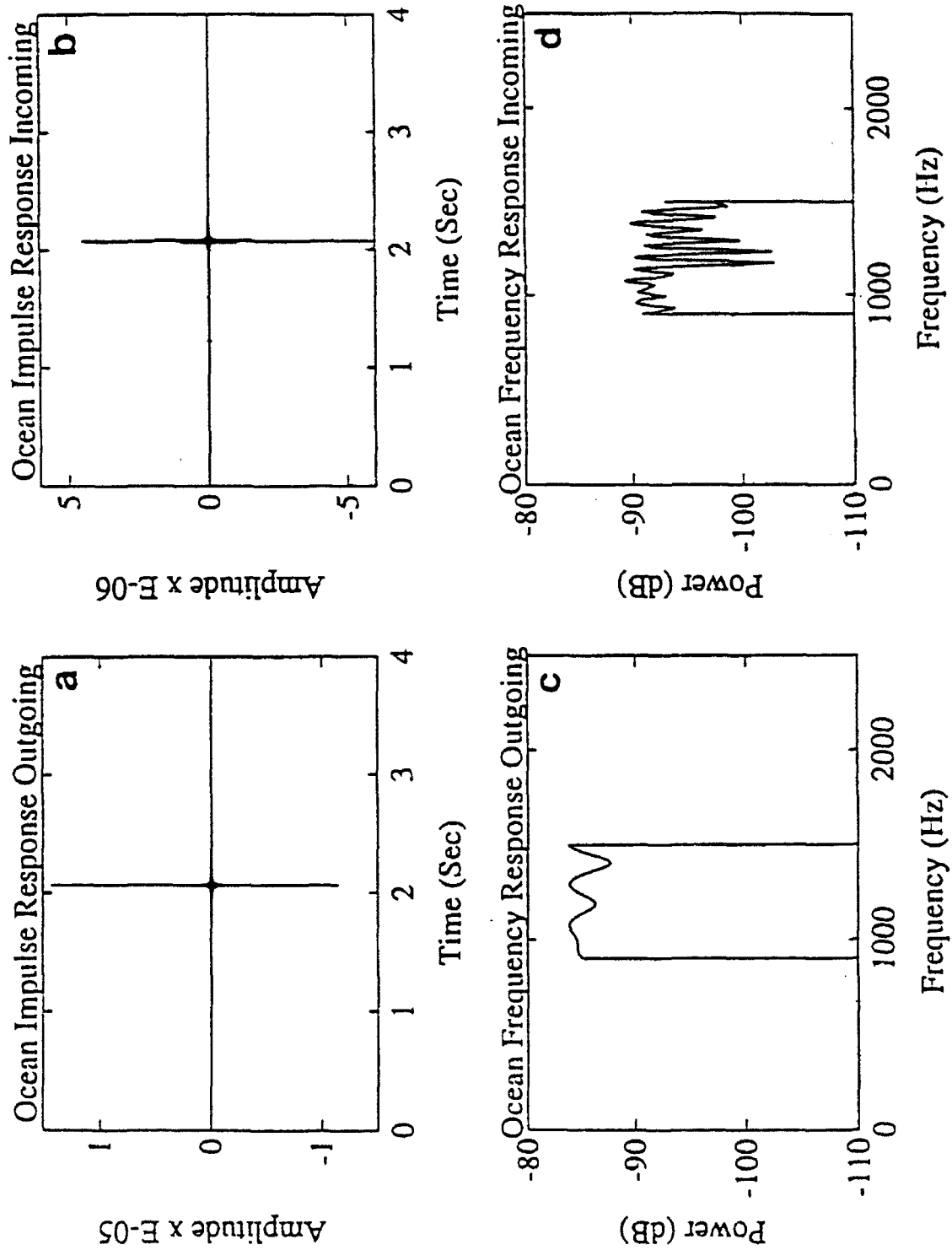


Figure B-2. Ocean Impulse and Frequency Responses for Outgoing and Incoming Channels for Case 2.

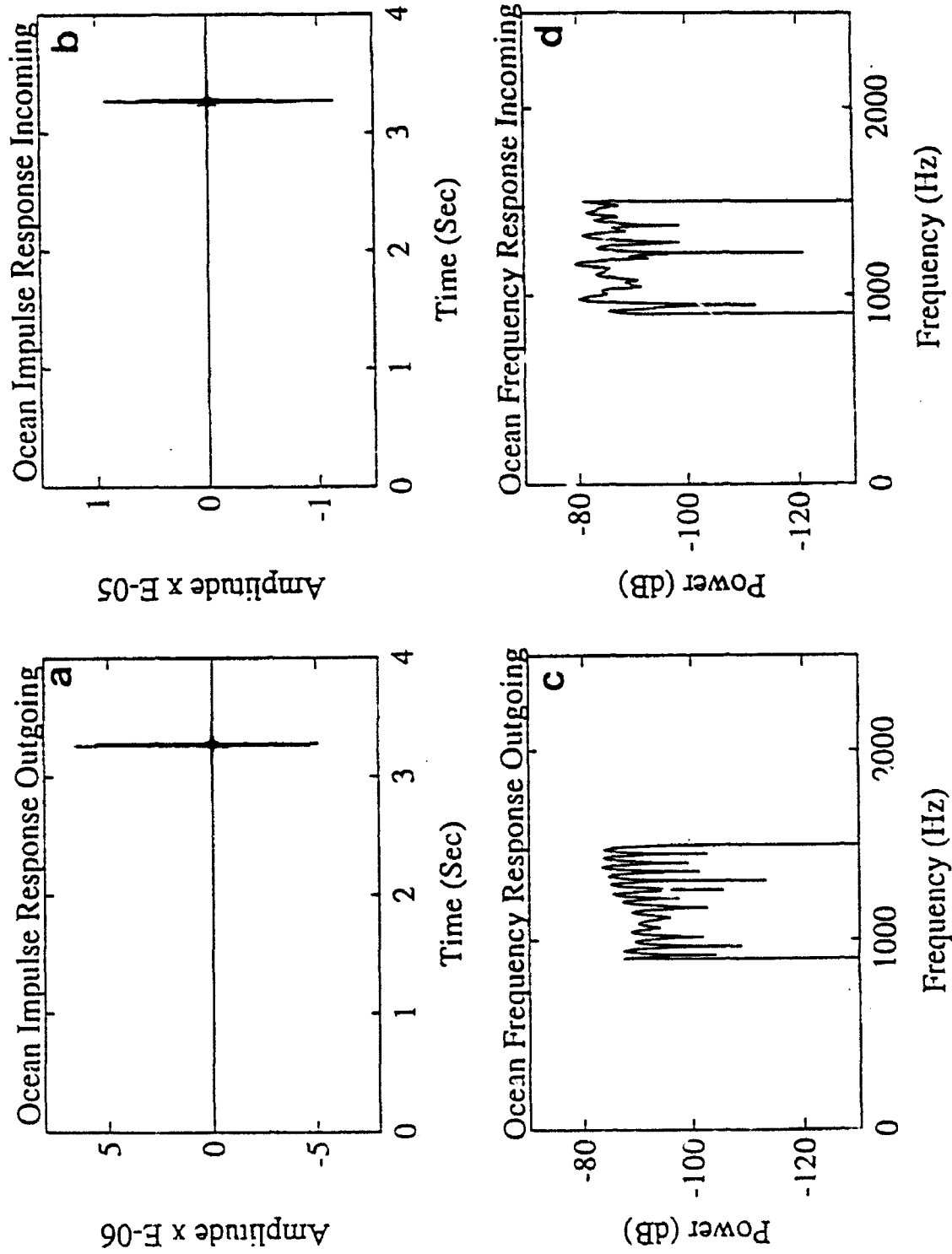


Figure B-3. Ocean Impulse and Frequency Responses for Outgoing and Incoming Channels for Case 3.

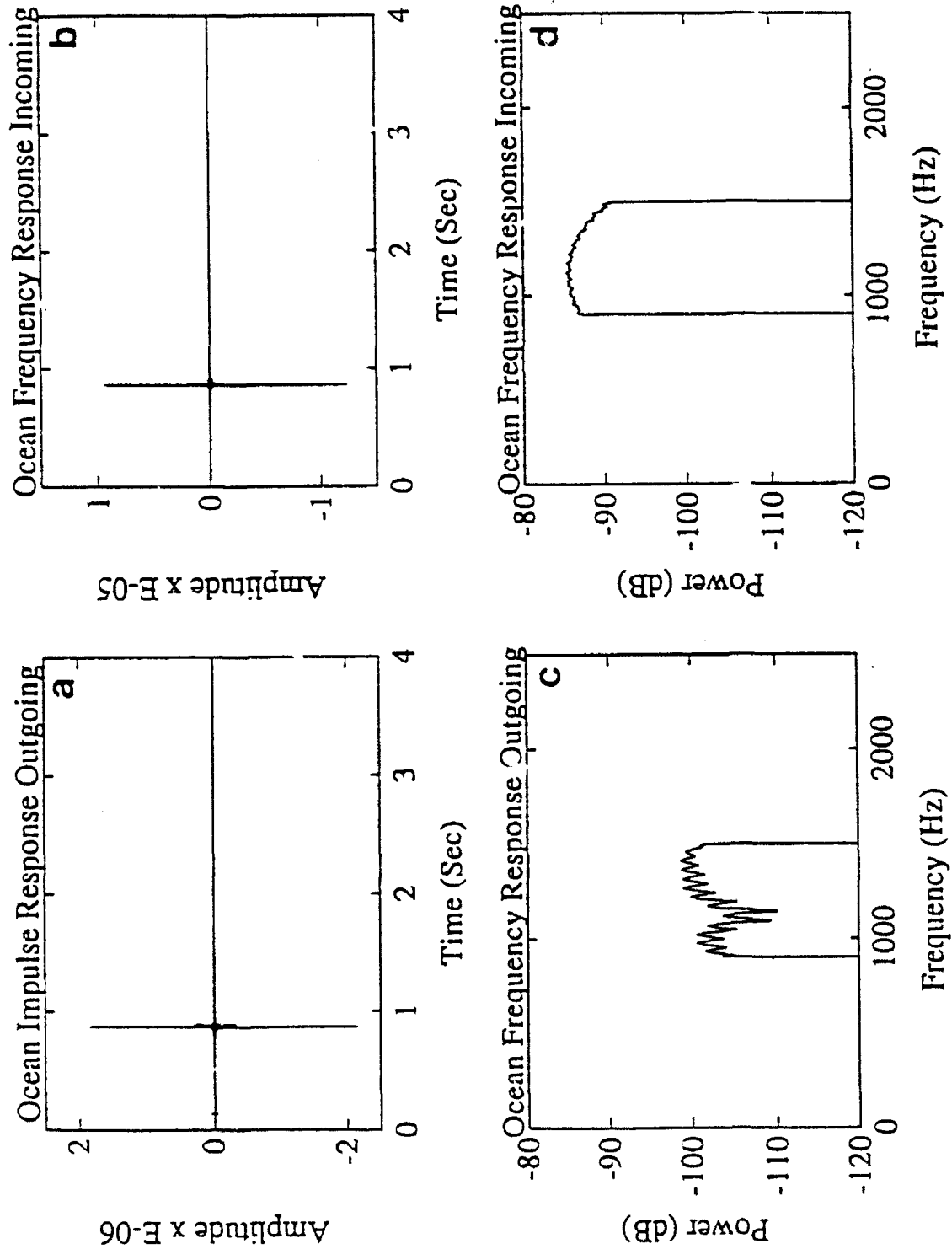


Figure B-4. Ocean Impulse and Frequency Responses for Outgoing and Incoming Channels for Case 4.

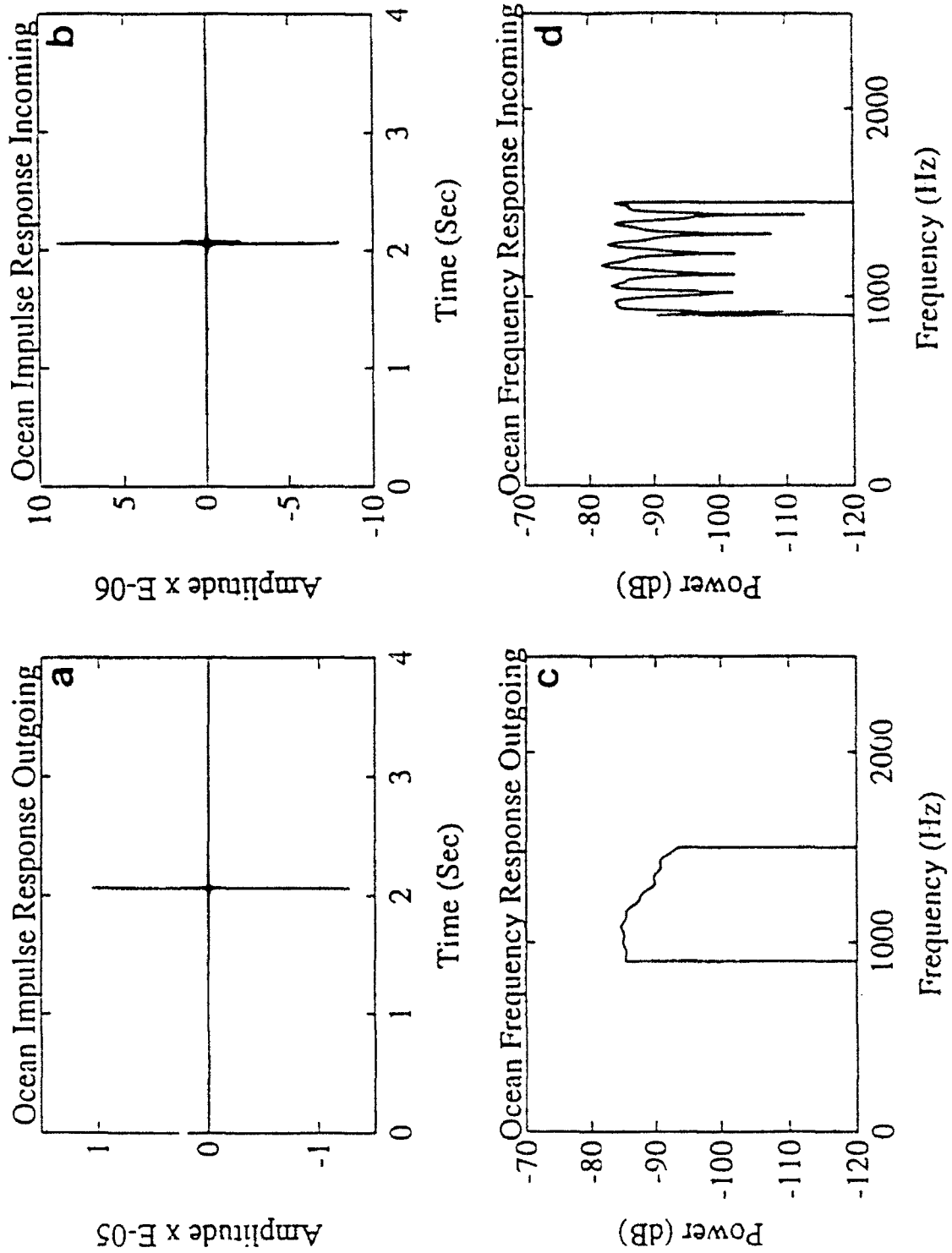


Figure B-5. Ocean Impulse and Frequency Responses for Outgoing and Incoming Channels for Case 5.

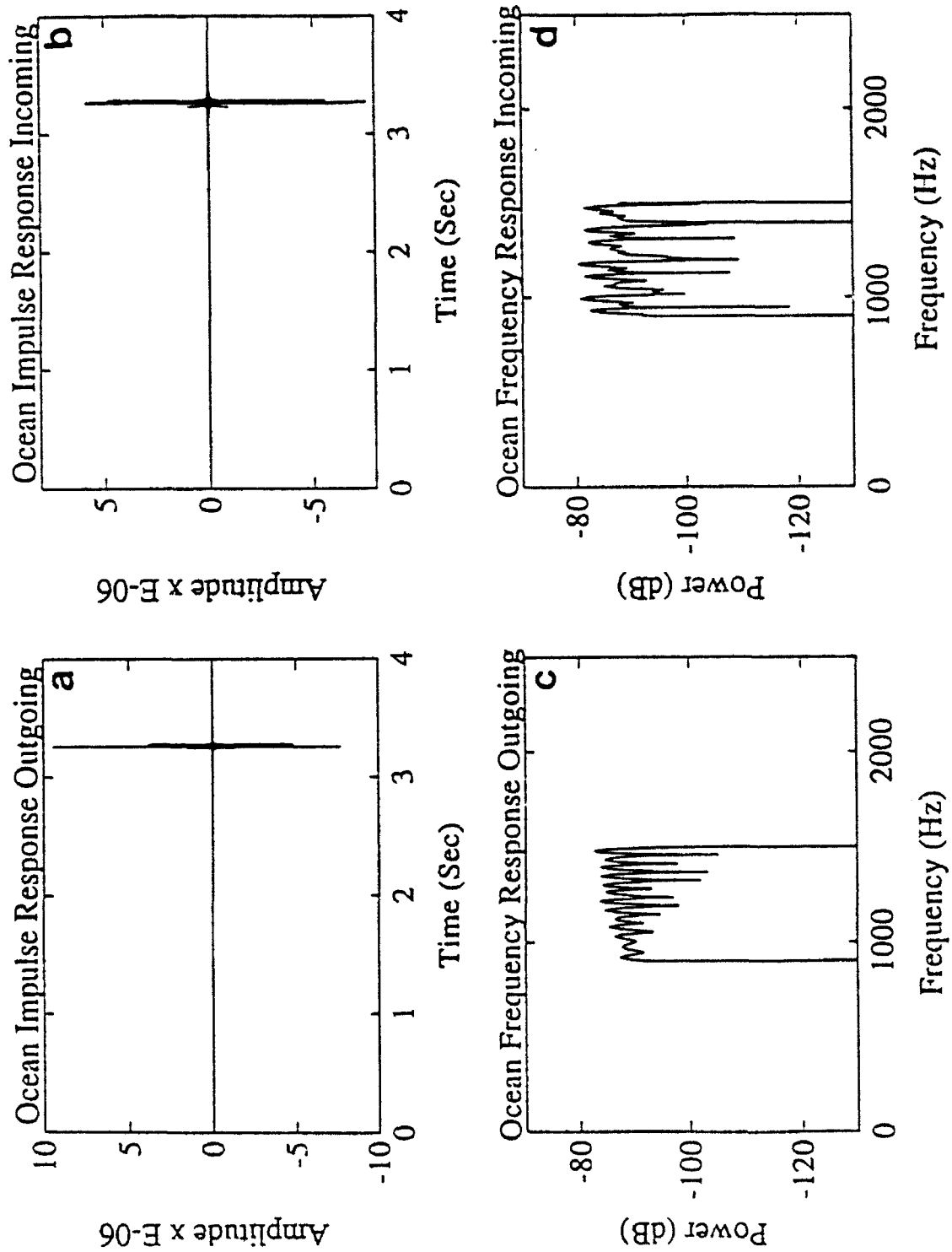


Figure B-6. Ocean Impulse and Frequency Responses for Outgoing and Incoming Channels for Case 6.

APPENDIX C

REPLICA CORRELATIONS WITH NOISY SIGNALS

Figures C-1 through C-8 present cross correlations of the Lorenz, Duffing, Henon, and Iterative waveforms with noisy copies of the same. For each waveform there are two figures each containing four panels. The panels of the first figure of each set of two are correlation with noisy signals with SNRs of 20, 10, 0, and -10. The SNRs of the second figure of each set are -15, -20, -25, and -30. Note the scale change between the first figure of each set (0 to 1) and the second figure (0 to 0.2).

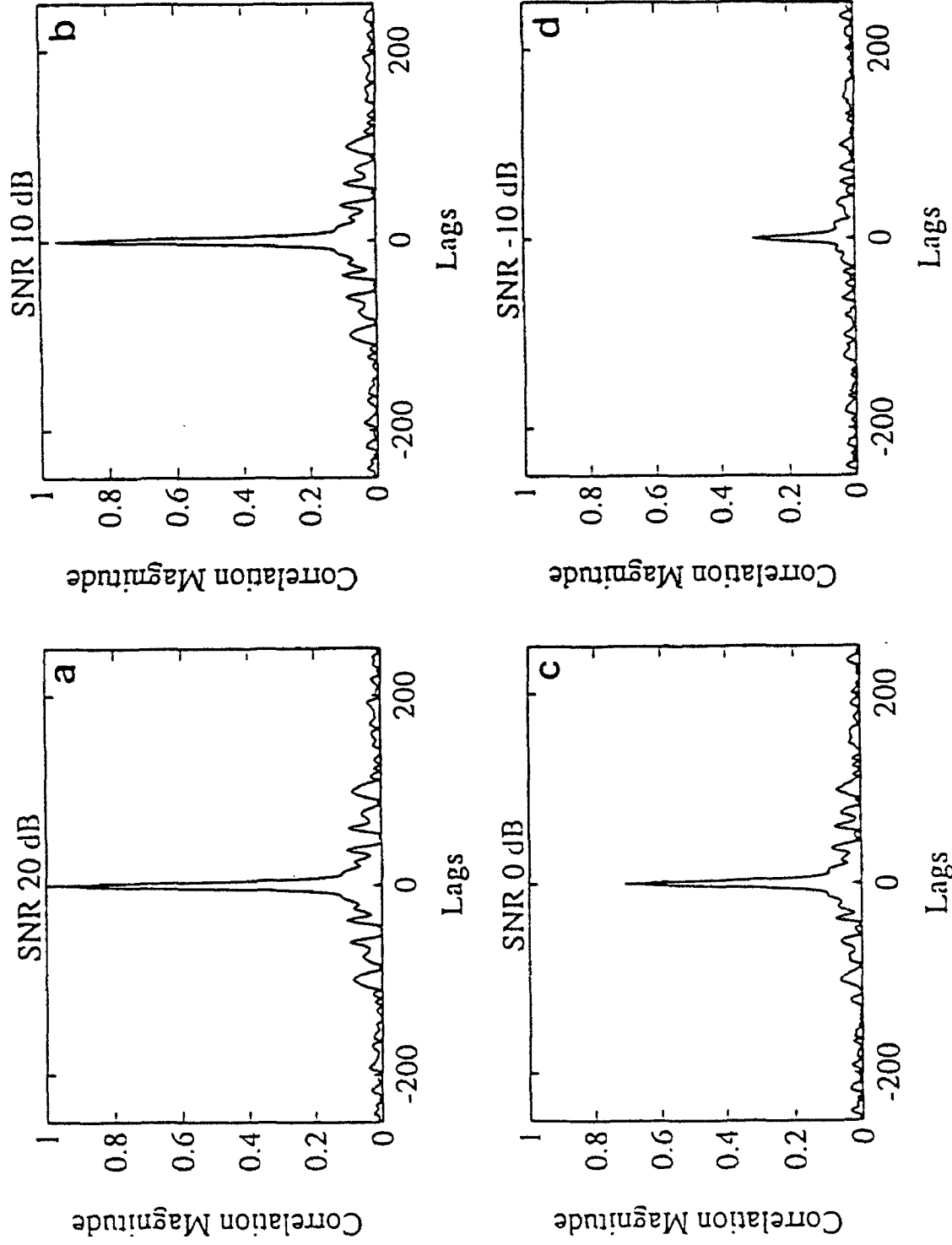


Figure C-1. Replica Correlations for Noise-Contaminated Lorenz Echoes for Selected SNR Values: (a) 20 dB; (b) 10 dB; (c) 0 dB; and (d) -10 dB.

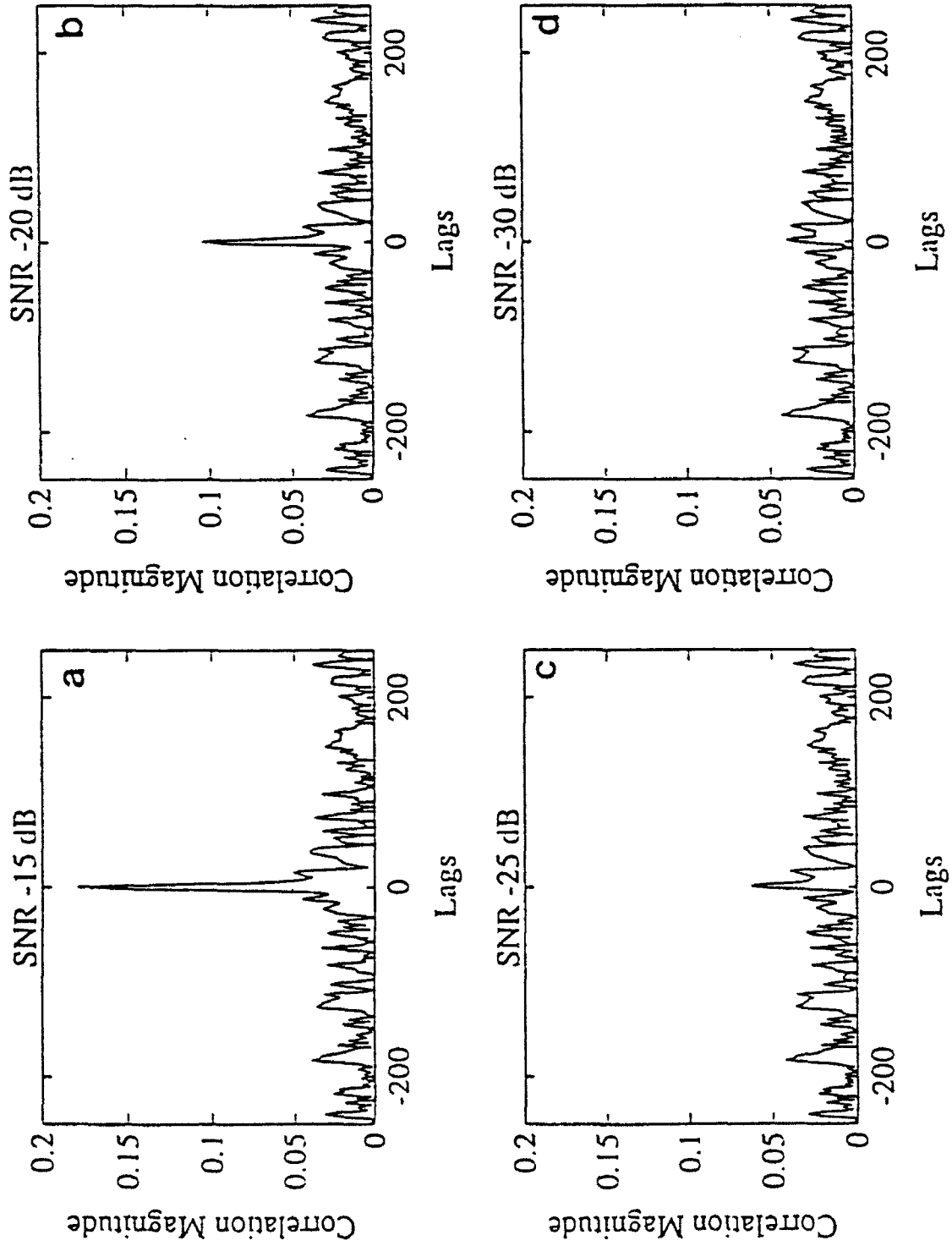


Figure C-2. Replica Correlations for Noise-Contaminated Lorenz Echoes for Selected SNR Values: (a) -15 dB; (b) -20 dB; (c) -25 dB; and (d) -30 dB..

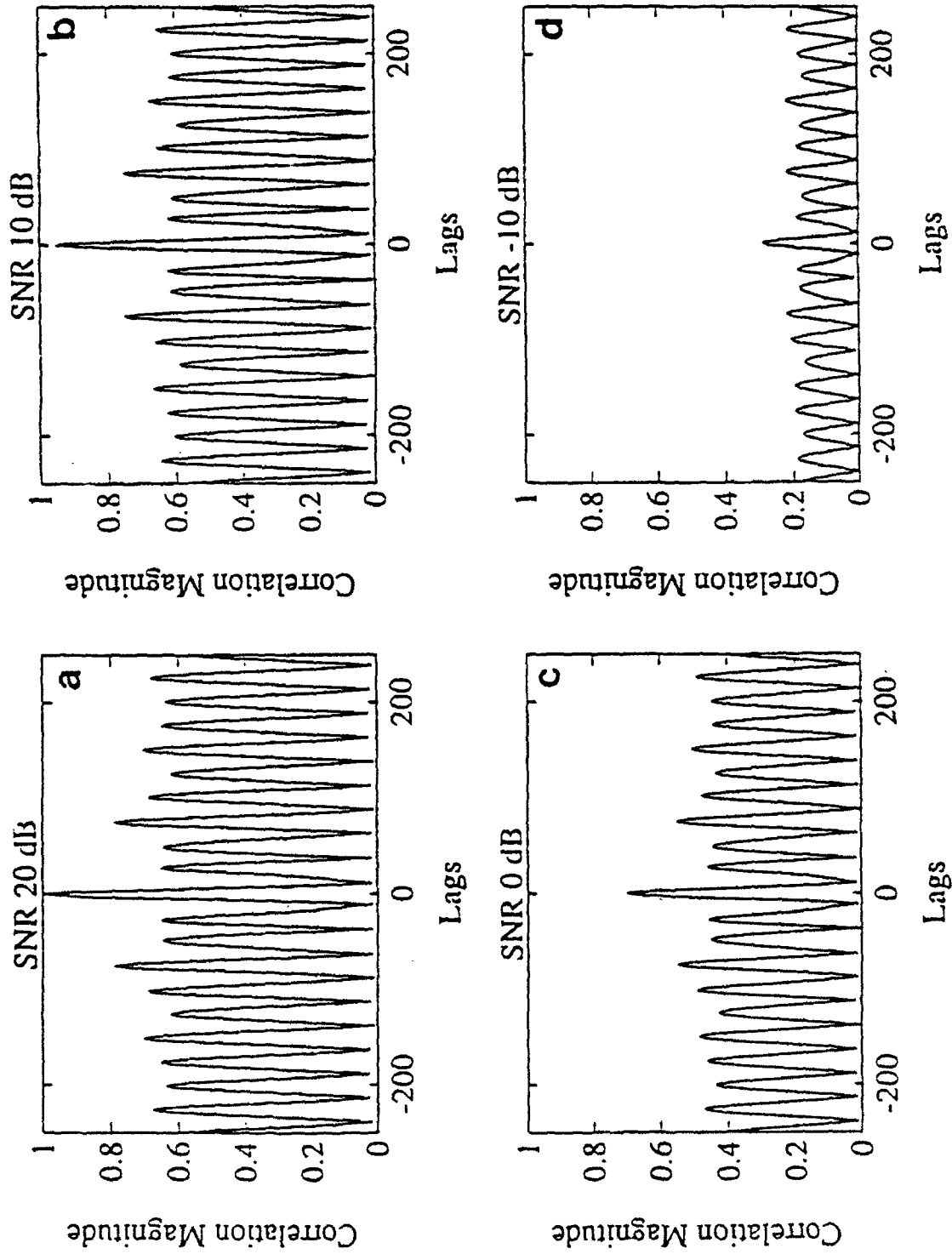


Figure C-3. Replica Correlations for Noise-Contaminated Duffing Echoes for Selected SNR Values: (a) 20 dB; (b) 10 dB; (c) 0 dB; and (d) -10 dB.

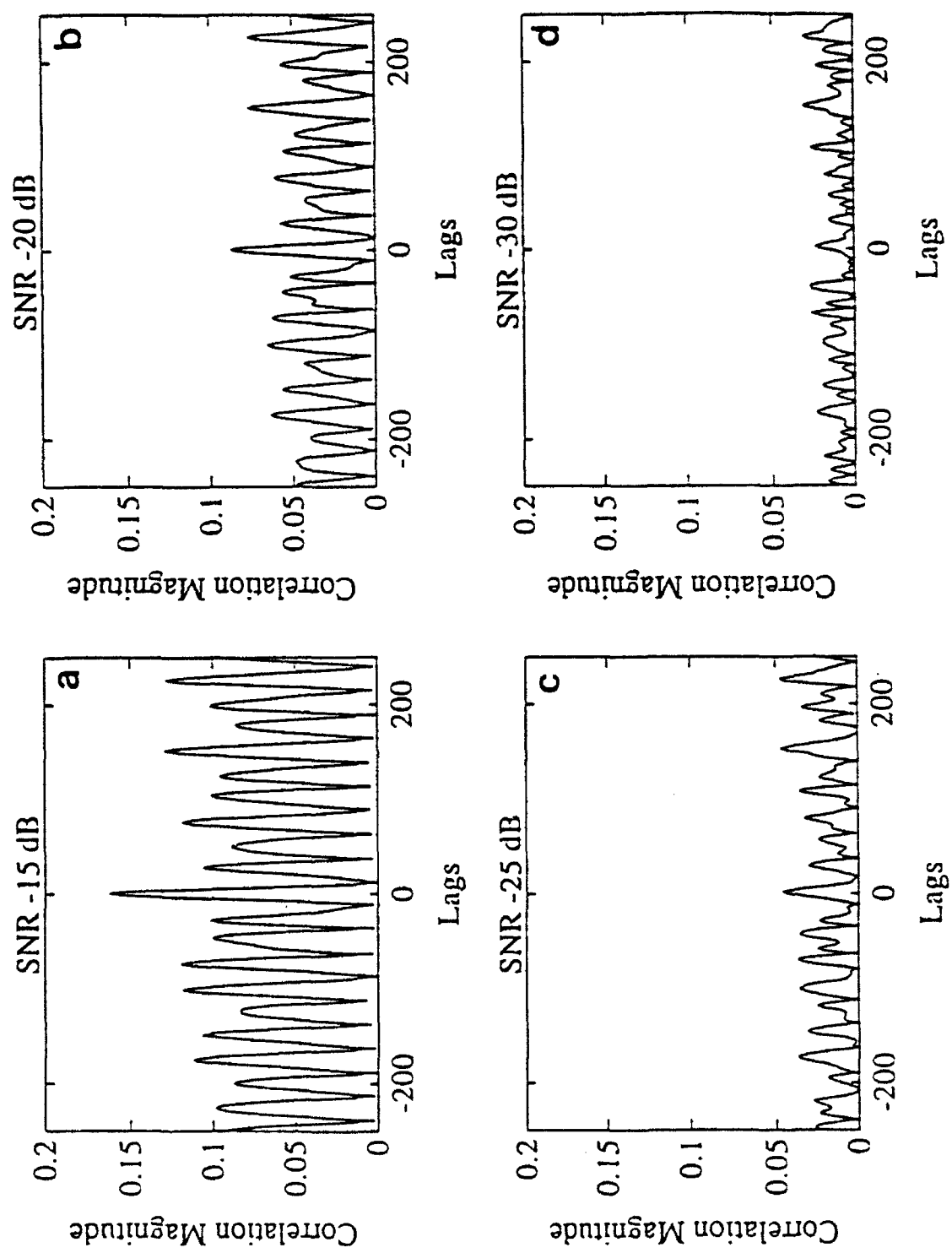


Figure C-4. Replica Correlations for Noise-Contaminated Duffing Echoes for Selected SNR Values: (a) -15 dB; (b) -20 dB; (c) -25 dB; and (d) -30 dB.

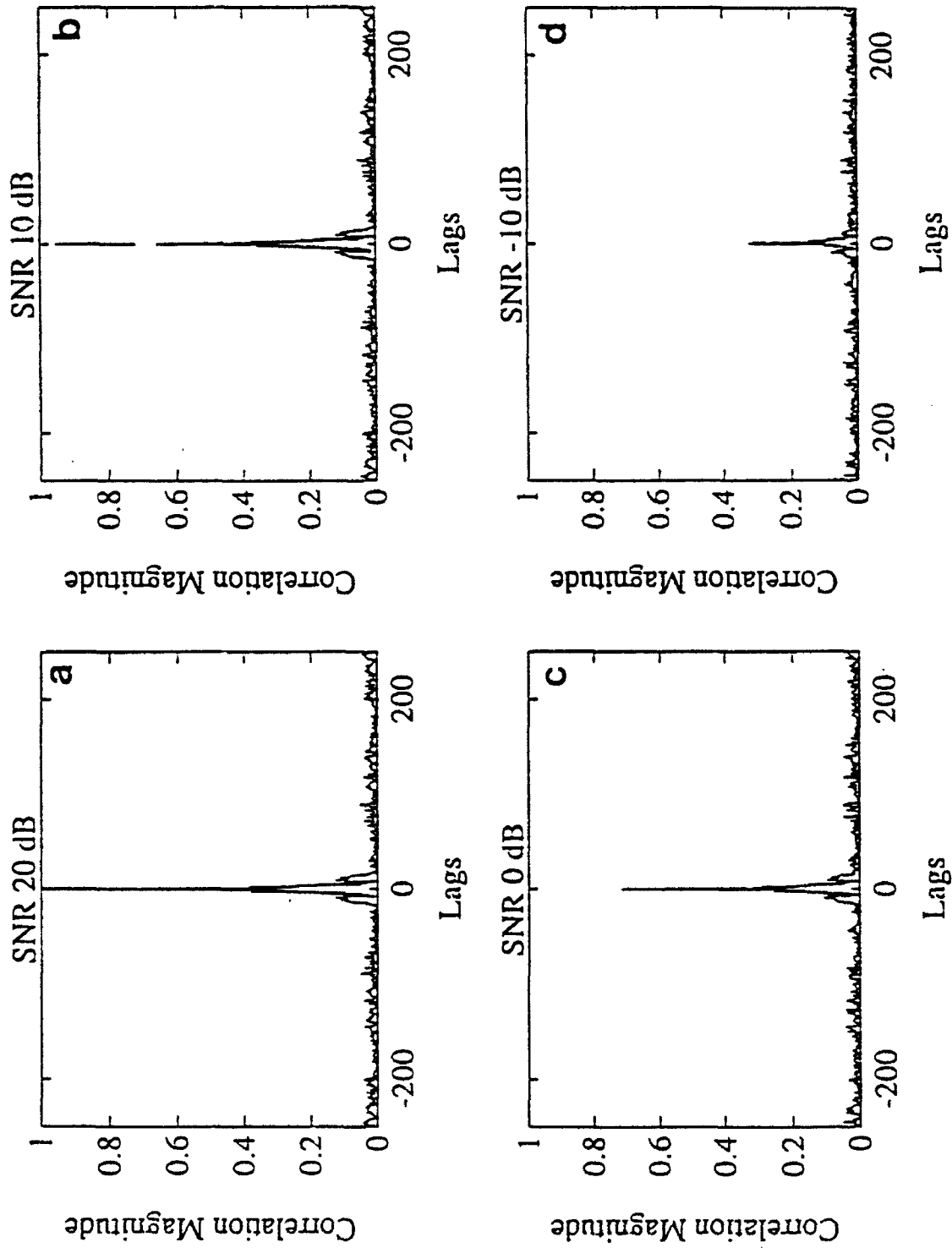


Figure C-5. Replica Correlations for Noise-Contaminated Henon Echoes for Selected SNR Values: (a) 20 dB; (b) 10 dB; (c) 0 dB; and (d) -10 dB.

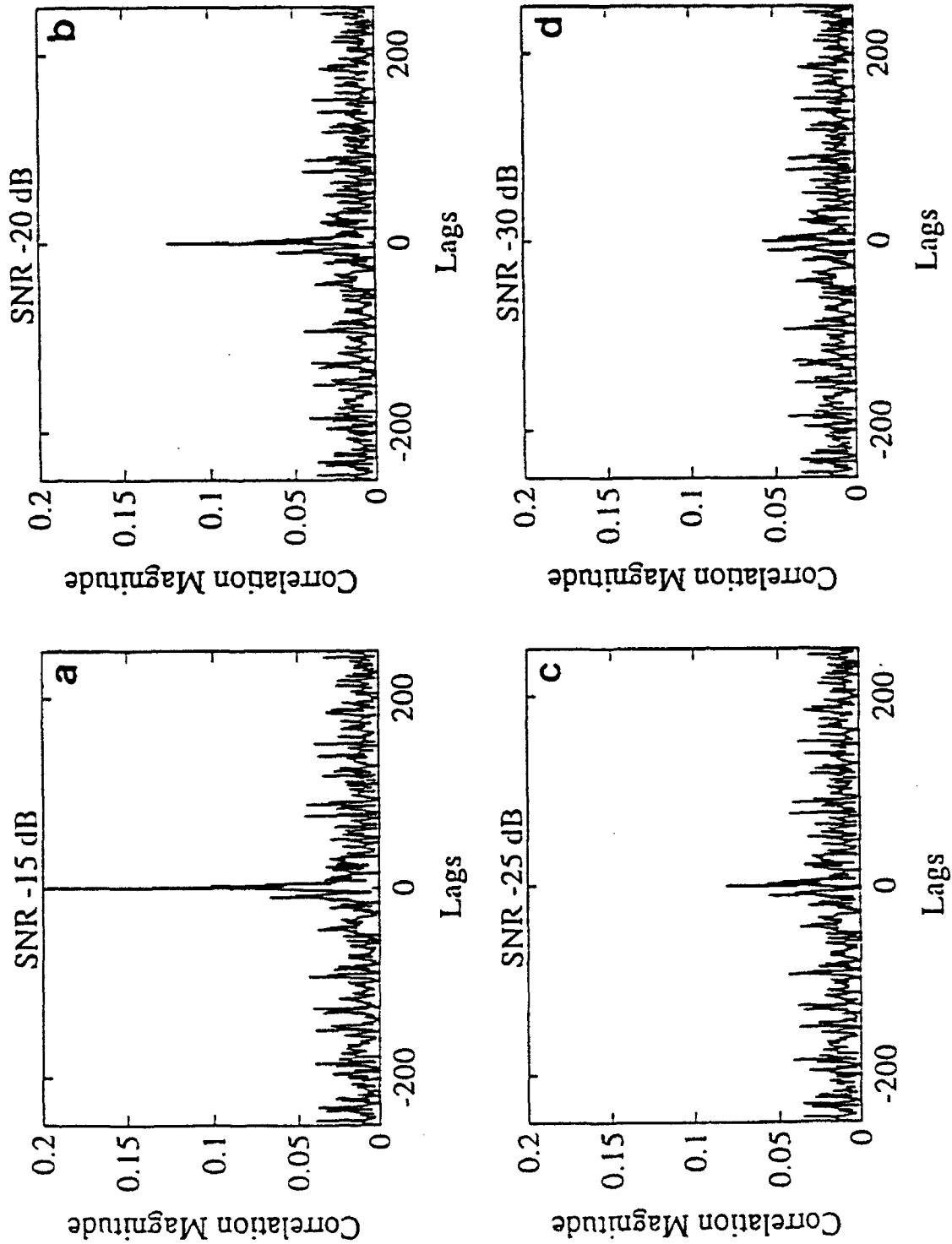


Figure C-6. Replica Correlations for Noise-Contaminated Henon Echoes for Selected SNR Values: (a) -15 dB; (b) -20 dB; (c) -25 dB; and (d) -30 dB.

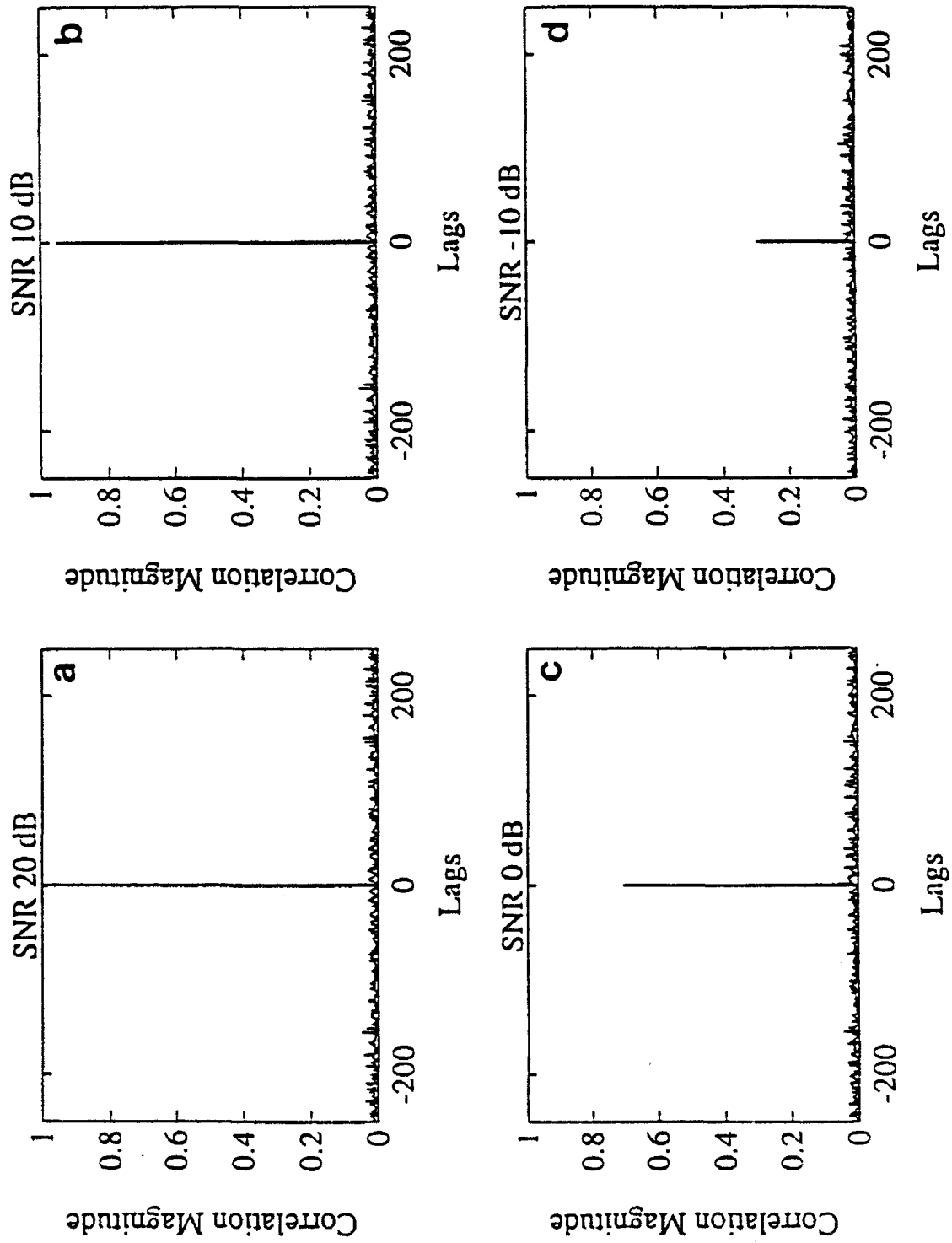


Figure C-7. Replica Correlations for Noise-Contaminated Iterative Echoes for Selected SNR Values: (a) 20 dB; (b) 10 dB; (c) 0 dB; and (d) -10 dB.

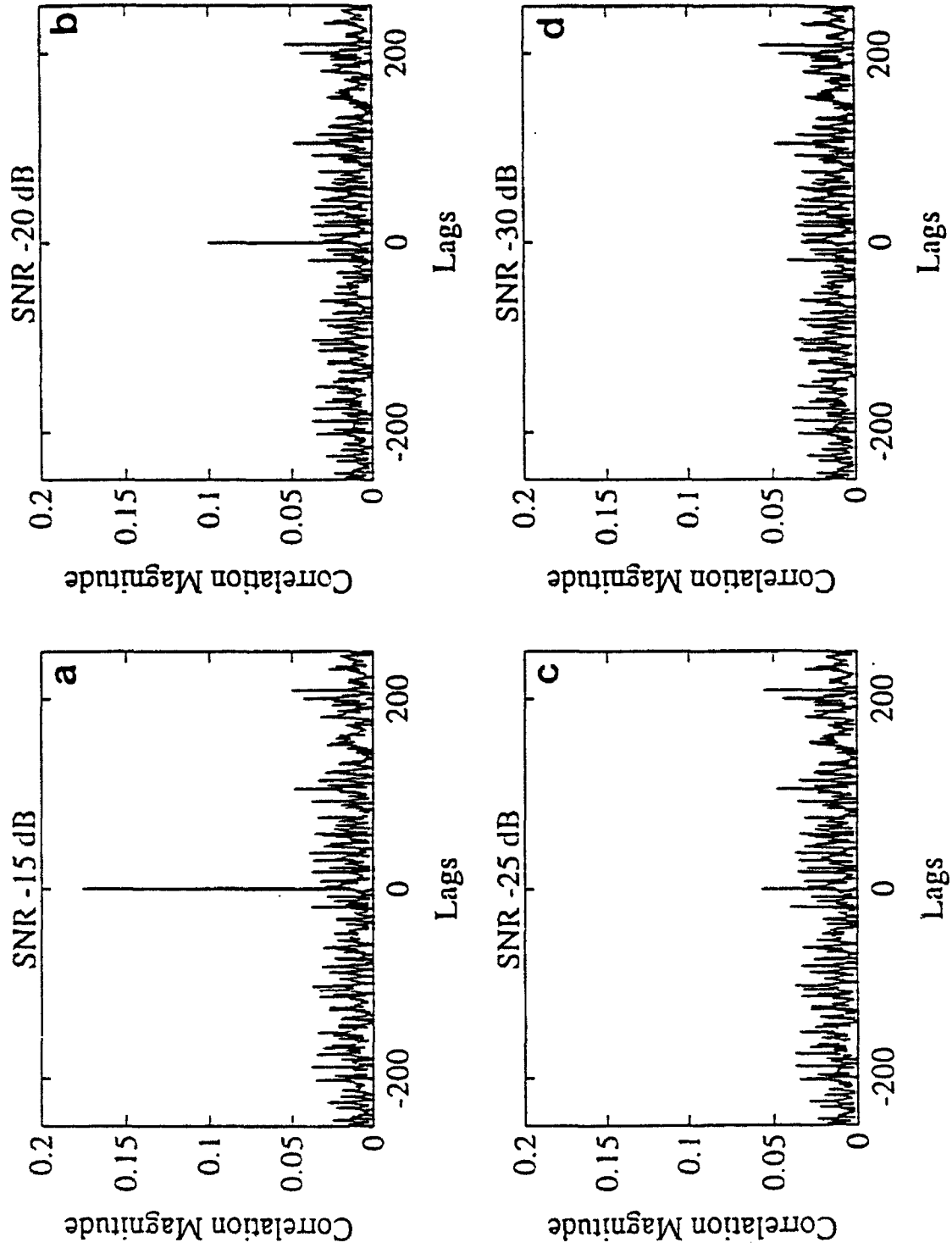


Figure C-8. Replica Correlations for Noise-Contaminated Iterative Echoes for Selected SNR Values: (a) -15 dB; (b) -20 dB; (c) -25 dB; and (d) -30 dB.

APPENDIX D

REPLICA CORRELATIONS WITH DOPPLER-SHIFTED ECHOES

Figures D-1 through D-6 present replica correlations of the Lorenz waveform with its Doppler-shifted (20 knots relative target motion) echo. Figures D-1 through D-6 correspond to propagation through the six ocean environments whose impulse and frequency responses are given in Appendix B. Each figure contains four panels, where the replica has been Doppler-shifted by a different amount in each panel. The replicas have been shifted by an amount corresponding to relative target motion of 19.5, 20, 20.2, and 20.4 knots in panels (a) through (d), respectively.

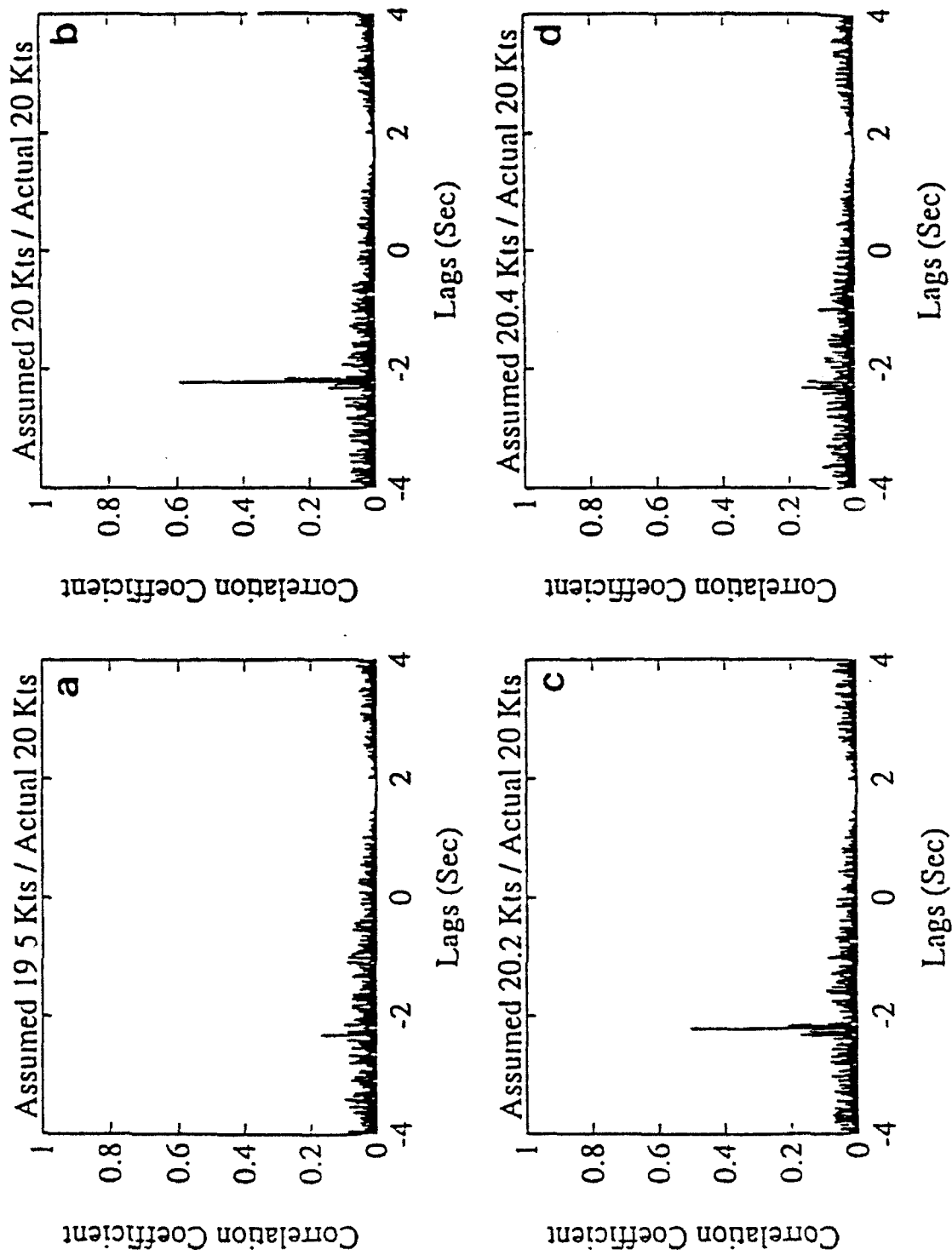


Figure D-1. Replica Correlations for Doppler-Shifted Lorenz Echoes in Case 1 with an Actual Doppler of 20 Knots and Assumed Dopplers of: (a) 19.5 Knots; (b) 20 Knots; (c) 20.2 Knots; and (d) 20.4 Knots.

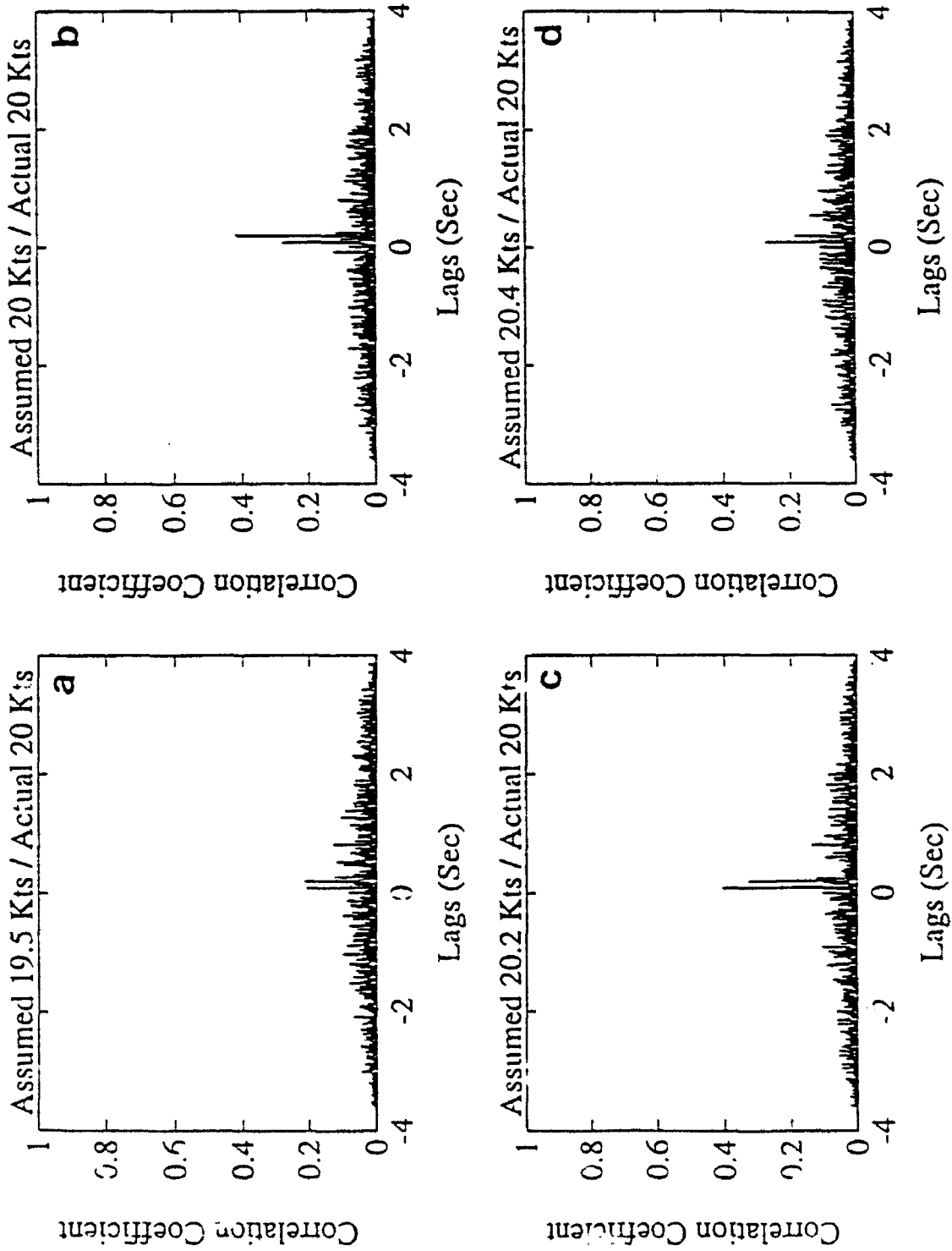


Figure D-2. Replica Correlations for Doppler-Shifted Lorenz Echoes in Case 2 with an Actual Doppler of 20 Knots and Assumed Dopplers of: (a) 19.5 Knots; (b) 20 Knots; (c) 20.2 Knots; and (d) 20.4 Knots.

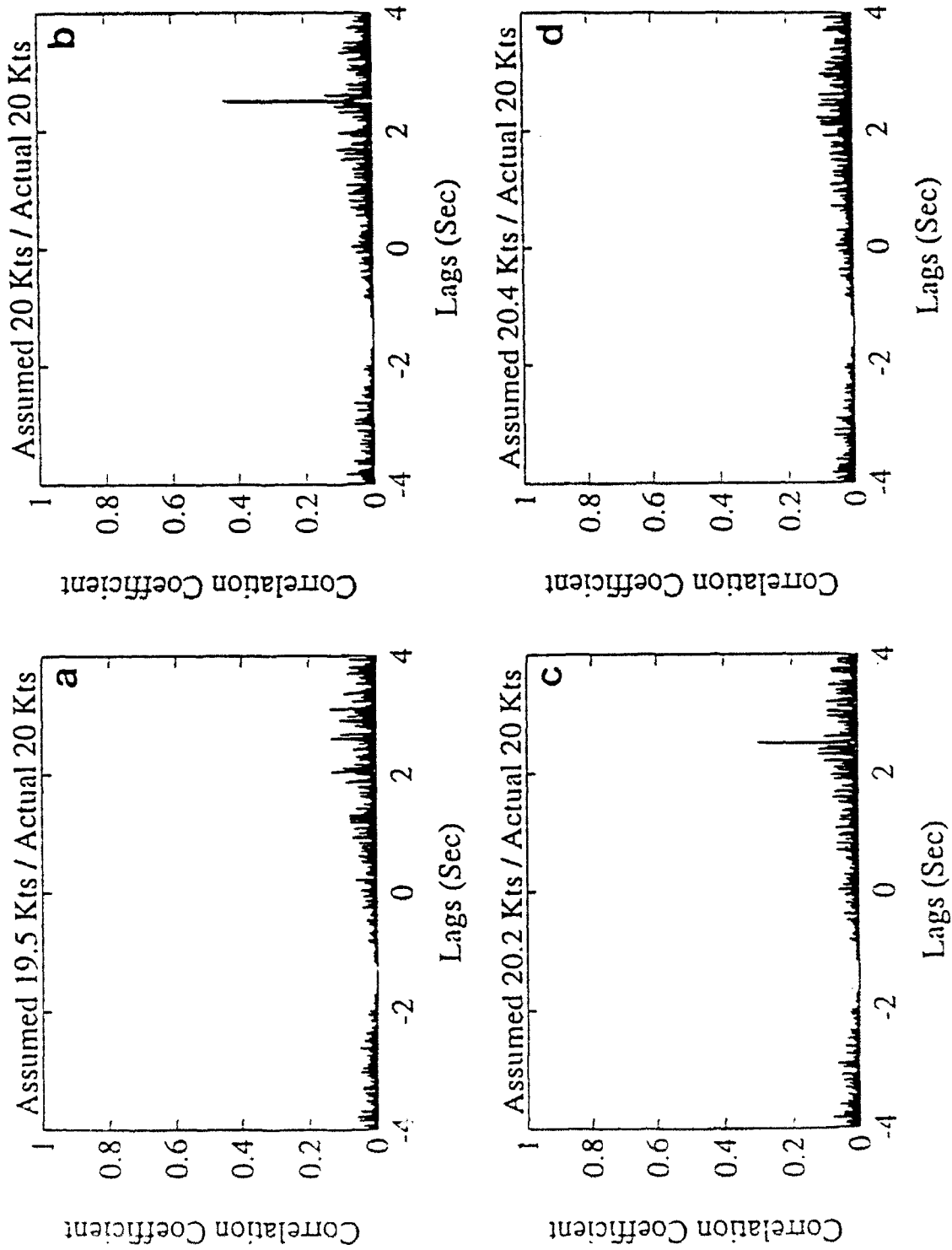


Figure D-3. Replica Correlations for Doppler-Shifted Lorenz Echoes in Case 3 with an Actual Doppler of 20 Knots and Assumed Dopplers of: (a) 19.5 Knots; (b) 20 Knots; (c) 20.2 Knots; and (d) 20.4 Knots.

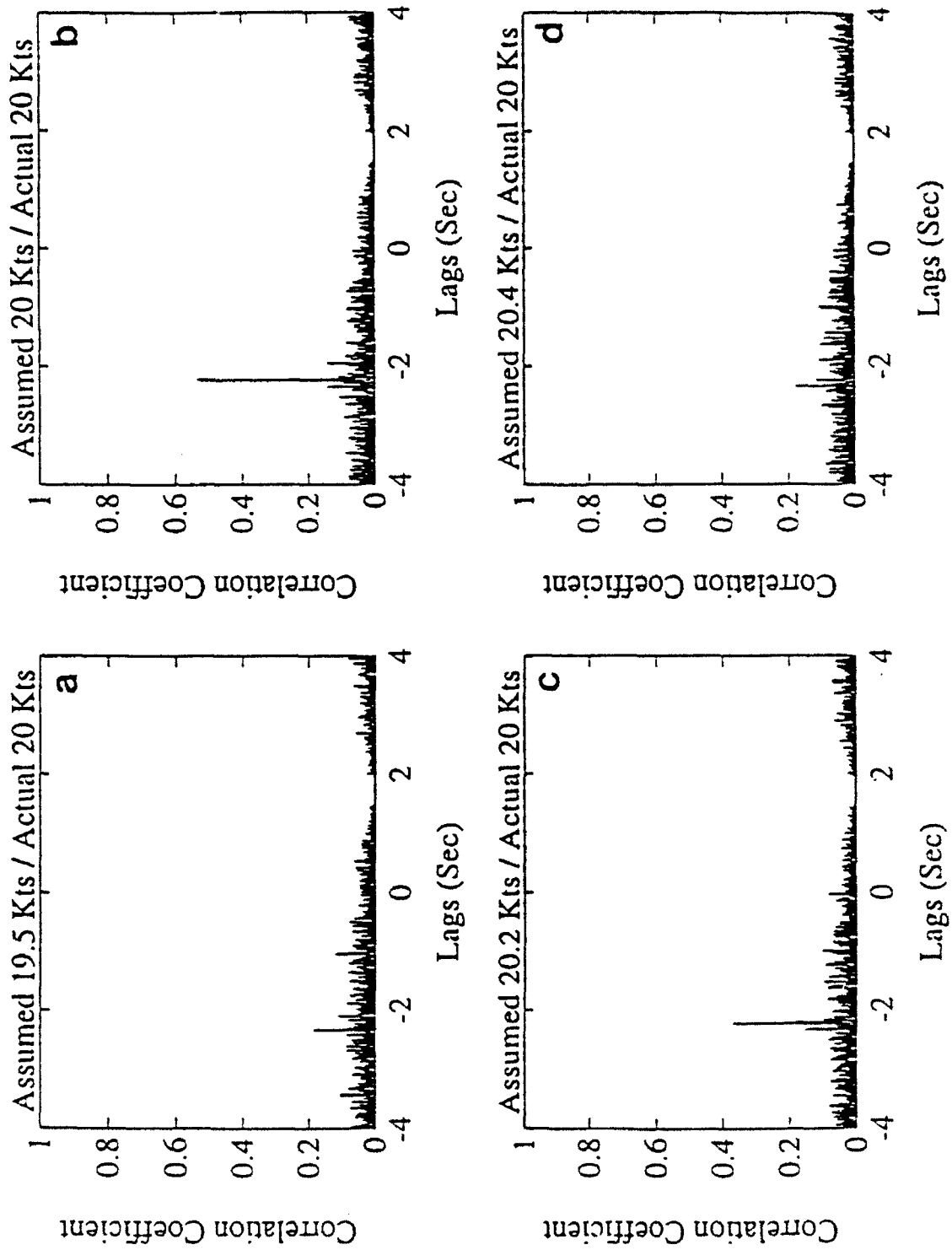


Figure D-4. Replica Correlations for Doppler-Shifted Lorenz Echoes in Case 4 with an Actual Doppler of 20 Knots and Assumed Dopplers of: (a) 19.5 Knots; (b) 20 Knots; (c) 20.2 Knots; and (d) 20.4 Knots.

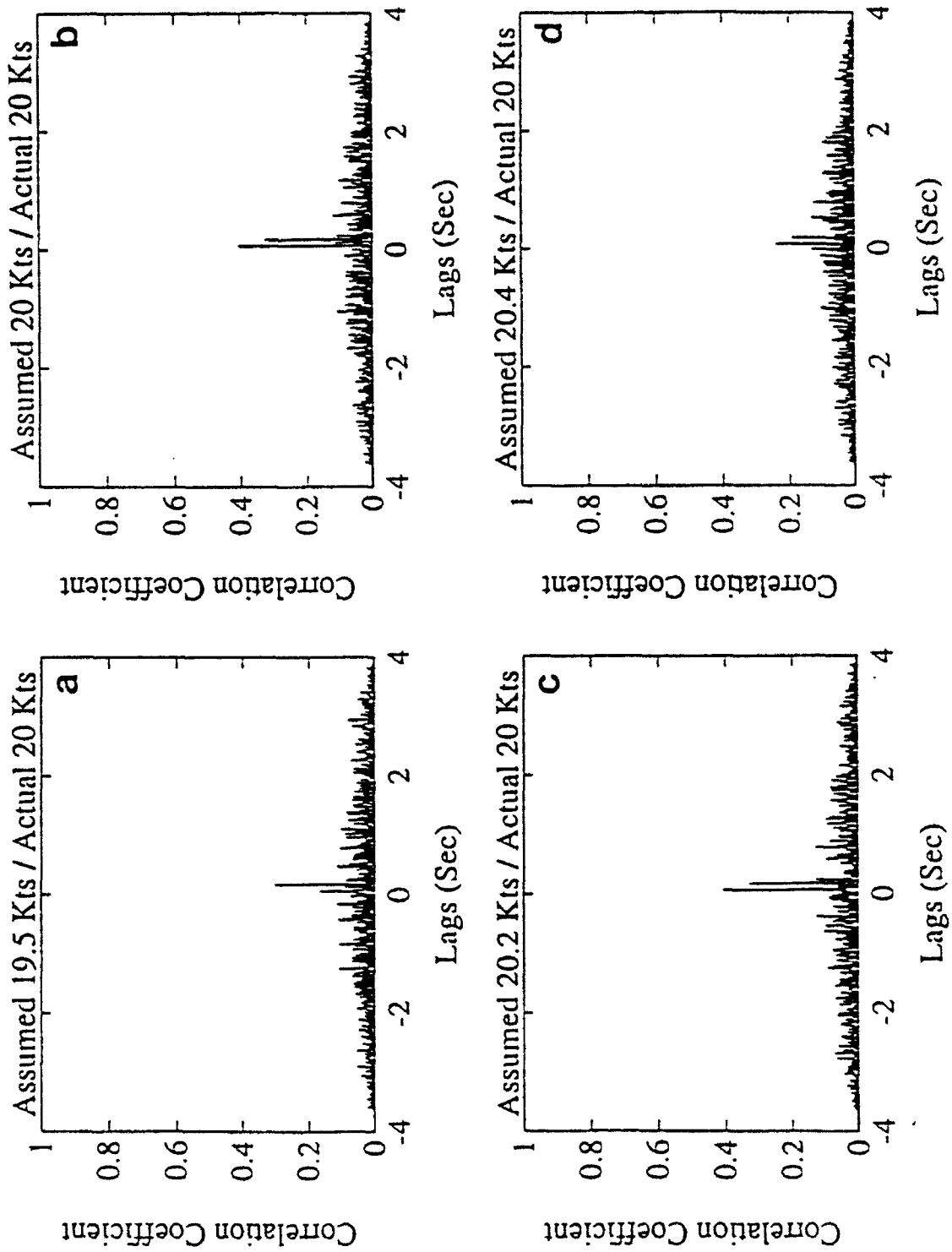


Figure D-5. Replica Correlations for Doppler-Shifted Lorenz Echoes in Case 5 with an Actual Doppler of 20 Knots and Assumed Dopplers of: (a) 19.5 Knots; (b) 20 Knots; (c) 20.2 Knots; and (d) 20.4 Knots.

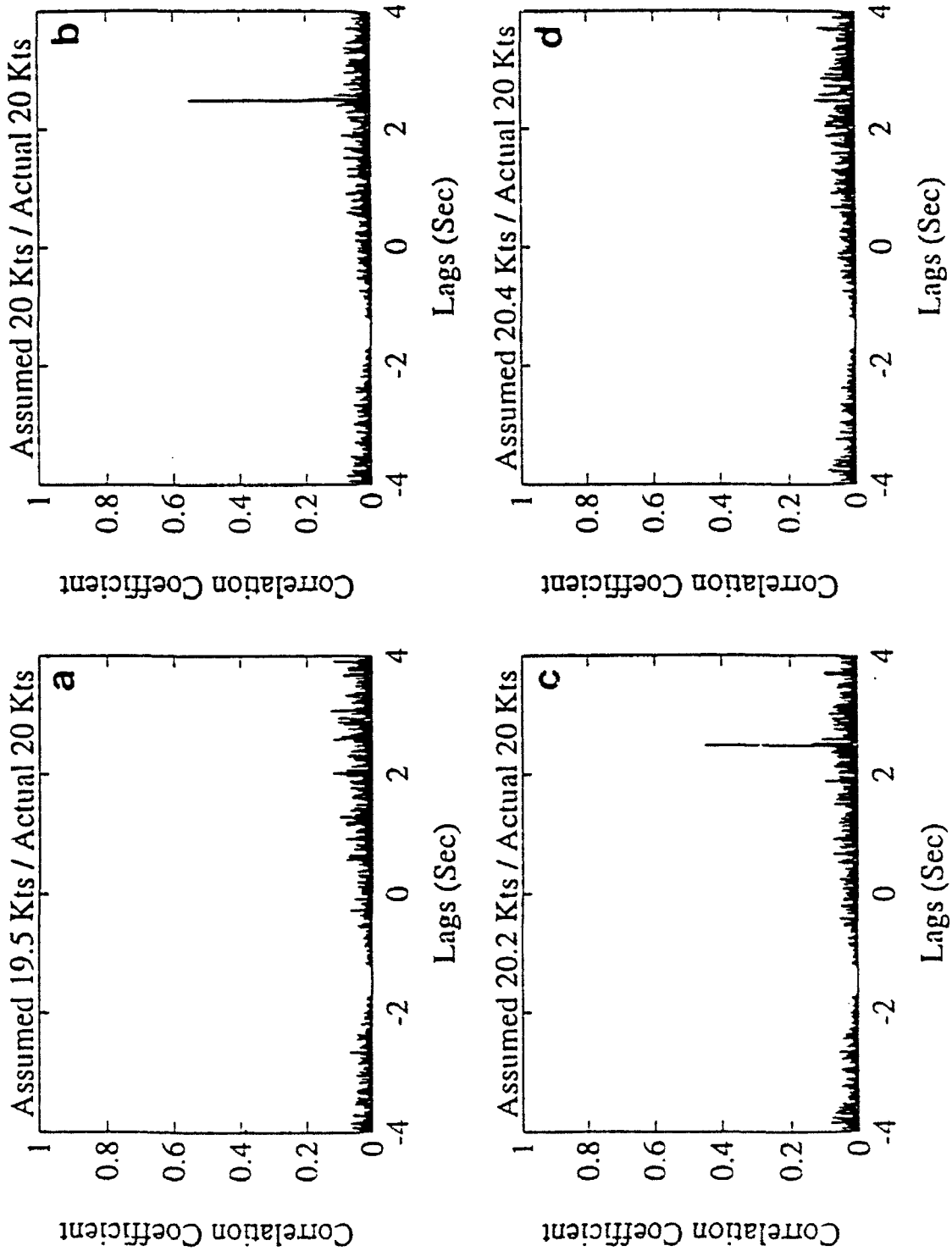


Figure D-6. Replica Correlations for Doppler-Shifted Lorenz Echoes in Case 6 with an Actual Doppler of 20 Knots and Assumed Dopplers of: (a) 19.5 Knots; (b) 20 Knots; (c) 20.2 Knots; and (d) 20.4 Knots.

APPENDIX E

PHASE PLOTS OF DISTORTED SIGNALS

Figures E-1 through E-4 illustrate the effects upon phase plots of ocean propagation and Doppler-shifts to the Lorenz, Duffing, Henon, and Iterative waveforms, respectively. The time delays used to generate the phase plots are as follows: three samples for the Lorenz and Duffing; one sample for the Henon and Iterative waveforms. That is, the plots are of pairs, $[W(n), W(n+3)]$, for the Lorenz and Duffing, and $[W(n), W(n+1)]$ for the Henon and Iterative, where $W(k)$ is the k^{th} sample of the waveform W . Only in the Duffing, and to a much lesser extent in the Lorenz, do the phase plots bear some semblance of the original phase plot.

Shown in each figure are two columns of four panels. Panel (a) is the phase plot of the undistorted waveform. The waveform has been modulated then demodulated in panel (b). Panel (c) is what would be seen at a stationary target were the signal demodulated, while panel (d) is of the demodulated echo at the receiver. The right column of panels are Doppler-shifted (20 knots relative motion) counterparts to the left column of panels. Panel (e) is the phase plot of the Doppler-shifted base band signal where as in panel (f) the modulated signal has been Doppler-shifted. Panels (g) and (h) are phase plots of the Doppler-shifted signal demodulated at the target and at the receiver, respectively.

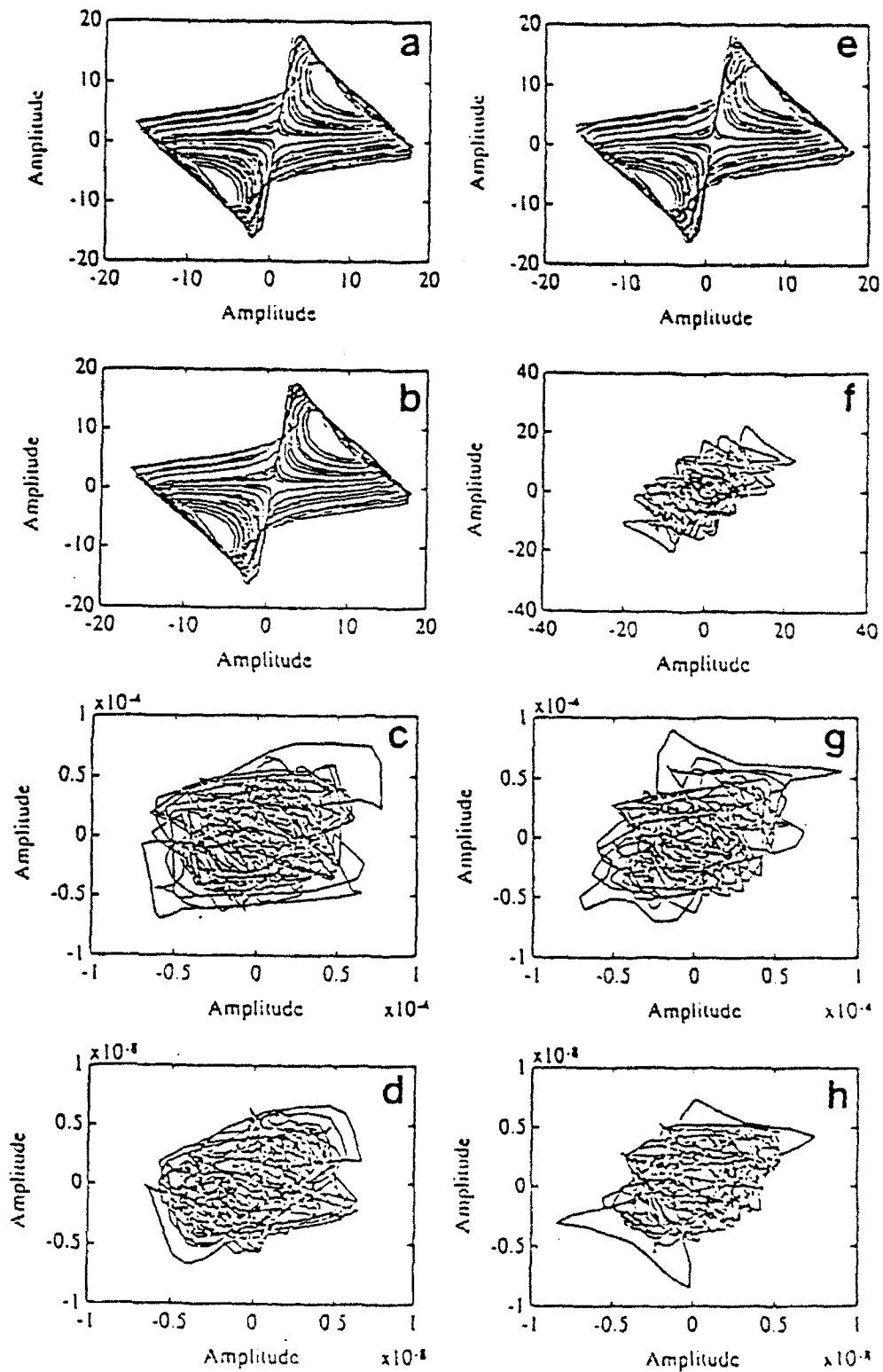


Figure E-1. Phase Plot of the Lorenz Waveform: (a) original; (b) modulated, then demodulated; (c) at target; (d) of echo; (e) Doppler-shifted; (f) modulated then Doppler-shifted; (g) at target, Doppler-shifted; (h) Doppler-shifted echo.

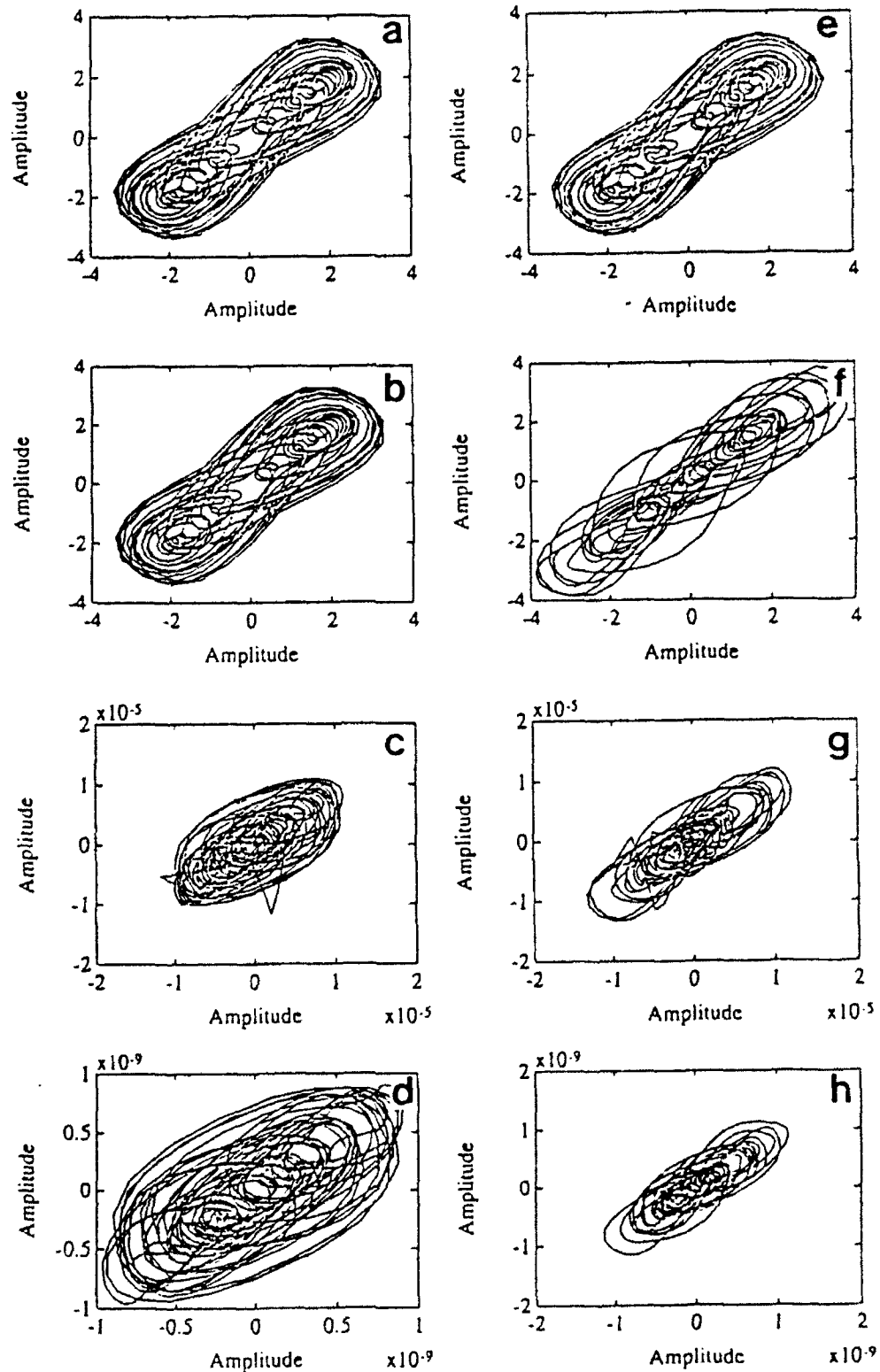


Figure E-2. Phase Plot of the Duffing Waveform: (a) original; (b) modulated, then demodulated; (c) at target; (d) of echo; (e) Doppler-shifted; (f) modulated then Doppler-shifted; (g) at target, Doppler-shifted; (h) Doppler-shifted echo.

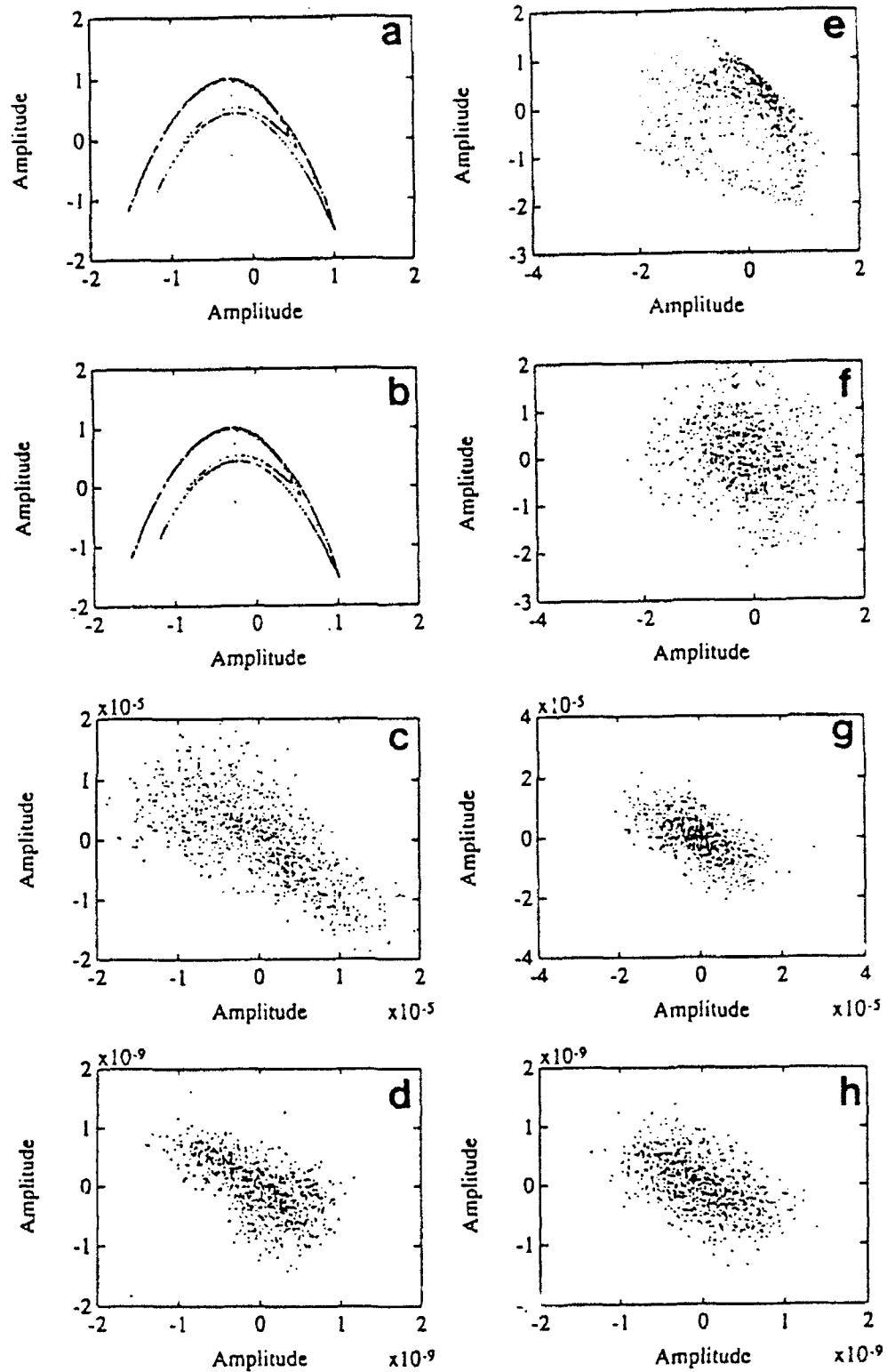


Figure E-3. Phase Plot of the Henon Waveform: (a) original; (b) modulated, then demodulated; (c) at target; (d) of echo; (e) Doppler-shifted; (f) modulated then Doppler-shifted; (g) at target, Doppler-shifted; (h) Doppler-shifted echo.

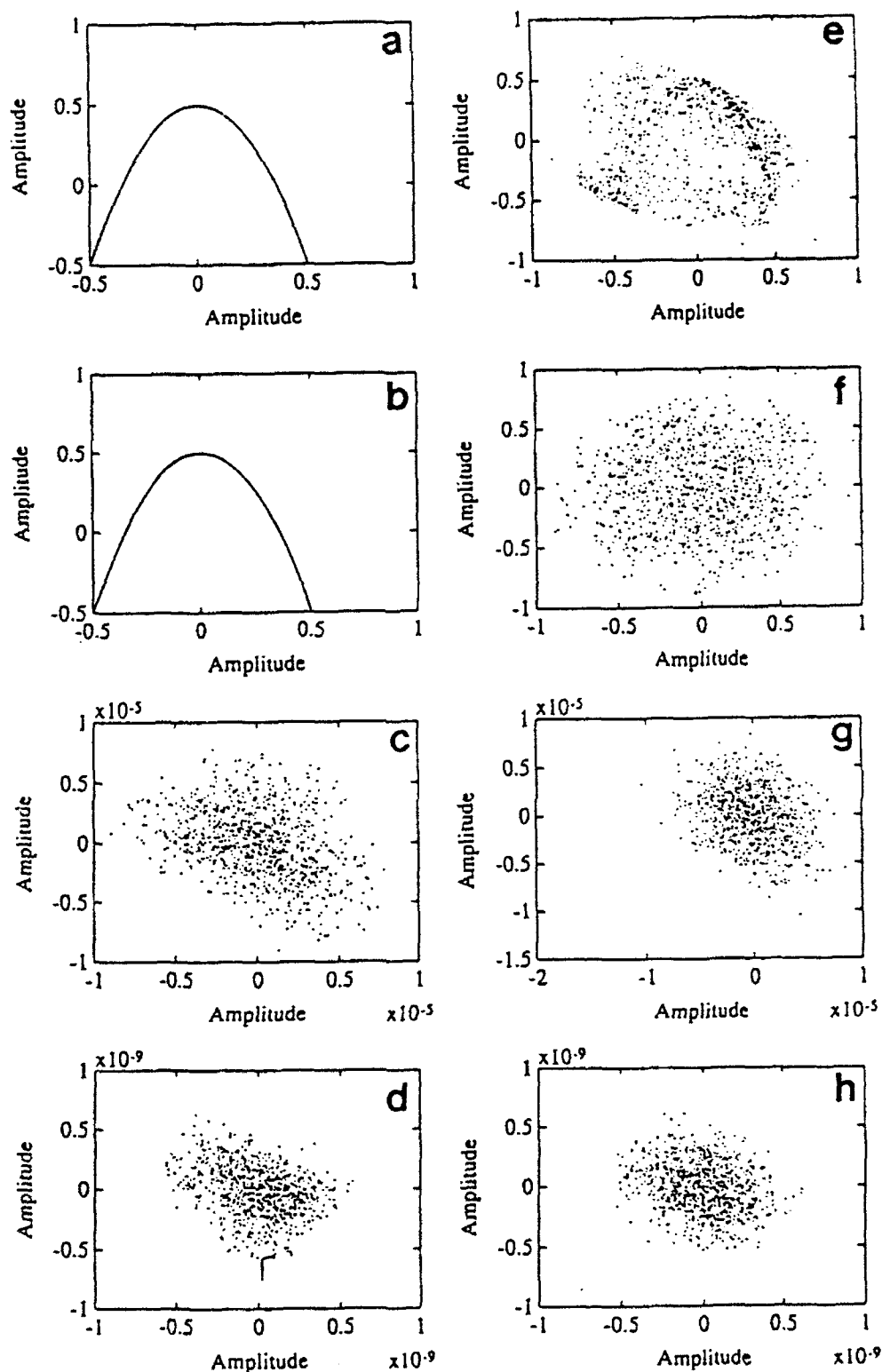


Figure E-4. Phase Plot of the Iterative Waveform: (a) original; (b) modulated, then demodulated; (c) at target; (d) of echo; (e) Doppler-shifted; (f) modulated then Doppler-shifted; (g) at target, Doppler-shifted; (h) Doppler-shifted echo.

APPENDIX F

STEREOSCOPIC PROJECTIONS

Figures F-1 and F-2 present stereoscopic pairs of waveforms embedded in three dimensions. The Lorenz and Duffing pairs are shown in Figure F-1, while the Henon and Iterative are shown in Figure F-2. If the reader is able to perceive three dimensions from these panels, then it will be seen that along the horizontal of the Lorenz, at an amplitude of about zero, there is a deep trough. Another striking feature is seen in Figure F-2 from the Iterative; the points appear to come sharply out of the paper starting at an amplitude of about -0.4.

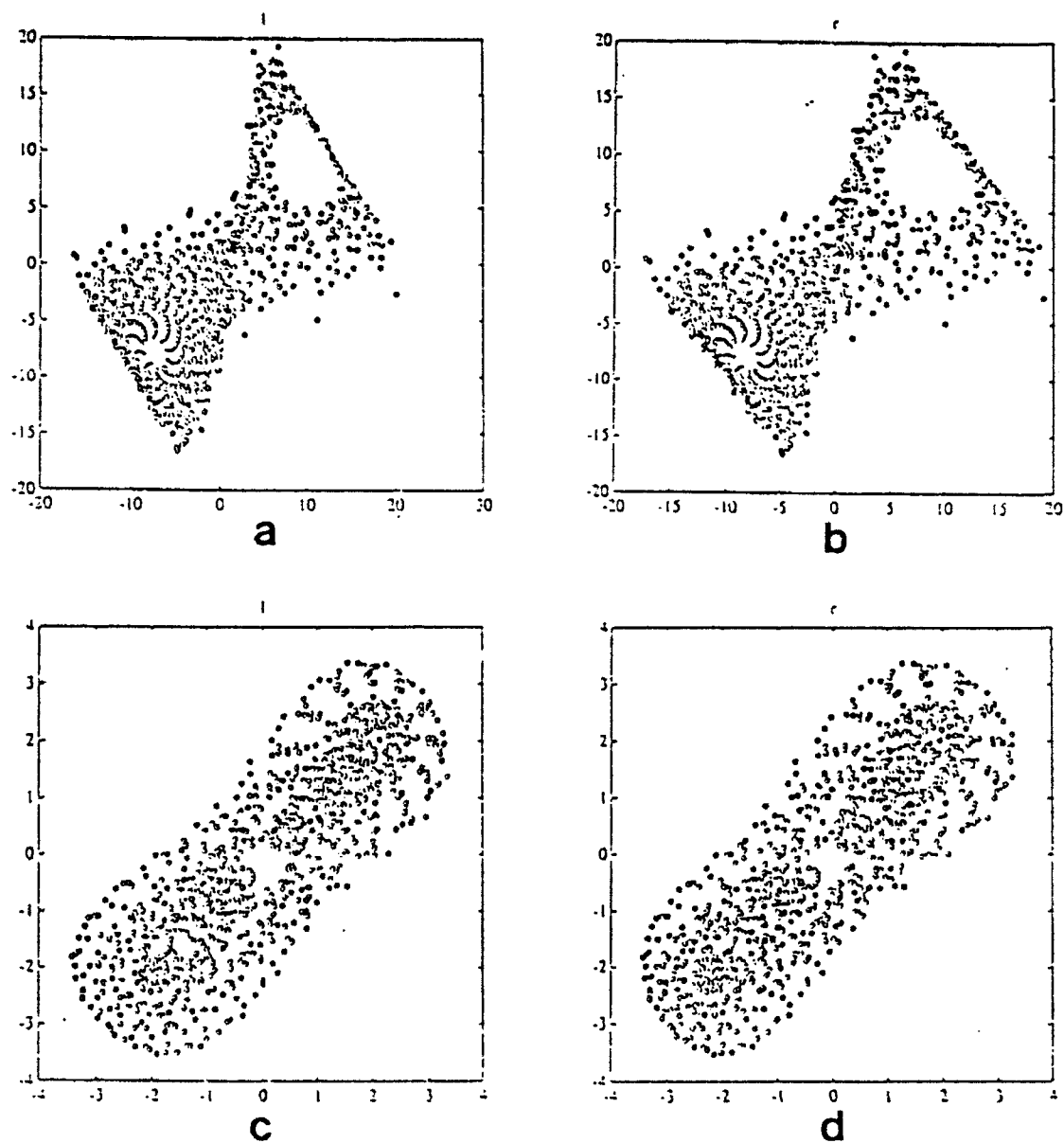


Figure F-1. Stereoscopic Pairs of the Lorenz (a,b) and Duffing (c,d) Waveform Phase Plots Embedded in Three Dimensions.

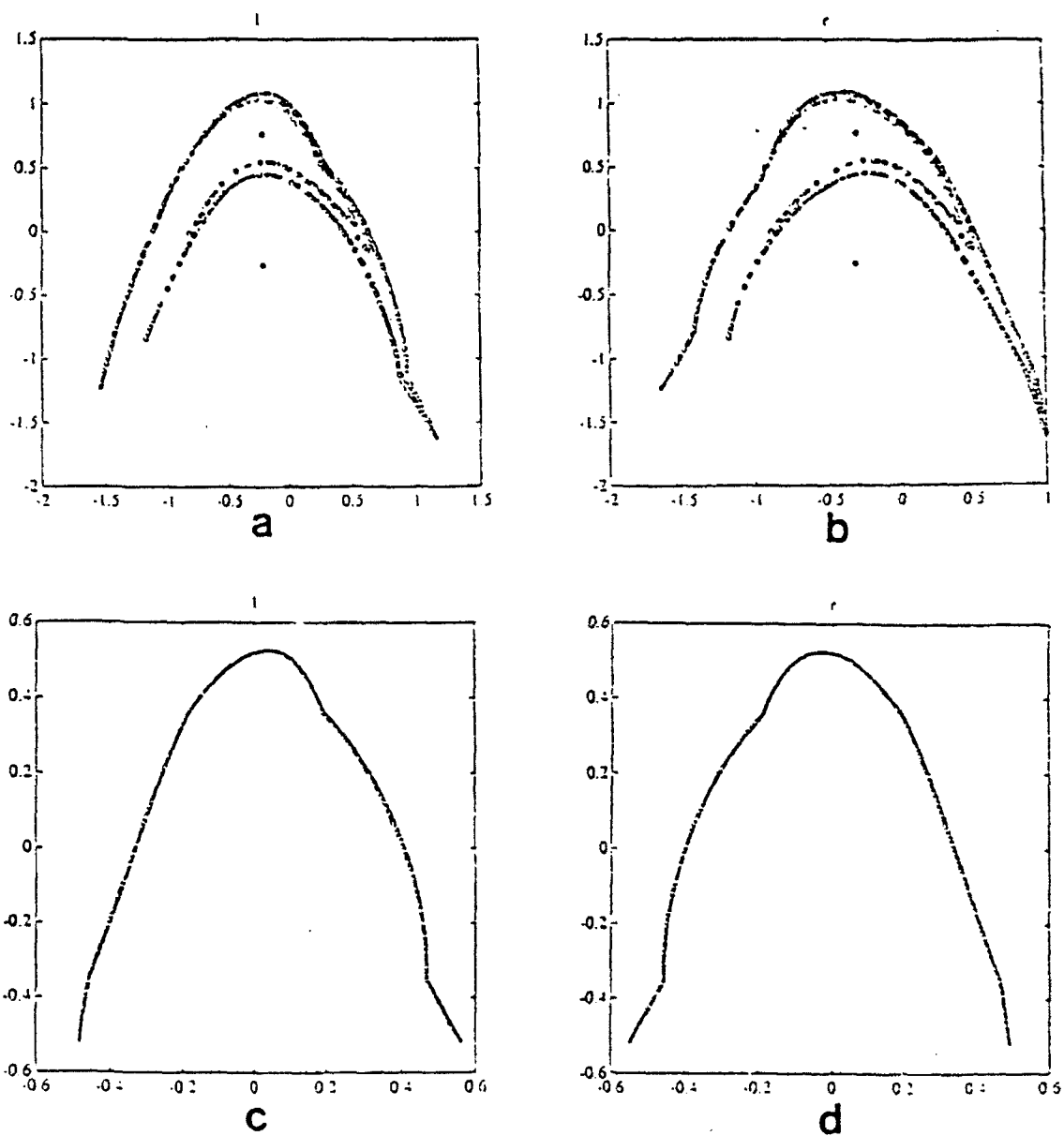


Figure F-2. Stereoscopic Pairs of the Henon (a,b) and Iterative (c,d) Waveform Phase Plots Embedded in Three Dimensions.

APPENDIX G

CORRELATION DIMENSION

Figures G-1 through G-23 present curves of the logarithm of $C^m(r)$ as a function of the logarithm of r as defined in Section 2.5.1, page 11 in the body of this report. These curves are used to extract the correlation dimension. The curves should be linear, or in practice, partially linear. The correlation dimension is the slope of the linear portion of the curves.

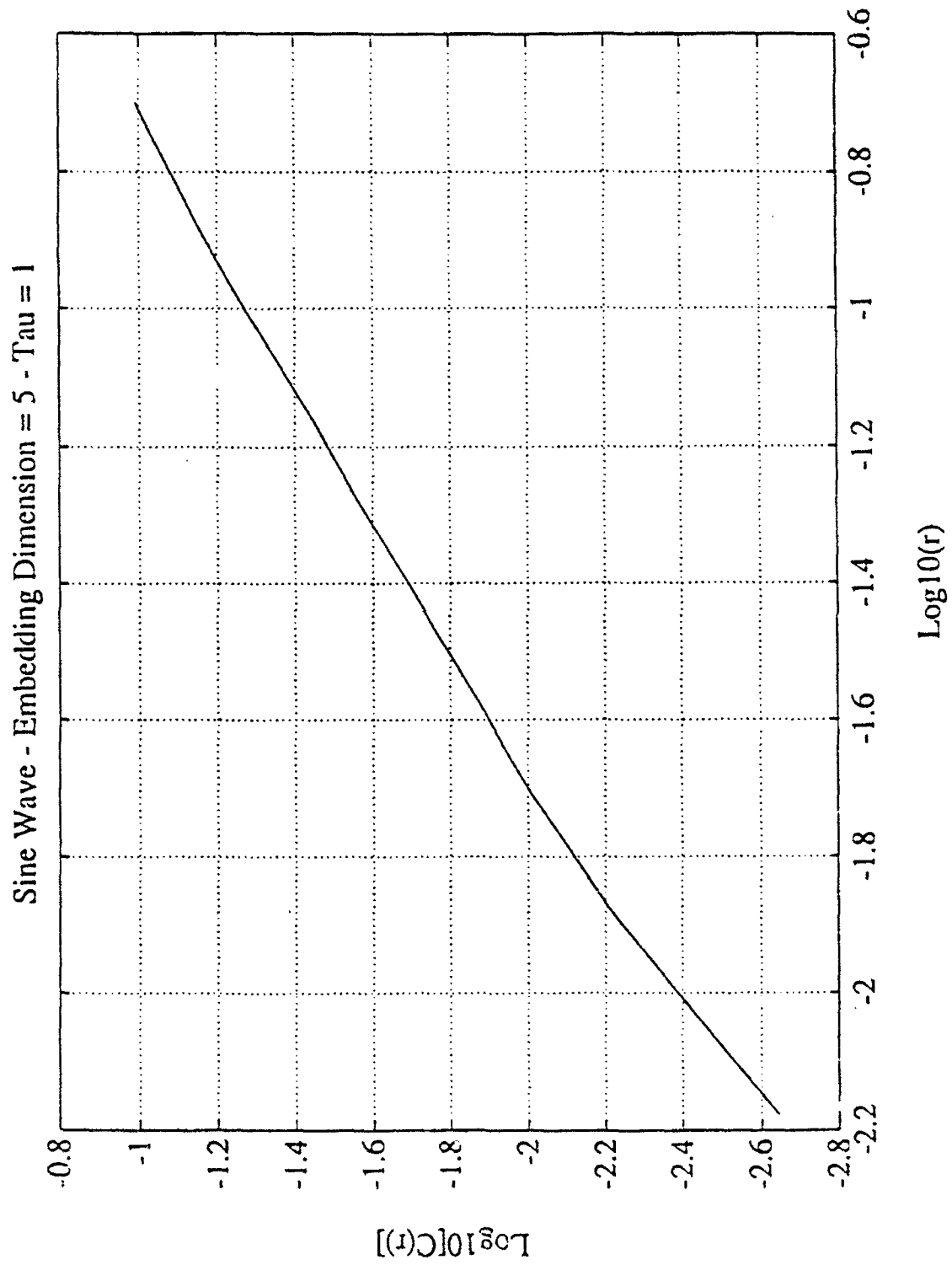


Figure G-1. Correlation Dimension Extraction Curve for Sine Wave Embedded in 5 Dimensions.

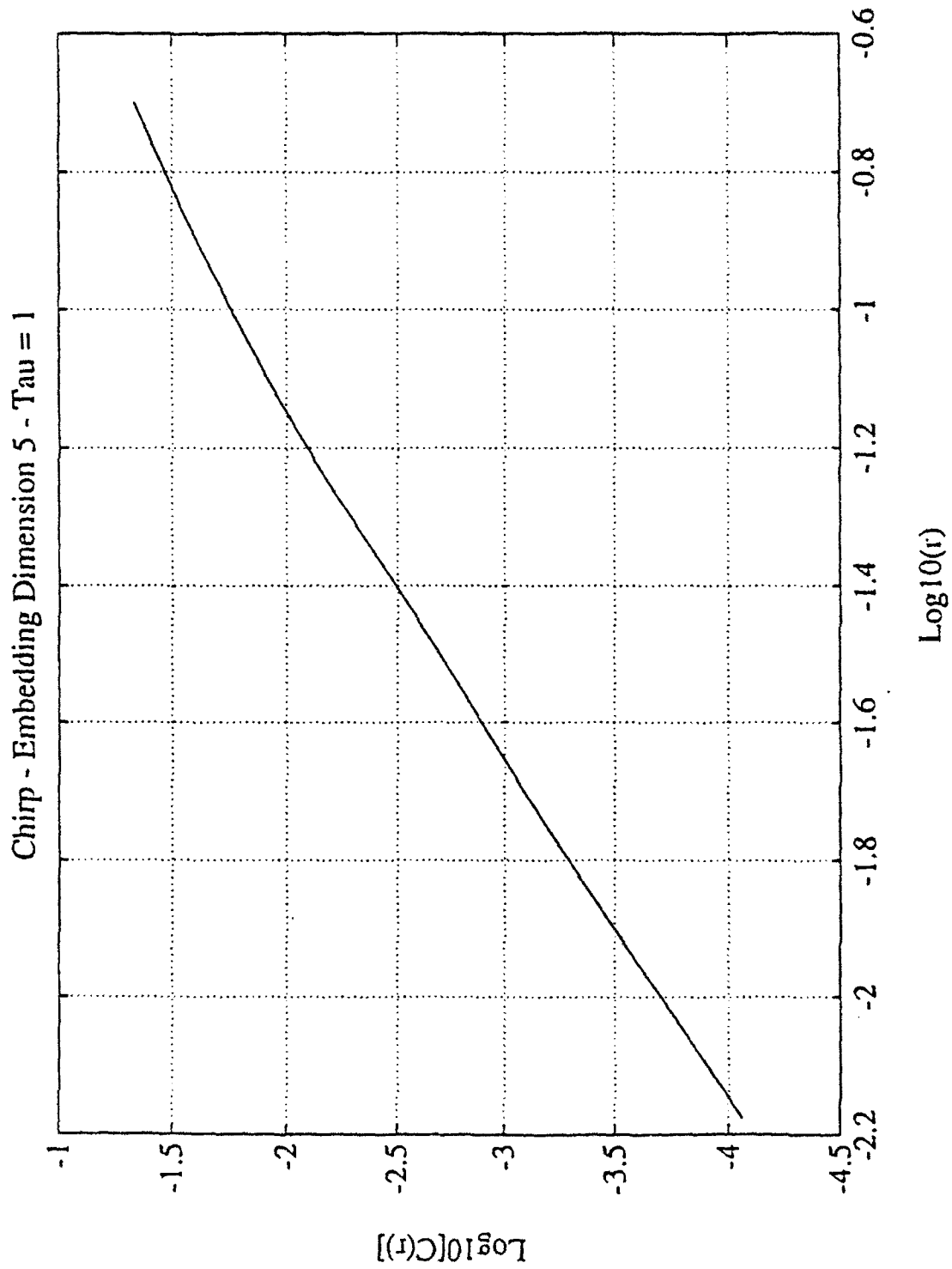


Figure G-2. Correlation Dimension Extraction Curve for Chirp Embedded in 5 Dimensions.

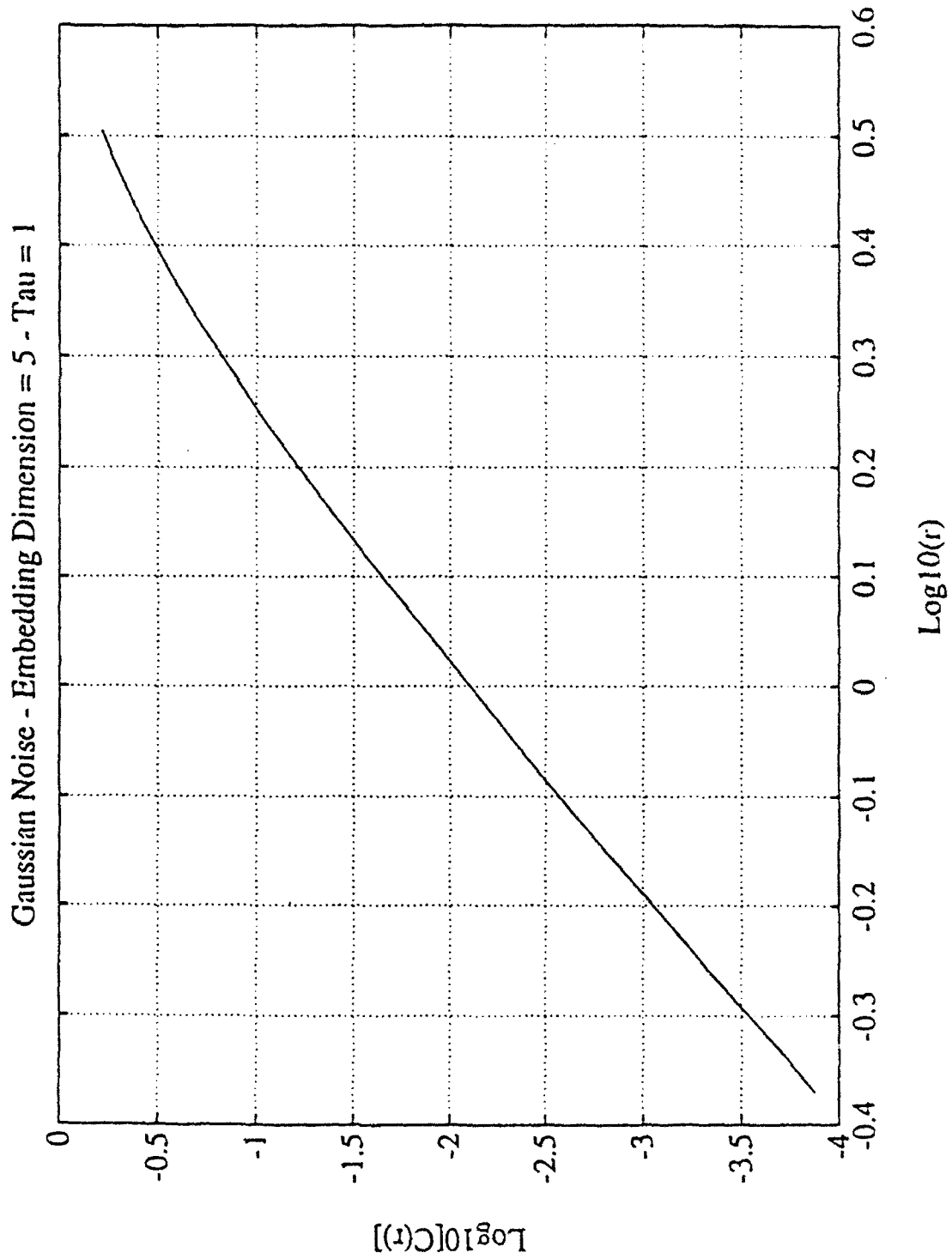


Figure G-3. Correlation Dimension Extraction Curve for Gaussian Noise Embedded in 5 Dimensions.

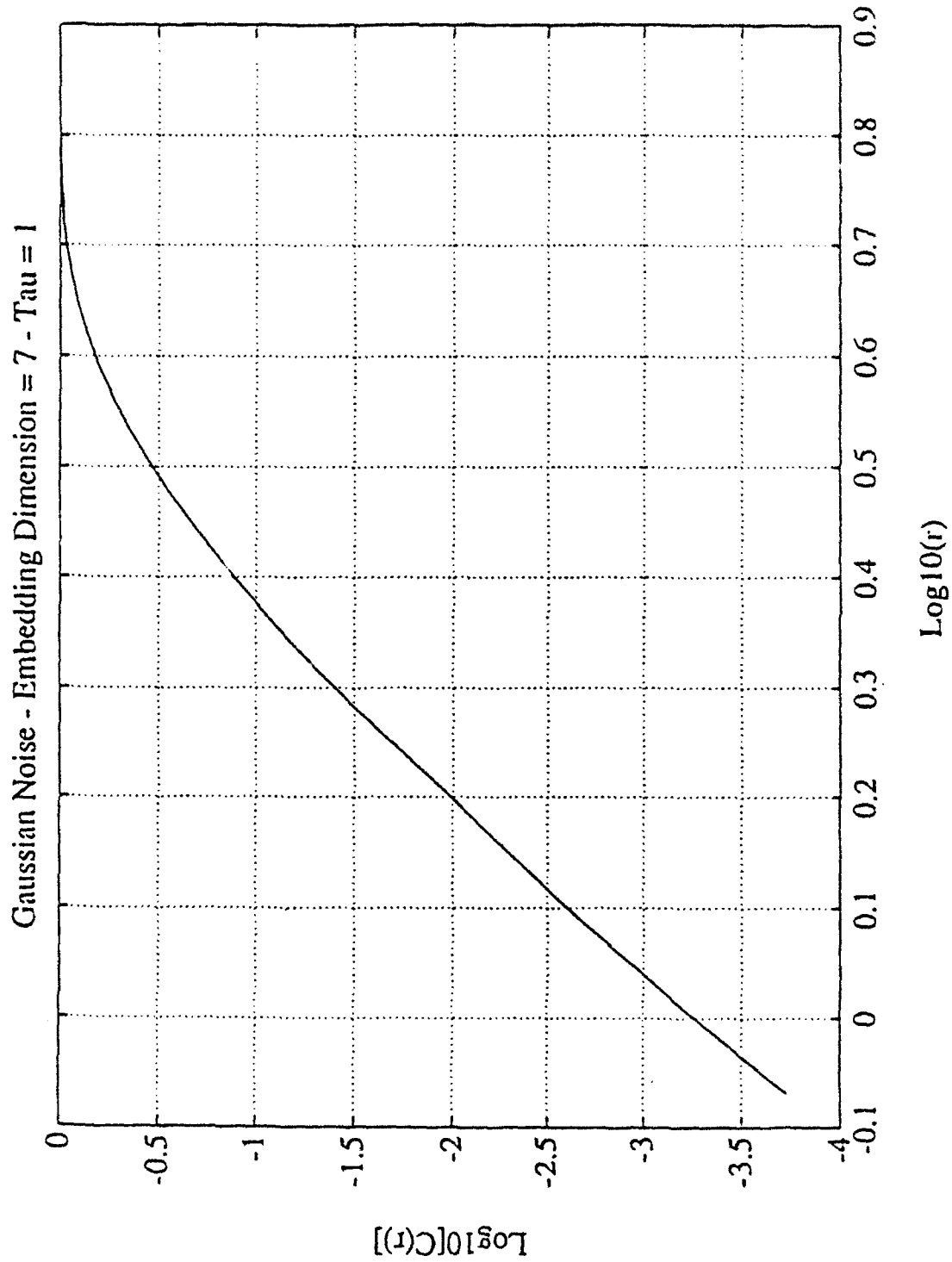


Figure G-4. Correlation Dimension Extraction Curve for Gaussian Noise Embedded in 7 Dimensions.

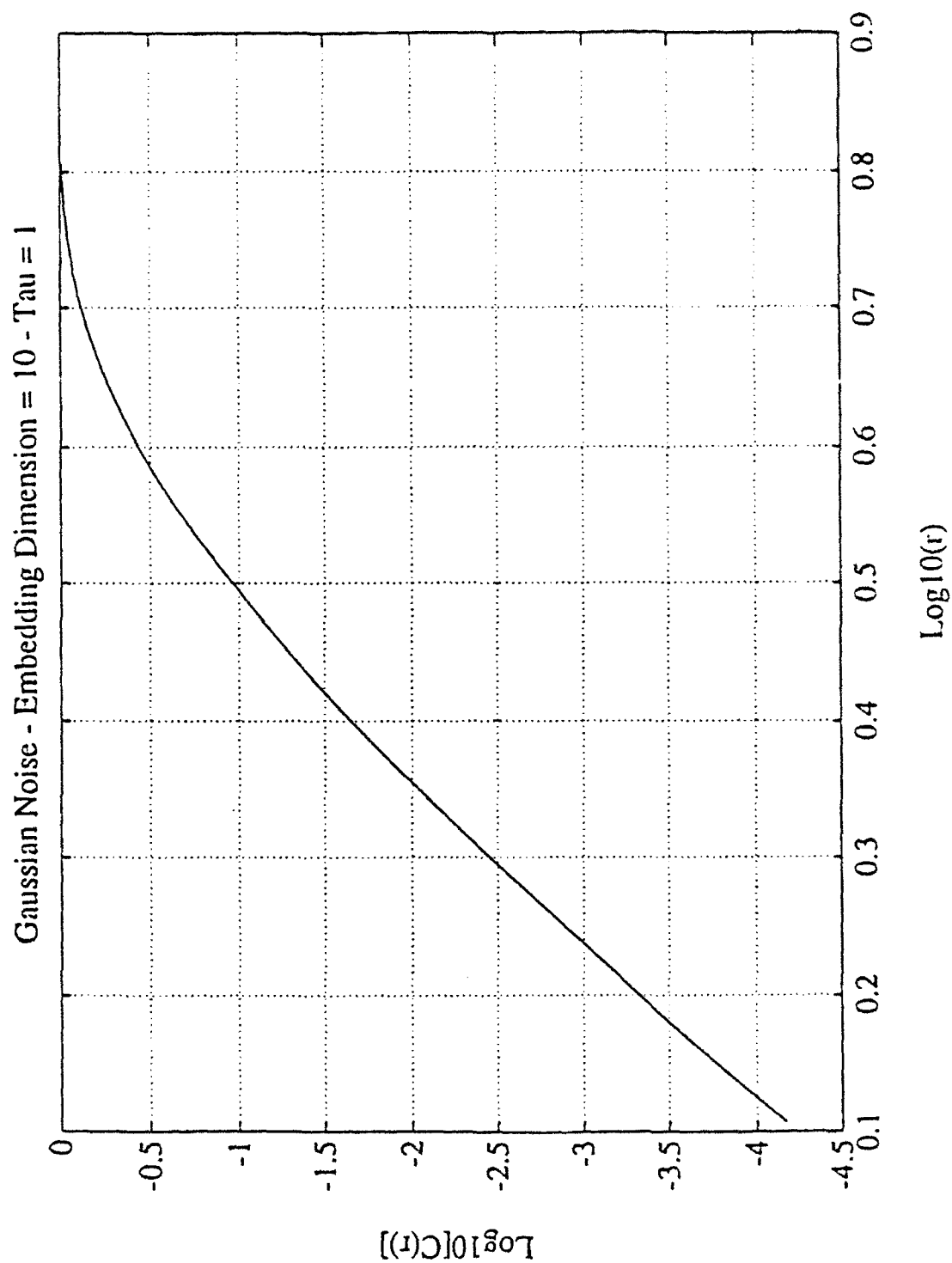


Figure G-5. Correlation Dimension Extraction Curve for Gaussian Noise Embedded in 10 Dimensions.

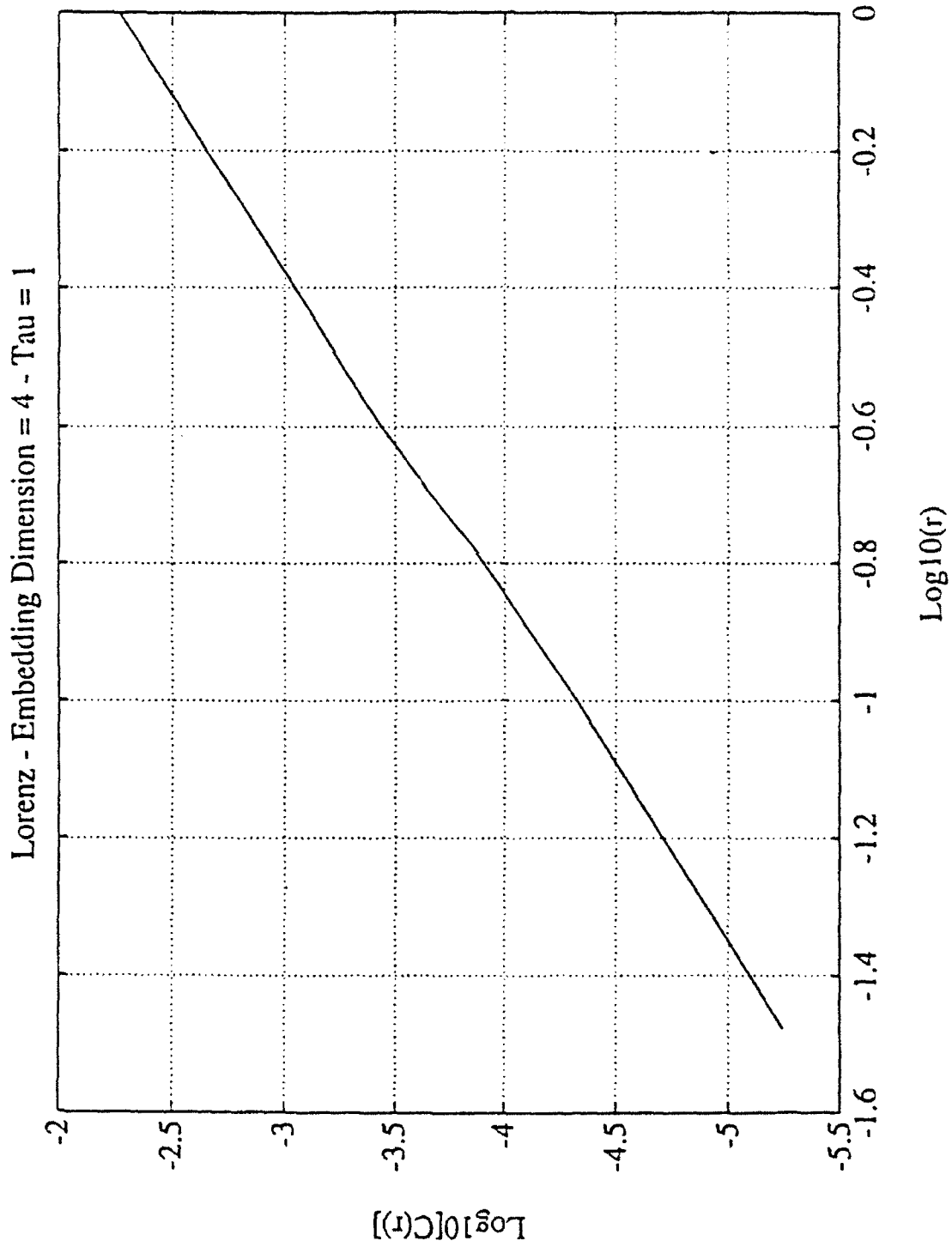


Figure G-6. Correlation Dimension Extraction Curve for Lorenz Waveform Embedded in 4 Dimensions.

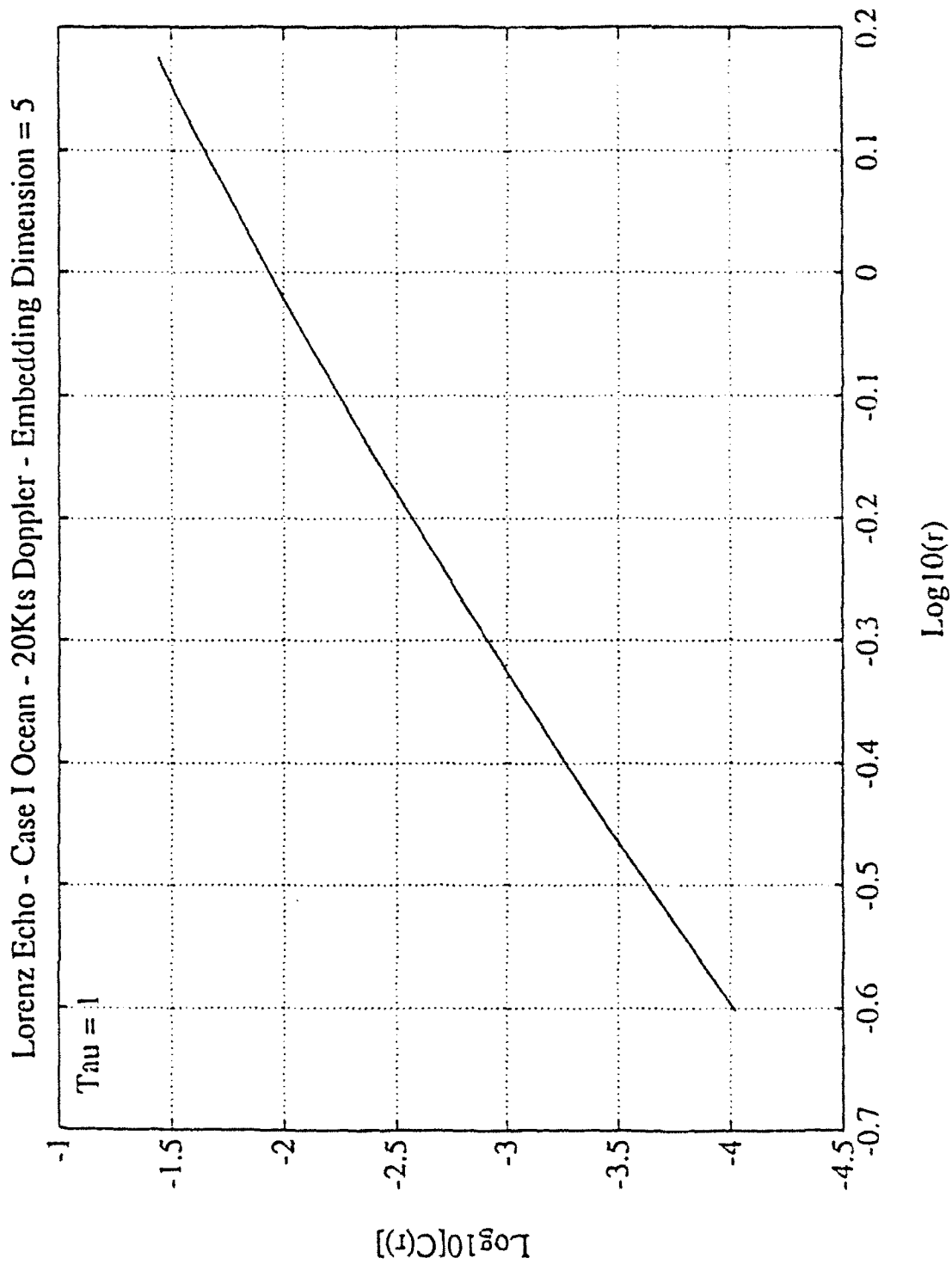


Figure G-7. Correlation Dimension Extraction Curve for Lorenz Waveform Propagated Through Case 1 Ocean with 20 Knots Doppler, Embedded in 5 Dimensions.

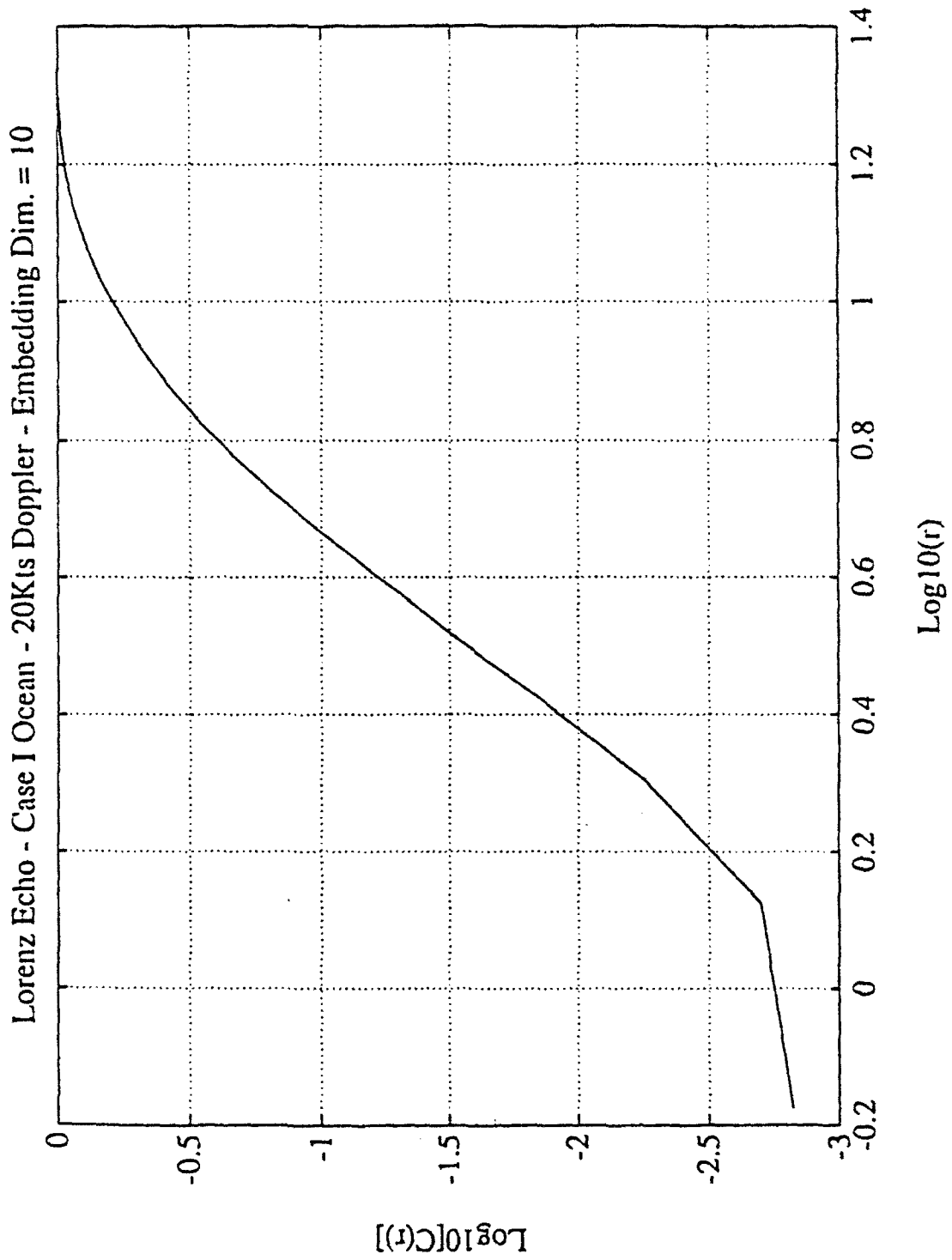


Figure G-8. Correlation Dimension Extraction Curve for Lorenz Waveform Propagated Through Case 1 Ocean with 20 Knots Doppler, Embedded in 10 Dimensions.

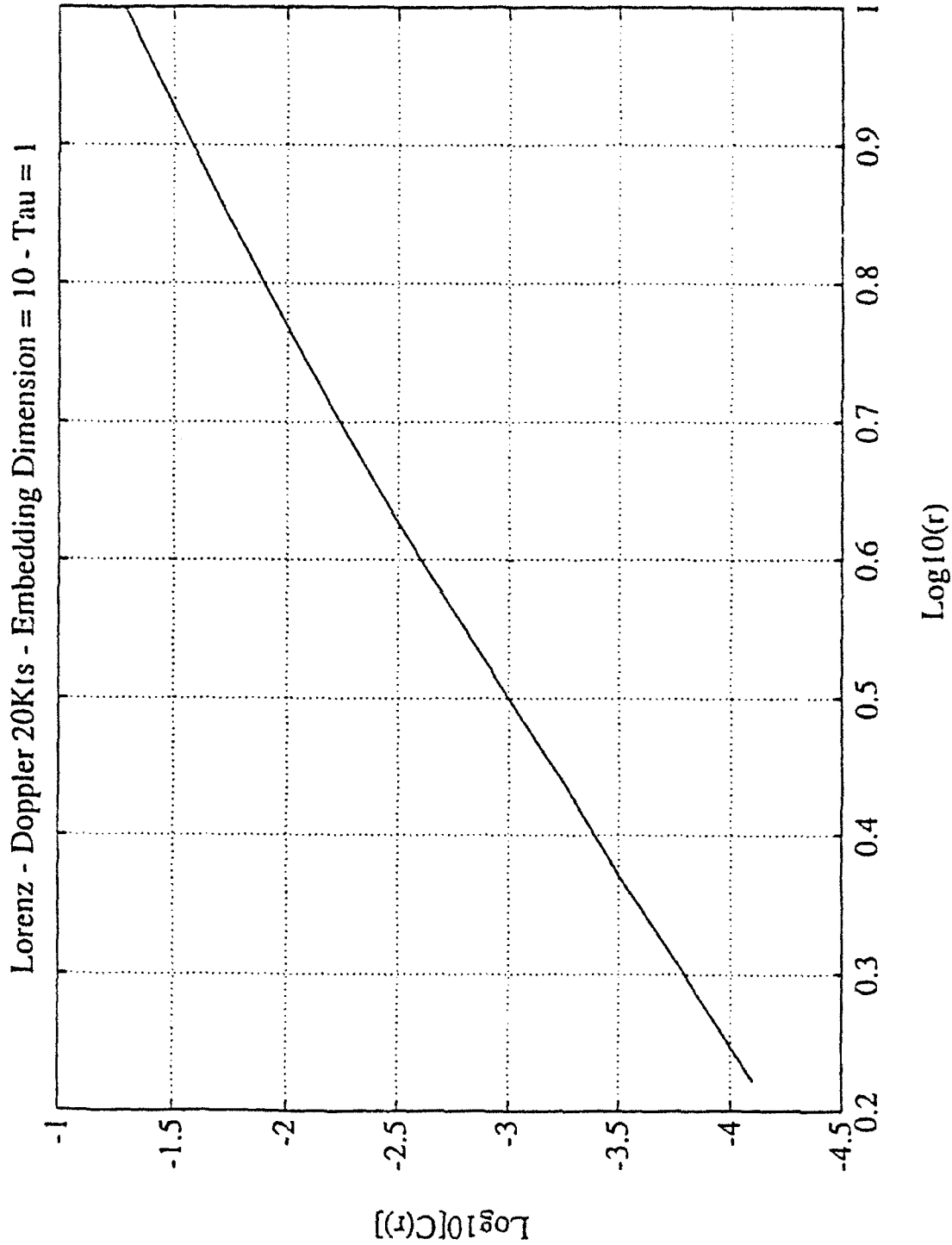


Figure G-9. Correlation Dimension Extraction Curve for Lorenz Waveform with 20 Knots Doppler, Embedded in 10 Dimensions.

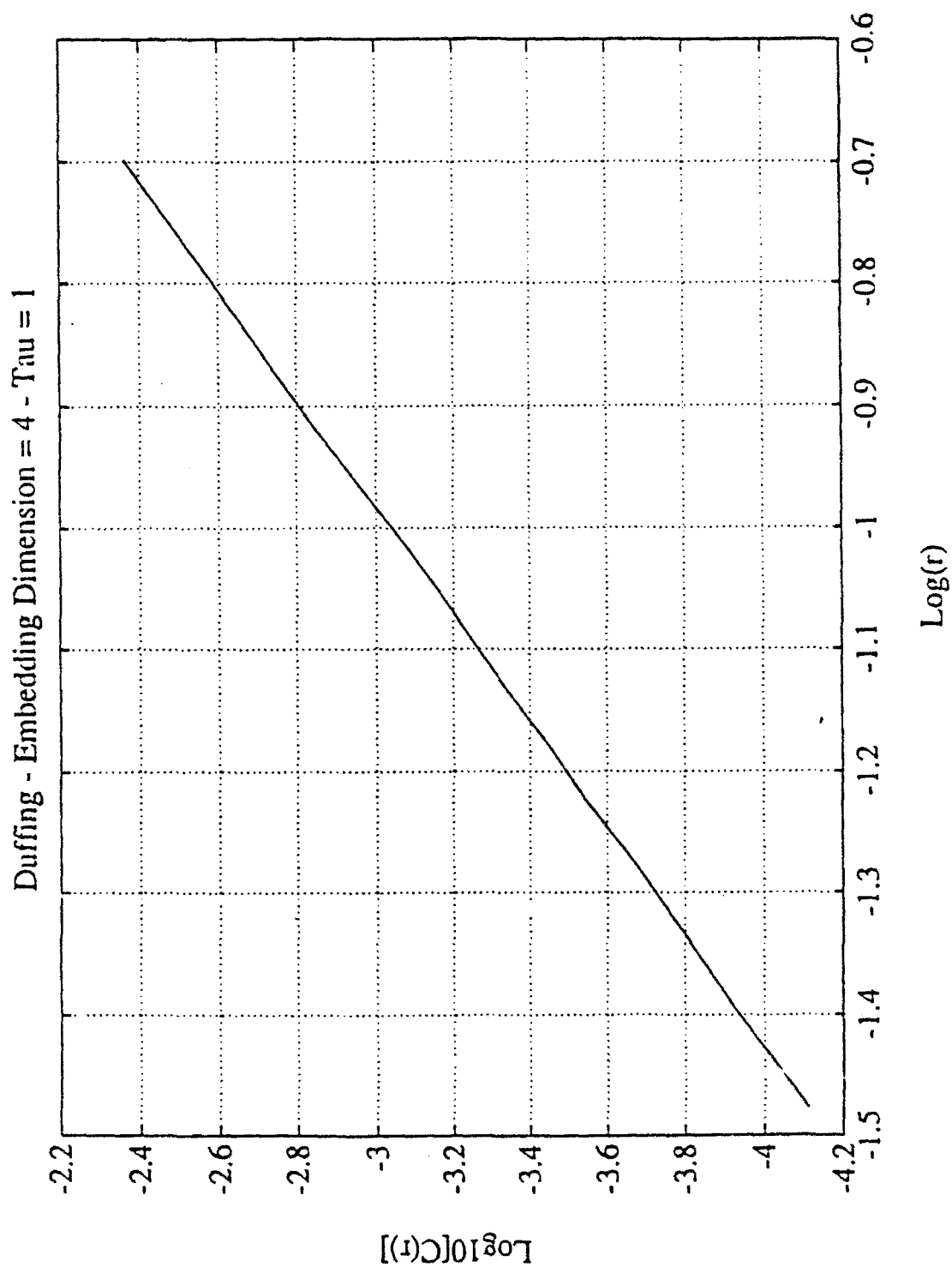


Figure G-10. Correlation Dimension Extraction Curve for Duffing Waveform Embedded in 4 Dimensions.

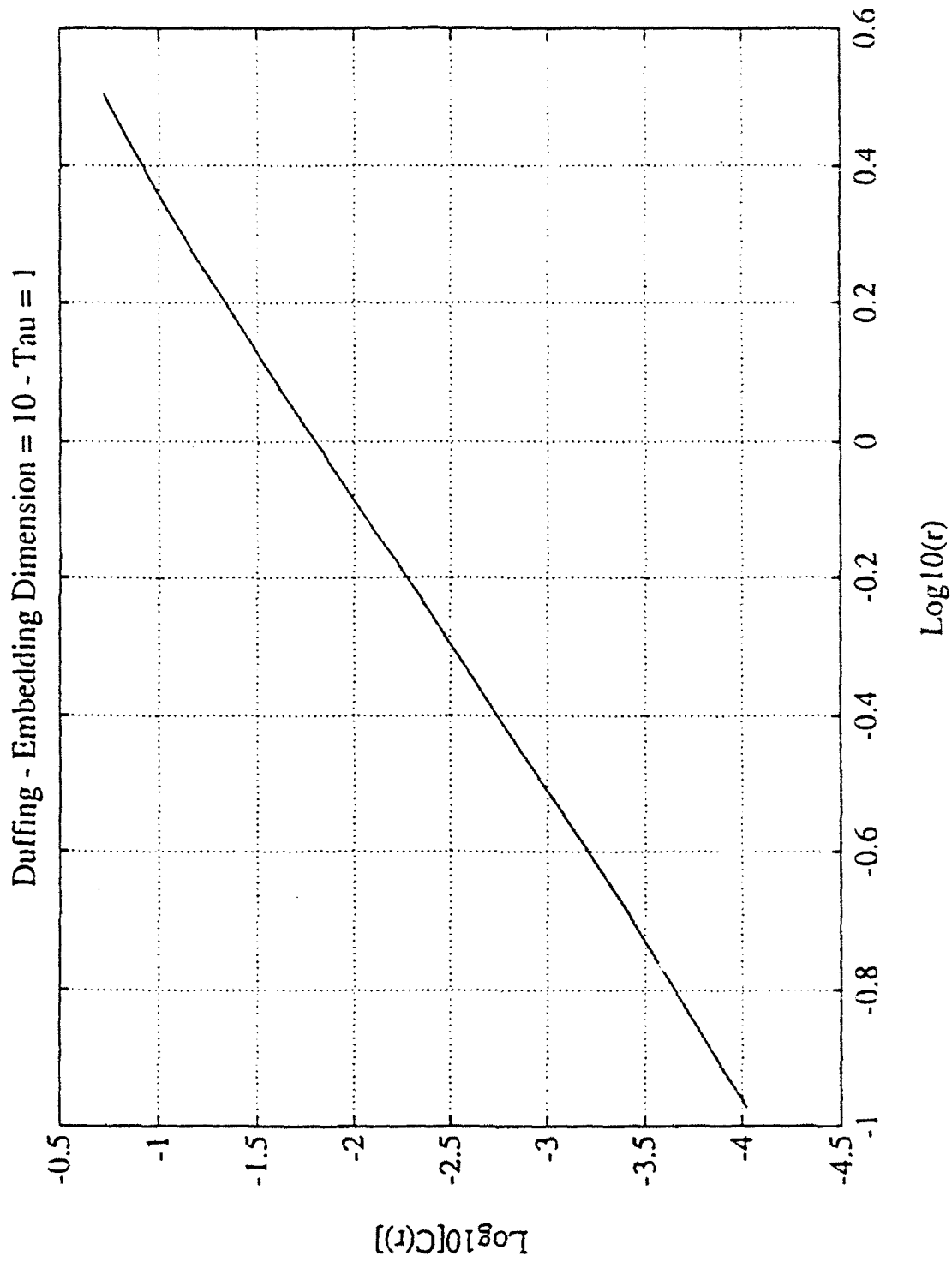


Figure G-11. Correlation Dimension Extraction Curve for Duffing Waveform Embedded in 10 Dimensions.

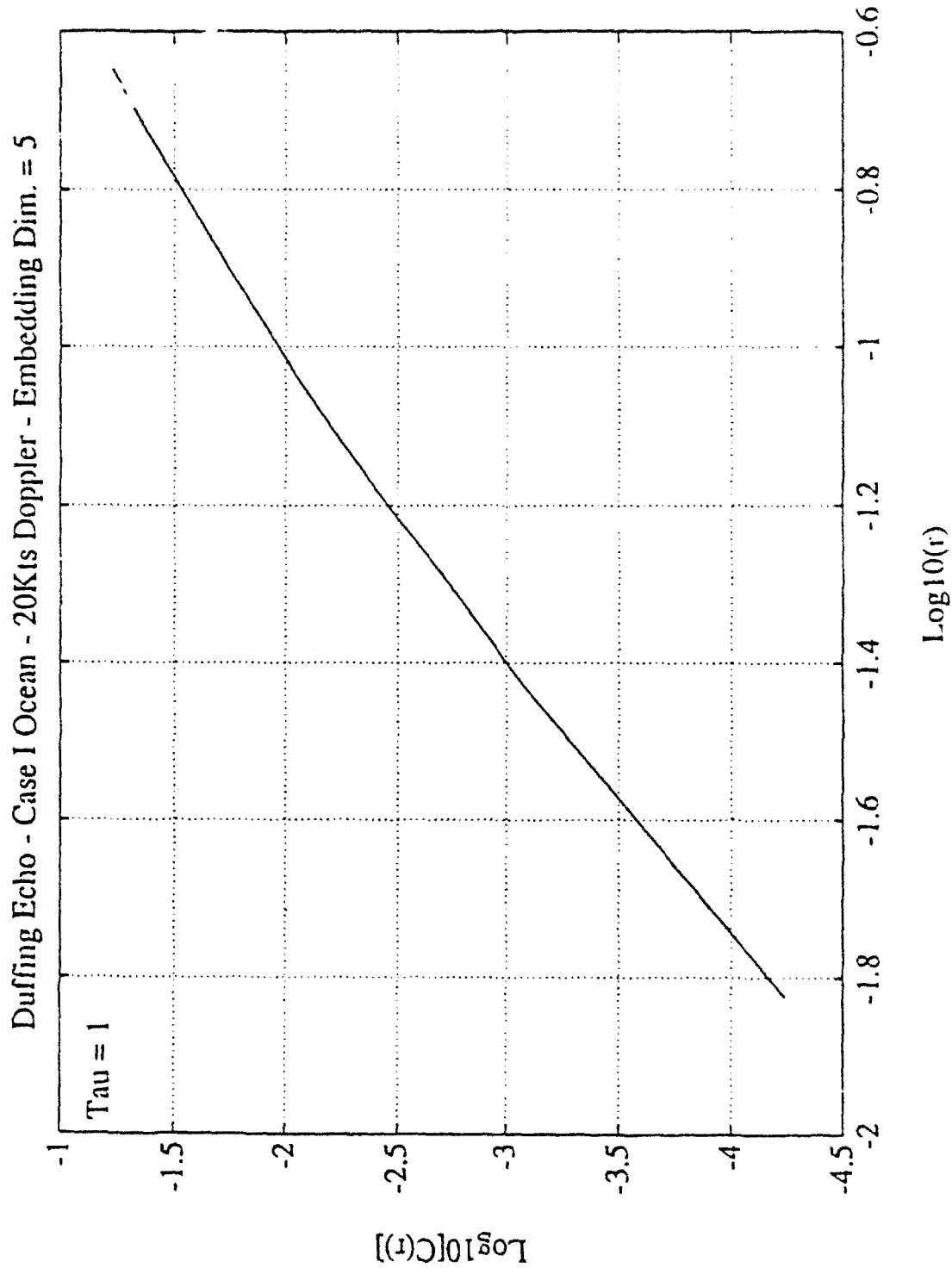


Figure G-12. Correlation Dimension Extraction Curve for Duffing Waveform Propagated Through Case 1 Ocean with 20 Knots Doppler, Embedded in 5 Dimensions.

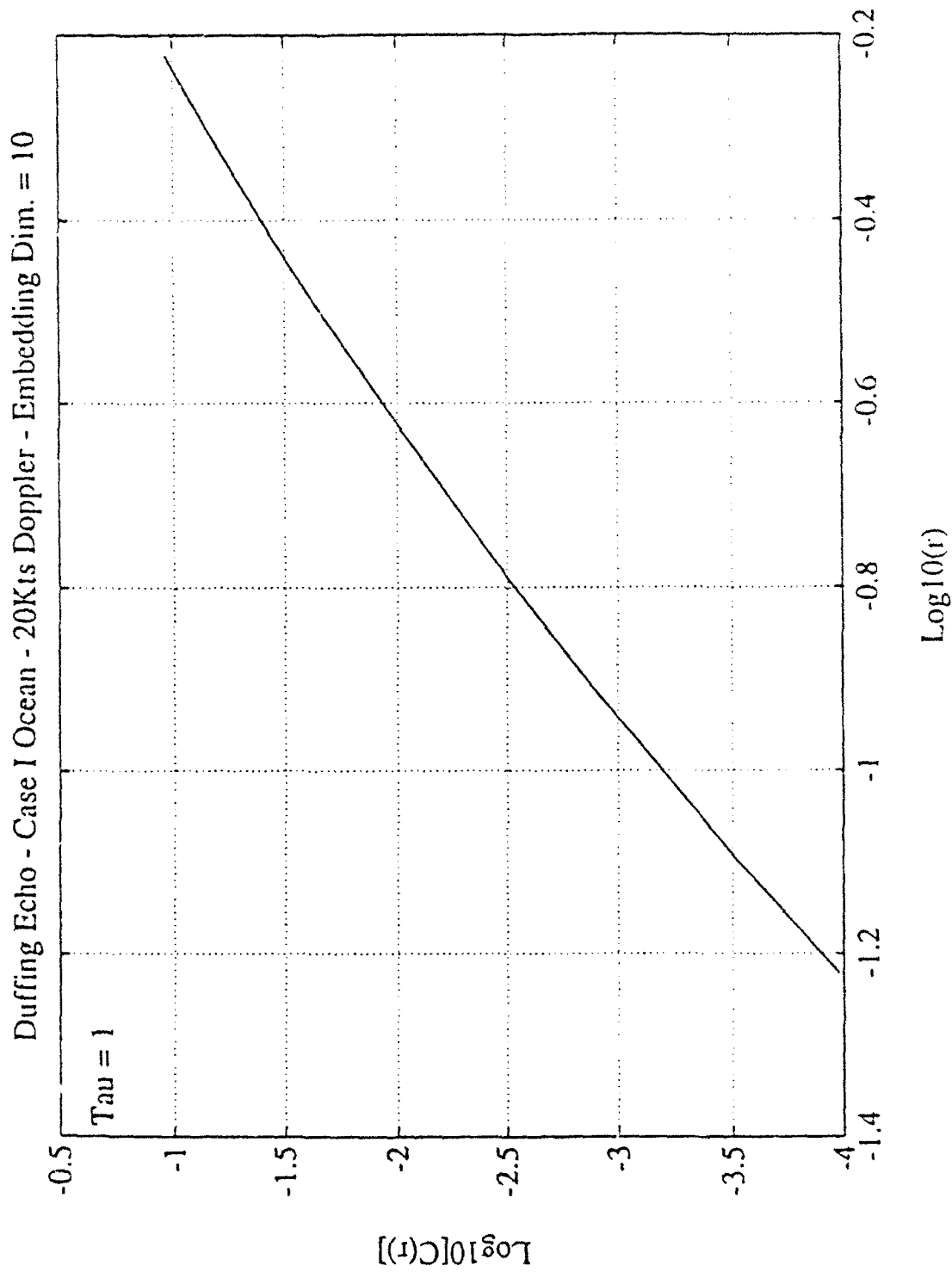


Figure G-13. Correlation Dimension Extraction Curve for Duffing Waveform Propagated Through Case 1 Ocean with 20 Knots Doppler, Embedded in 10 Dimensions.

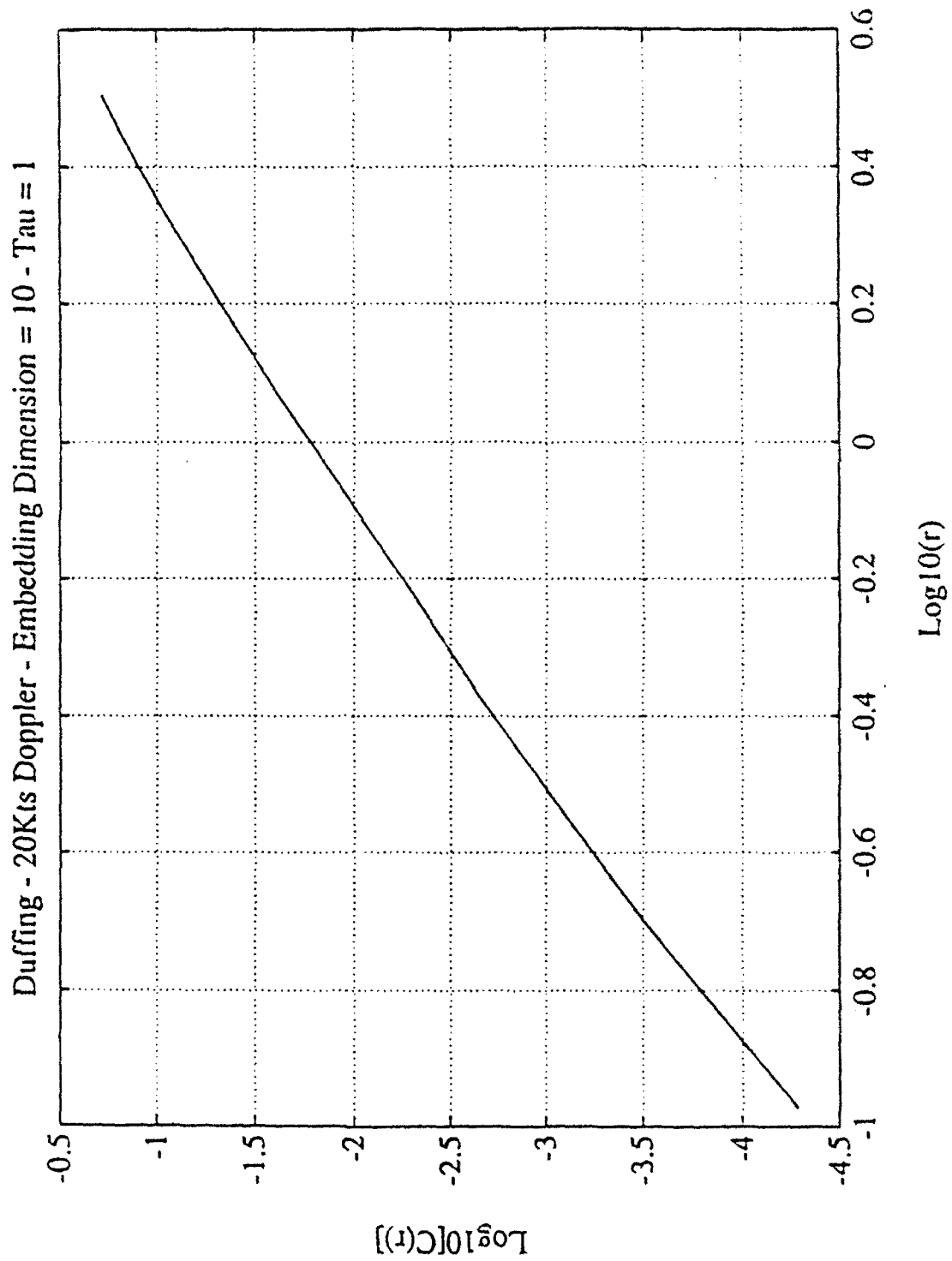


Figure G-14. Correlation Dimension Extraction Curve for Duffing Waveform with 20 Knots Doppler, Embedded in 10 Dimensions.

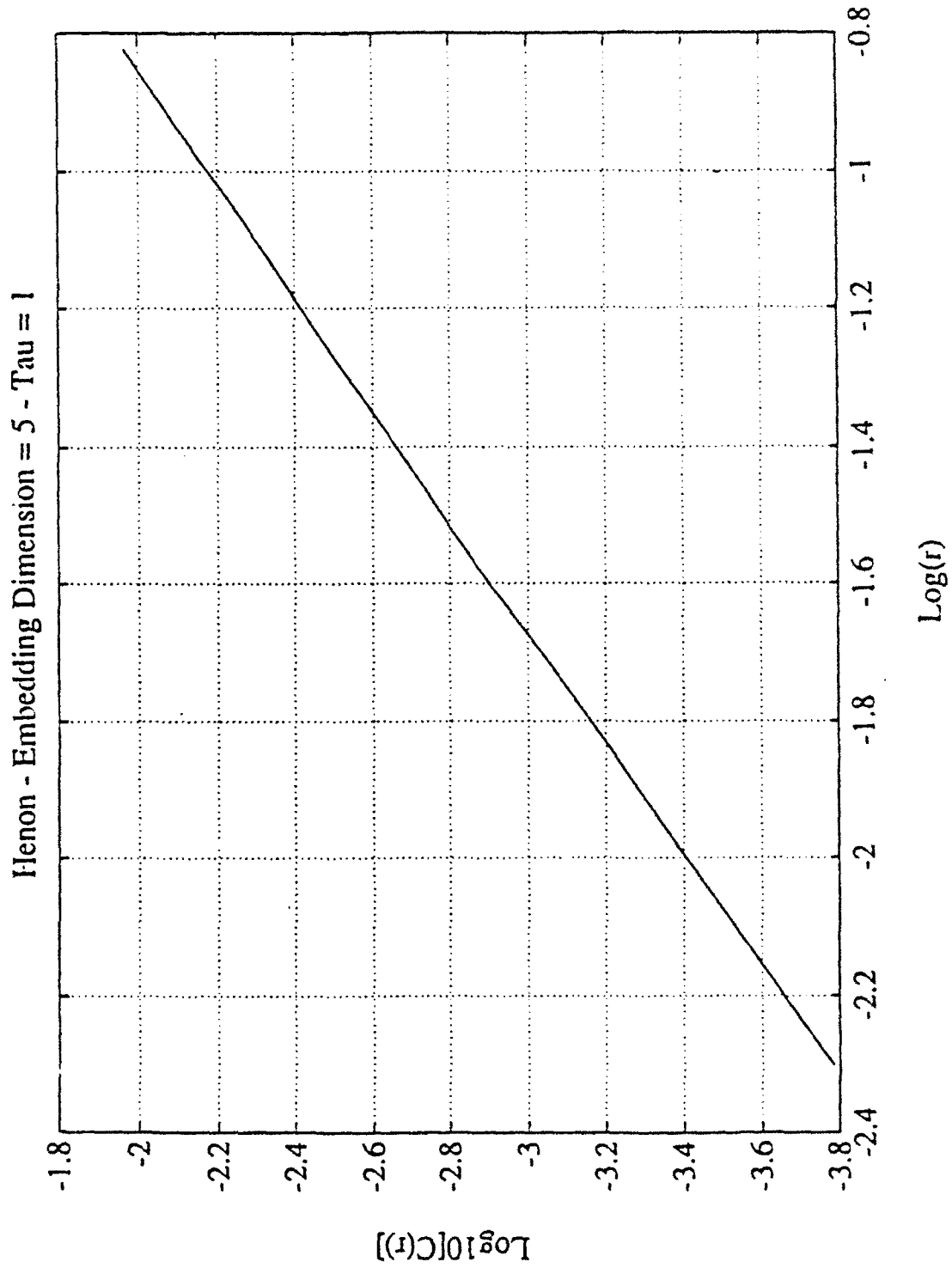


Figure G-15. Correlation Dimension Extraction Curve for Henon Waveform Embedded in 5 Dimensions.

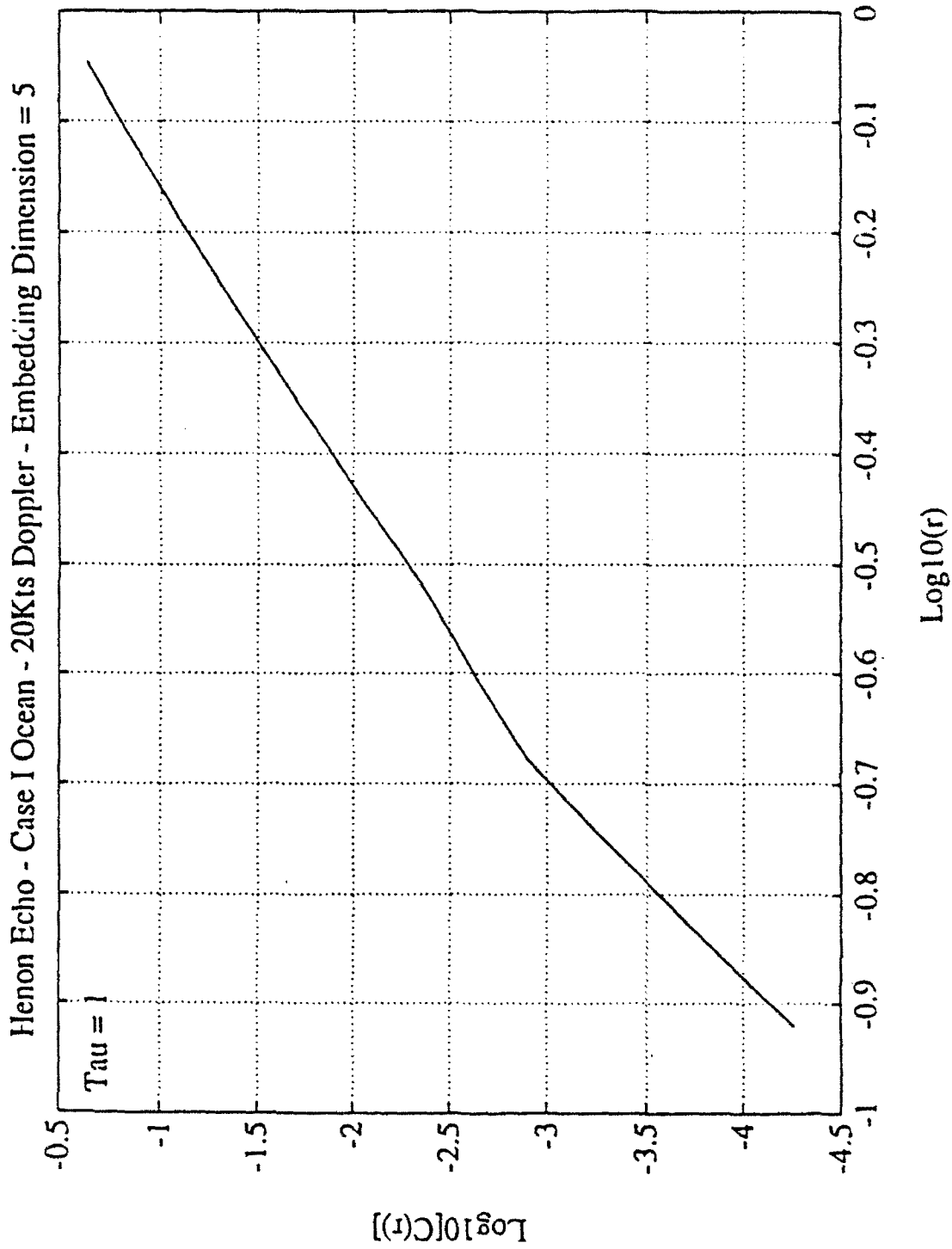


Figure G-16. Correlation Dimension Extraction Curve for Henon Waveform Propagated Through Case 1 Ocean with 20 Knots Doppler, Embedded in 5 Dimensions.

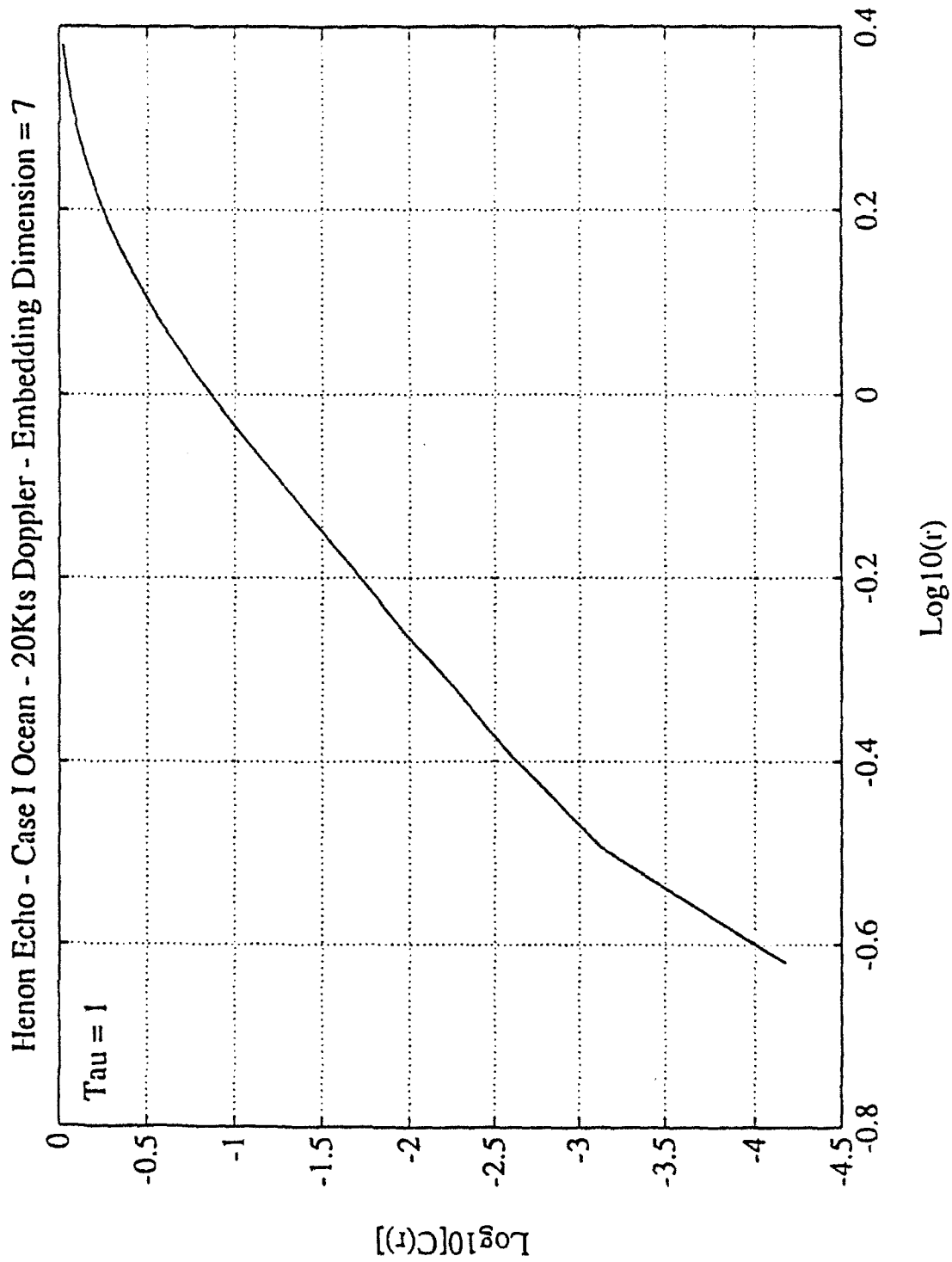


Figure G-17. Correlation Dimension Extraction Curve for Henon Waveform Propagated Through Case 1 Ocean with 20 Knots Doppler, Embedded in 7 Dimensions.

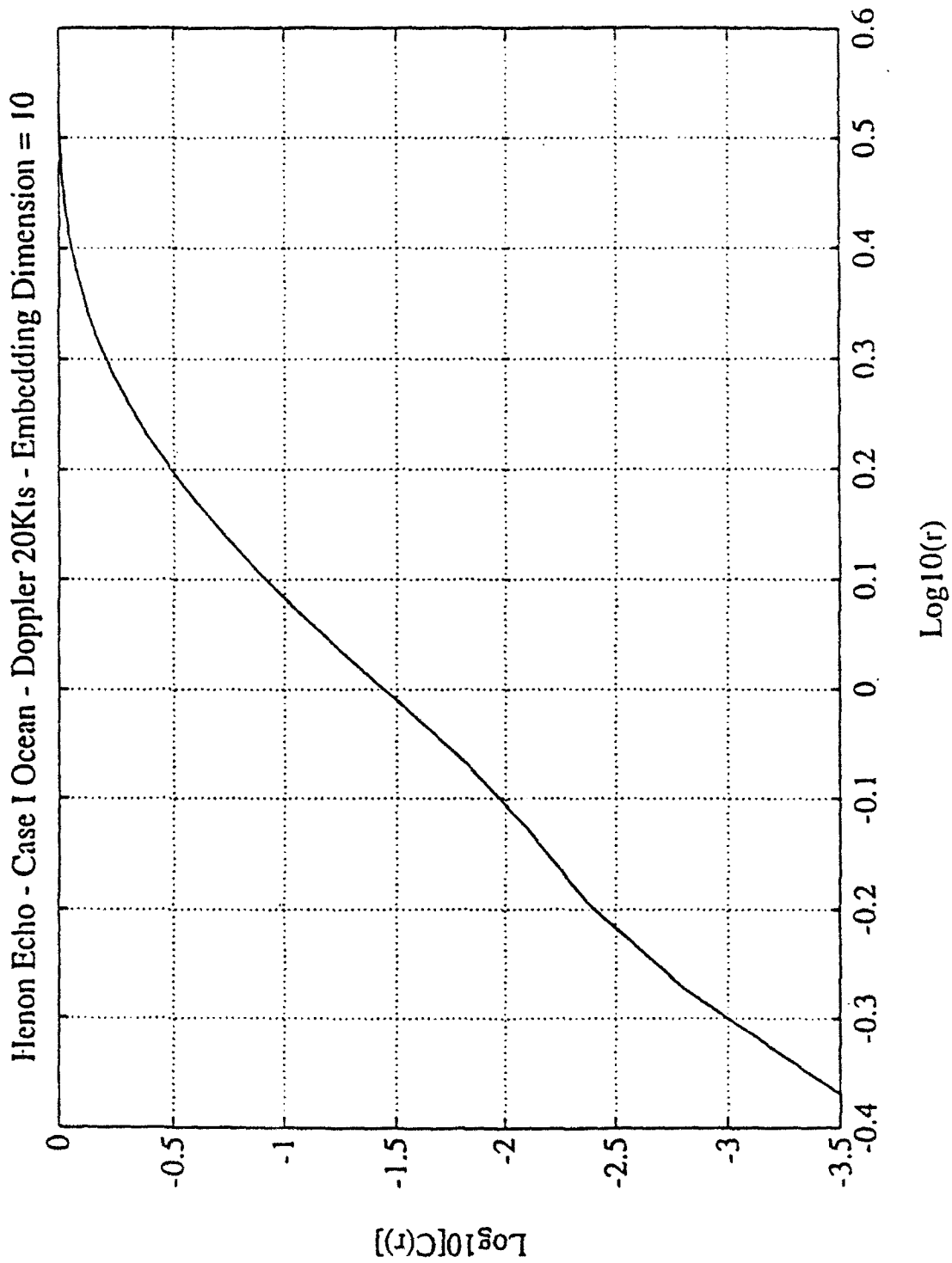


Figure G-18. Correlation Dimension Extraction Curve for Henon Waveform Propagated Through Case I Ocean with 20 Knots Doppler, Embedded in 10 Dimensions.

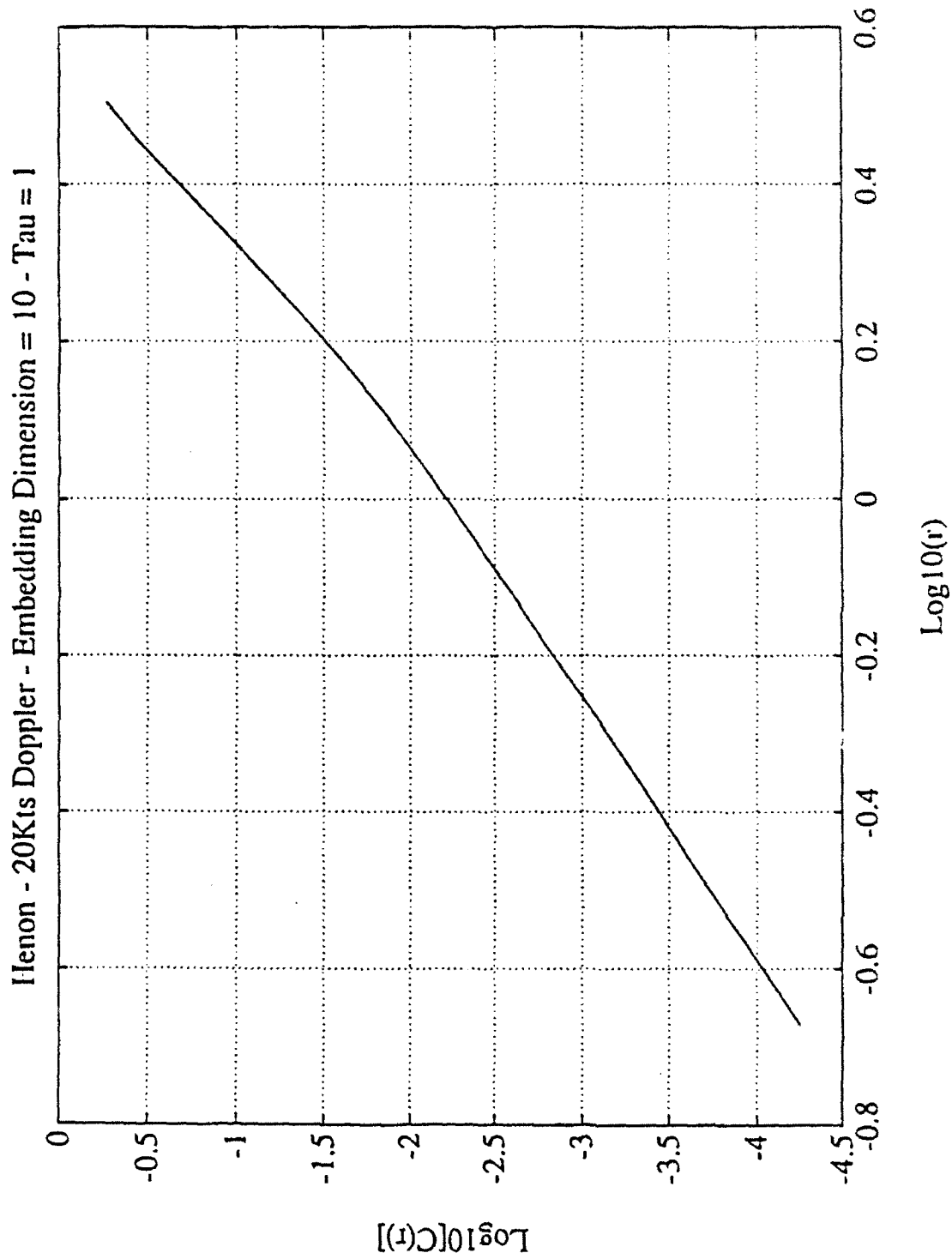


Figure G-19. Correlation Dimension Extraction Curve for Henon Waveform with 20 Knots Doppler, Embedded in 10 Dimensions.

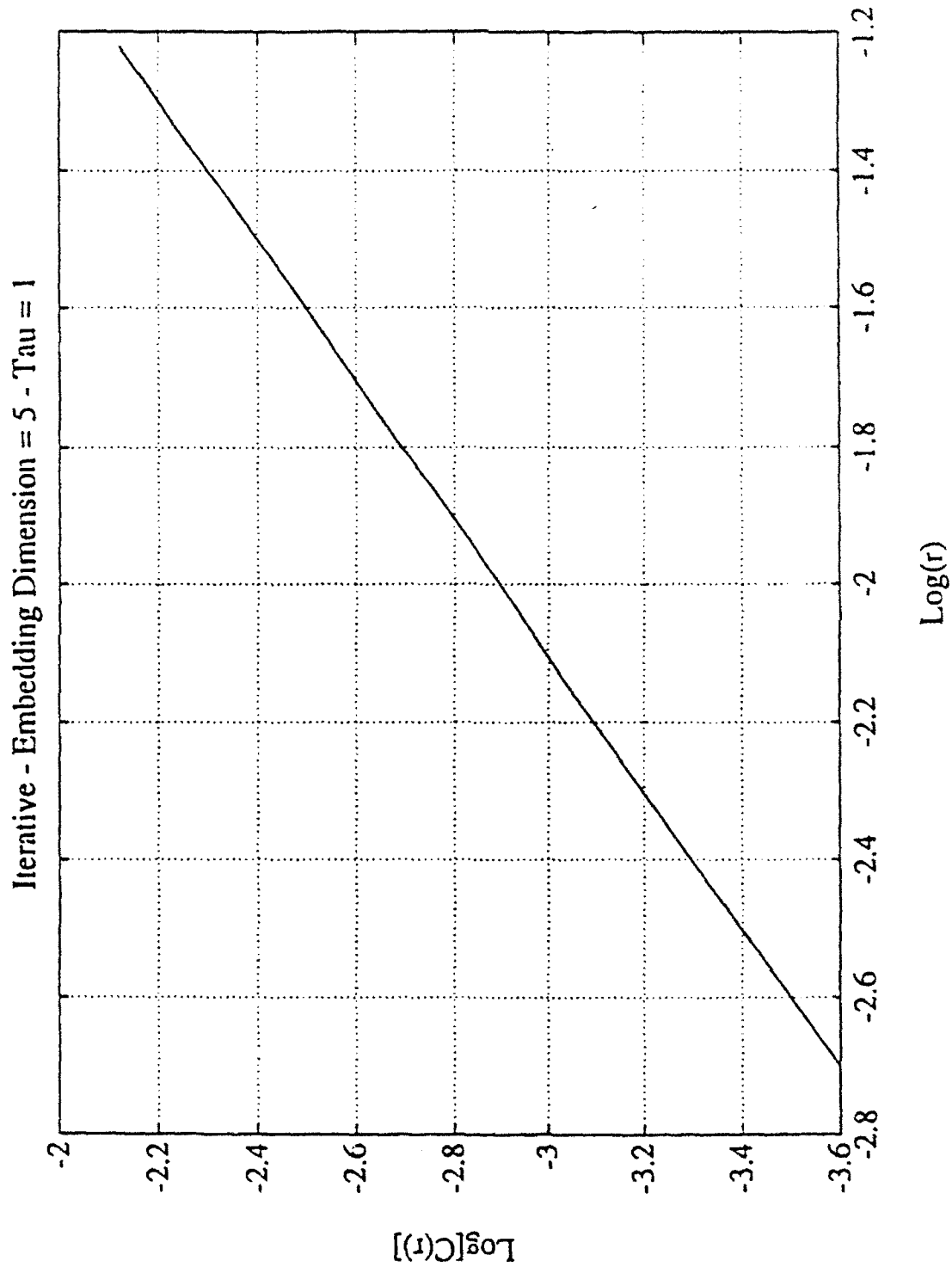


Figure G-20. Correlation Dimension Extraction Curve for Iterative Waveform Embedded in 5 Dimensions.

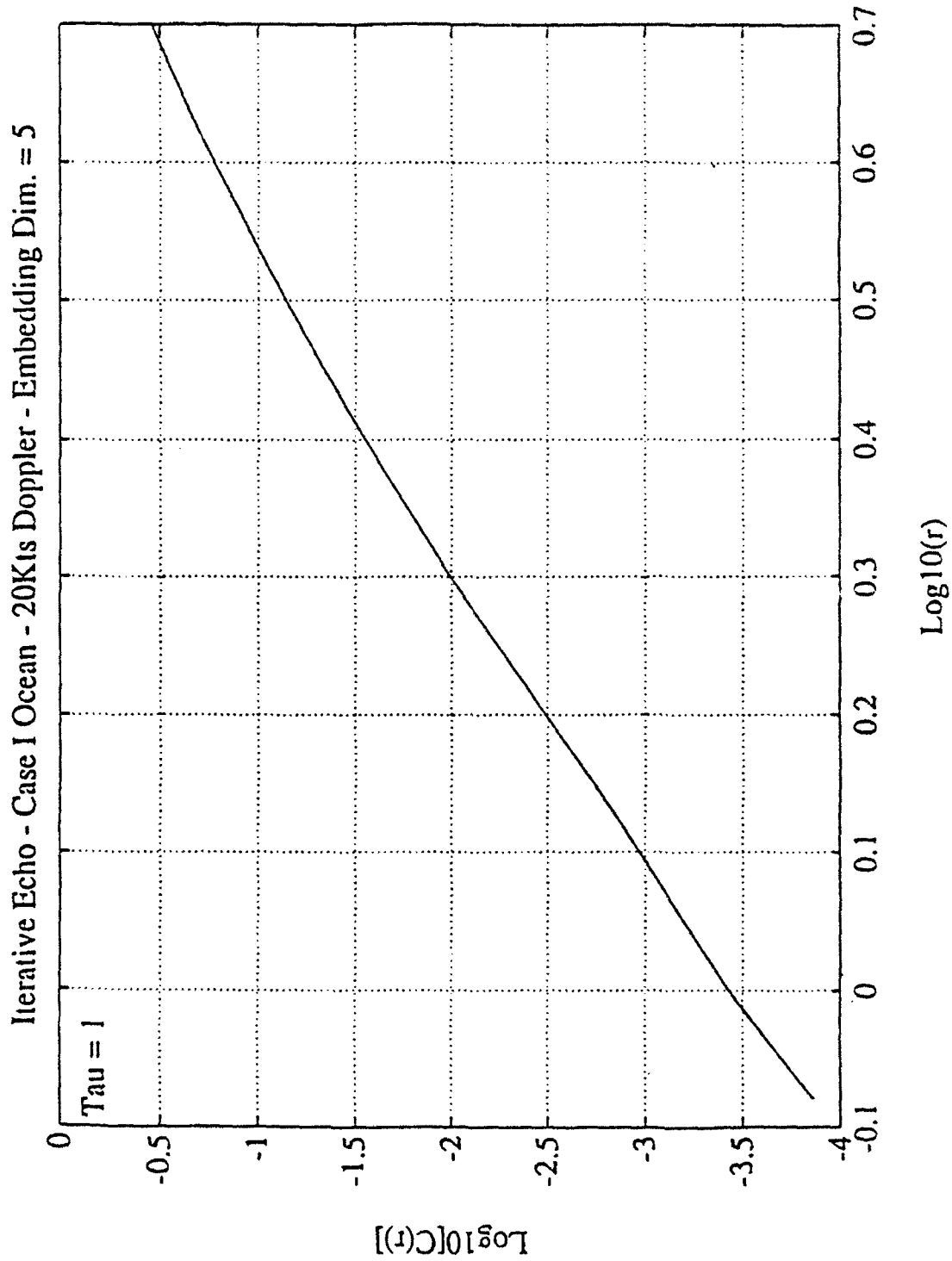


Figure G-21. Correlation Dimension Extraction Curve for Iterative Waveform Propagated Through Case 1 Ocean with 20 Knots Doppler, Embedded in 5 Dimensions.

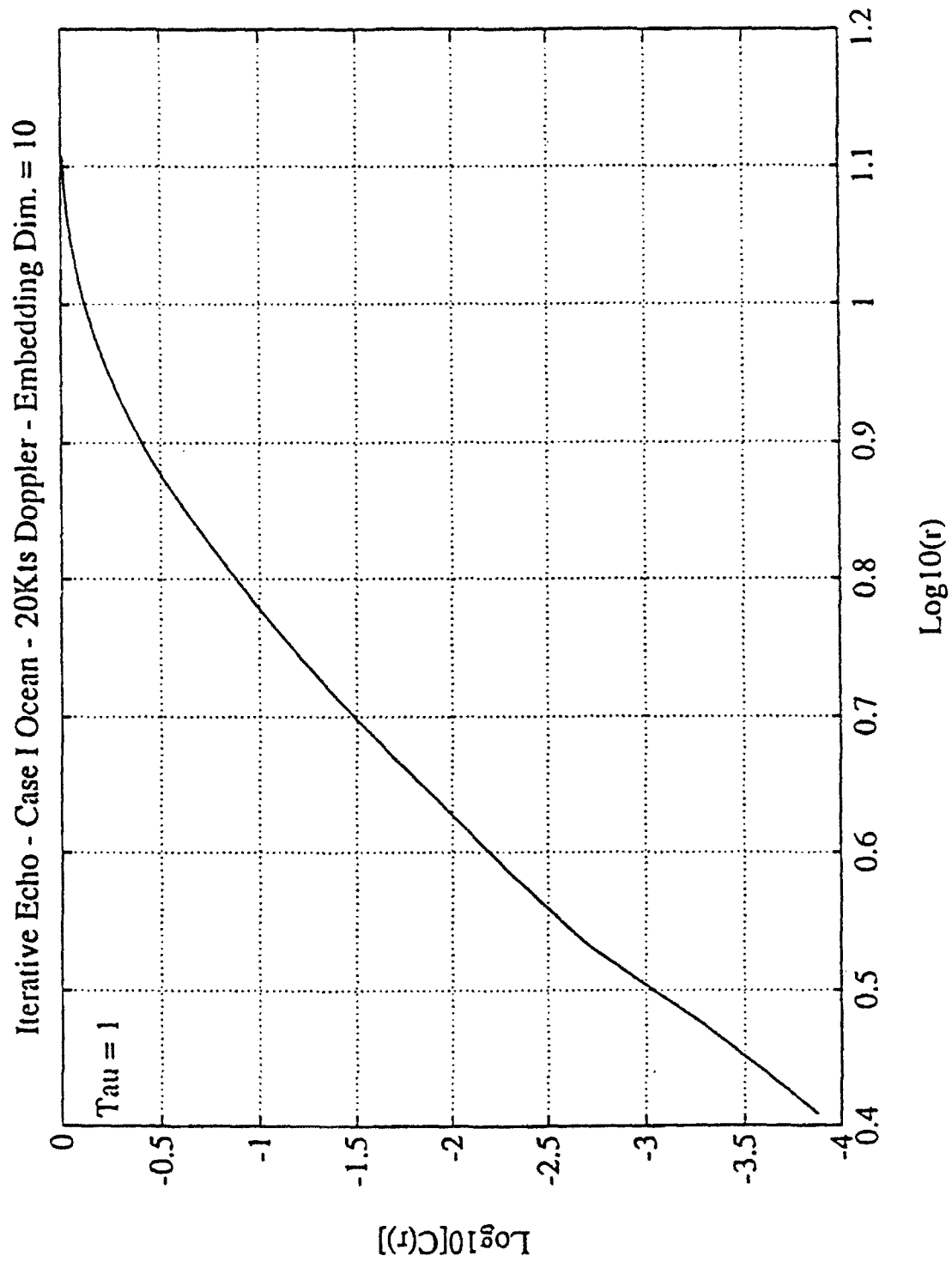


Figure G-22. Correlation Dimension Extraction Curve for Iterative Waveform Propagated Through Case I Ocean with 20 Knots Doppler, Embedded in 10 Dimensions.

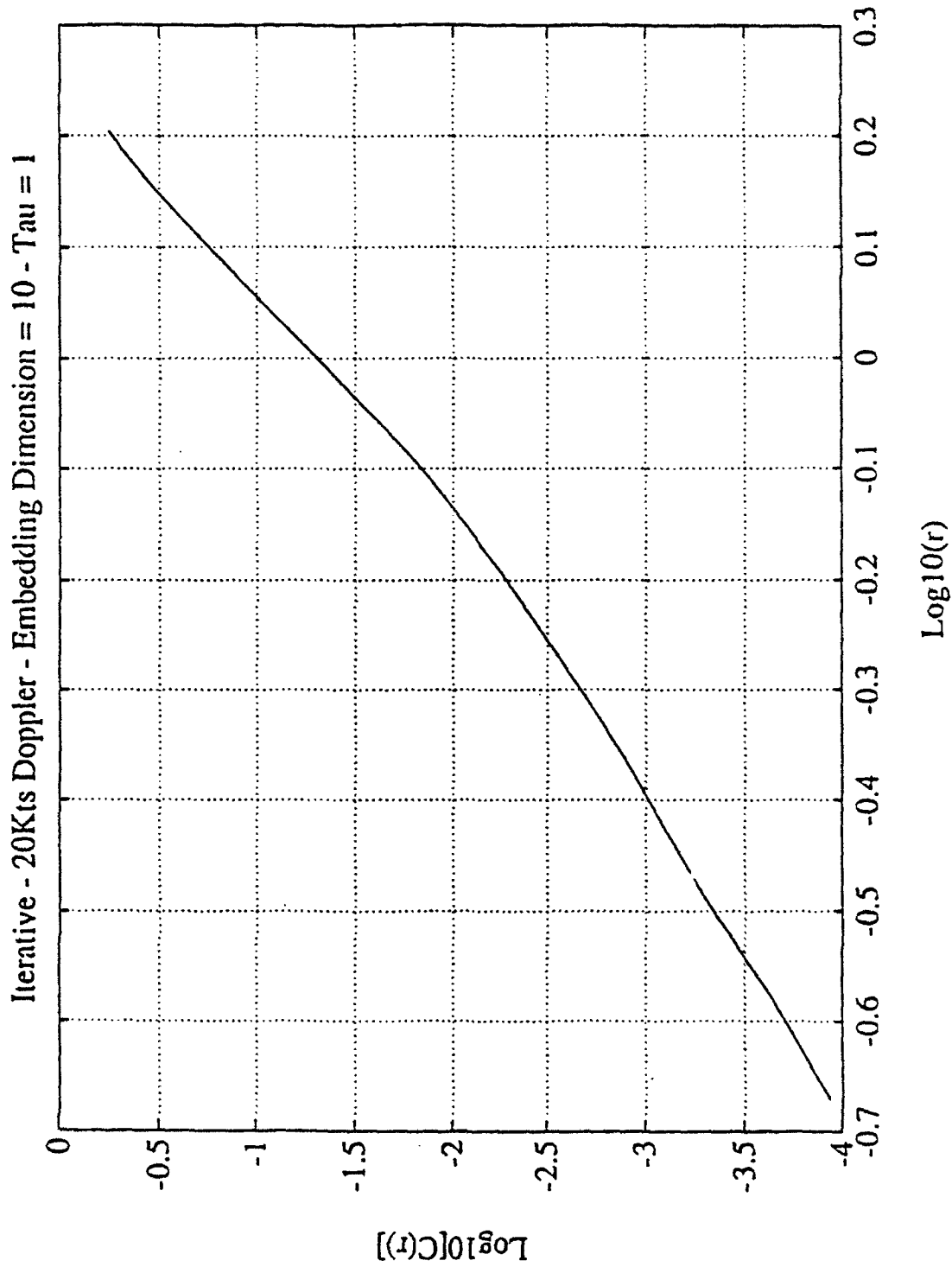


Figure G-23. Correlation Dimension Extraction Curve for Iterative Waveform with 20 Knots Doppler, Embedded in 10 Dimensions.